Coherent two-dimensional electronic broad-band UV-spectroscopy of DNA and its nucleobases

Dissertation
zur Erlangung des Doktorgrades Dr. Rer. Nat.

eingereicht an der Fakultät für Mathematik,
Informatik und Naturwissenschaften
Fachbereich Physik
Universität Hamburg

vorgelegt von
M.Sc. Alessandra Picchiotti
aus Brescia, Italien

Hamburg, 29 März 2017

Alessandra Picchiotti

Coherent two-dimensional electronic broad-band UV-spectroscopy of DNA and its nucleobases

Gutachter der Dissertation:
Prof. Dr. R. J. Dwayne Miller
Prof. Dr. Arwen R. Pearson

Gutachter der Disputation:
Vorsitzende/r: Prof. Dr. Michael Rübhausen
Erstgutachter/in: Prof. Dr. R. J. Dwayne Miller
Zweitgutachter/in: Prof. Dr. Arwen R. Pearson

Datum der Disputation: 19/06/2017

Itaque illum ego feliciorem dixerim qui nihil negotii secum habuit, hunc quidem melius de se meruisse qui malignitatem naturae suae vicit et ad sapientiam se non perduxit sed extraxit.

(Seneca - Epistuale Morales Ad Lucilium (V,52,6))

Contents

Abstract

The photostability of *DNA* is highly complicated, and yet crucial, as dimerization of bases due to excitation could lead to skin cancer. Therefore, the physical properties of *DNA* are studied in order to understand its biochemical functions and pathology, such as the influence of UV light on cancer formation, which is related to the presence of thymine photoproducts.[1] The presence of excitons in this process has been proposed[2–17], and the investigation of *DNA* and its composing nucleobases excitation pathways raises a number of questions, such as the role of solvents in the release of excessive energy, the interaction of different solvents with nucleobases, the possible differences between nucleobases themselves, and ultimately, the possibility of an universal mechanism. The present work uses sensitive optical techniques - electronic broad band transient absorption (TA), and two-dimensional photon echo (2DPE) spectroscopies - in order to study these phenomenons.

In order to cover a wide spectroscopic window, broadband time-resolved spectroscopy in the UV is used, as it covers the full absorption peak of *DNA* and nucleobases. This is very demanding, and this work demonstrates the possibility of overcoming the inherent challenges by using a novel optical setup that covers nearly all the lowest absorption bands and excited-state emission bands of *DNA* and nucleobases (250 to $300\,\mathrm{nm}$). The setup can record very short dynamics, including oscillatory behaviors due to Raman frequencies, as it has such a broadband spectral window and short pulse length ($6-8\,\mathtt{fs}$ in fwhm), combined with a closed-loop wire-guided jet system for handling the liquid samples.[18]

An extensive characterization of single nucleobases and short single strands of $DNA\,(ssDNA)$ using steady-state absorption and circular dichroism spectroscopy, was conducted priorly to the time-resolved experiments. The linear spectroscopy study (absorption and circular dichroism) of *ssDNA* revealed two major electronic excitations below the band at $260\,\mathrm{nm}$, as well as a linear relationship between the number of nucleobases in a single strand and the dipole strength. Furthermore, the delocalization of excitons is dependent on the length of the oligomeric chain, though this varies; in adenosine the exciton is localized only on nearest neighbors, in $(dT)_n$ and $(dAT)_n$ the range grows as the strand lengthens.

The performance of the TA and 2DPE system was first tested an characterized by using pyrene, a well-known dye[19–25] with a high transition dipole strength, well-known electronic transitions, relatively small chemical structure, and clear Franck-Condon progression. The study suggests two possible alternative mechanisms for the de-excitation of pyrene. The excitation of the S_4 is followed by a sub-picosecond relaxation of the excited population to the phantom state S_3, then to the S_2 (8 ps) and finally to the L_b states (24 ps), assuming the characteristics of S_1 at the minimum; the population is trapped for an extended time in the S_1/L_b bottle-neck minimum before relaxing to the ground state. Alternatively, there is a single conical intersection (CI) between S_3 and L_b, and the fluorescence structure at $350 - 368$ nm is instead associated with a relaxation from the L_b after the CI with the phantom state; the S_2 level is not involved in de-excitation.

Furthermore, the TA and 2DPE study of nucleobases uncovered an universal mechanism of two-step photo-deactivation that is valid for all investigated $ssDNA$ bases, extending previous studies that proposed it for cytosine[26] and adenine.[27] The population passes from an initially excited bright state $\pi\pi^*$ through an $n\pi^*$ (dark) state to the ground state via two CIs; the dark state $n\pi^*$ is shared by all nucleobases. The findings were enhanced by theoretical modeling of 2D spectra in the vicinity of two CIs and excited state absorptions[28], which closely matched the experimental spectra, as it reproduced the two peaks with opposite signs present in the 2DPE experimental spectra.

To the best available knowledge, this is the first experimental broadband TA and 2DPE spectra of $ssDNA$ in the far UV ever reported in literature. By comparing the experimental TA and 2DPE spectra of single nucleobases and DNA strands, the intermediate lifetime increases when nucleobases are stacked in $ssDNA$, and the amplitude of the decay associated spectra associated with the longest lifetime also increases. This findings could be enriched by building a theoretical framework, as well as continuing the experimental work toward double stranded DNA.

Zusammenfassung

Die Photostabilität der *DNA* ist hochgradig komplex und essentiell, da die Dimerisierung von Nukleobasen aufgrund von Photoanregung zur Bildung von (Haut-)krebs führen kann. Daher ist es wichtig, die physikalischen Eigenschaften der *DNA* zu untersuchen, um biochemische und pathologische Mechanismen zu verstehen, wie z.B. den Einfluss von UV-Strahlung auf die Bildung von Hautkrebs, welche sich auf die Photoprodukte des Thymins zurückführen lassen.[1] In diesem Zusammenhang wird die Anwesenheit von Exitonen vermutet[2–17], und die Untersuchung von *DNA* und der Anregungspfade ihrer Nukleobasen wirft eine Reihe neuer Fragen auf, wie z.B. den Einfluss des Lösungsmittels in der Abgabe von Überschussenergie, die Wechselwirkung verschiedener Lösungsmittel mit den einzelnen Nukleobasen, die Unterschiede zwischen den Nukleobasen selbst, und letztlich die Möglichkeit eines universellen Mechanismus. Die hier vorliegende Arbeit verwendet hochpräzise spektroskopische Methoden - breitbandige elektronische transiente Absorptionsspektroskopie (TA) und zweidimensionale Photonenecho (2DPE) Spektroskopie – um die beschriebenen Zusammenhänge zu untersuchen.

Um einen möglichst großen Spektralbereich abzudecken, wird breitbandige, zeitaufgelöste UV Spektroskopie verwendet, da diese Technik alle Absorptionsbanden von *DNA* und ihrer Nukleobasen abdeckt. Dies ist eine experimentell sehr anspruchsvolle Aufgabe und die vorliegende Arbeit demonstriert die Möglichkeit, diese Herausforderungen zu meistern, in dem ein neuartiger optischer Aufbau genutzt wird, welcher fast die gesamten tiefliegenden Absoprtionsbanden und angeregten Emissionsbanden der *DNA* und der Nukleobasen (250 bis 300 nm) abdeckt. Der experimentelle Aufbau kann sehr kurzlebige Dynamiken, einschließlich dem Verhalten von Oszillatoren in Abhängigkeit von Ramanfrequenzen, untersuchen, da es sehr breitbandig ist und gleichzeitig über sehr kurze Pulsdauer ($6 - 8$ fs fwhm), in Kombination mit einem geschlossenen Kreislauf Drahtflüssigkeitsfilm, verfügt.

Vor den zeitaufgelösten Untersuchungen wurde eine ausgiebige Charakterisierung der Nukleobasen und kurzer einzelsträngiger *DNA* (*ss-DNA*) mit statischer Absoprtions- sowie Zirkulardichroismusspektroskopie durchgeführt. Diese lineare Spektroskopie-Studie (Absorption und Zirkulardichroismus) von *ssDNA* enthüllte zwei dominierende elek-

3

tronische Anregungen unterhalb der Absorptionsbande bei $260\,\mathrm{nm}$, sowie einen linearen Zusammenhang zwischen der Zahl der Nukleobasen in einem Einzelstrang *DNA* und der Dipolstärke. Darüber hinaus ist die Delokalisation der Exitonen abhängig von der Länge der Oligomere. Dies variiert jedoch: In Adenosin ist das Exiton nur auf den nächsten Nachbarn lokalisiert, wohingegen in $(dT)_n$ und $(dAT)_n$ die Reichweite der Delokalisierung mit der Oligomerlänge zunimmt.

Der TA und 2DPE Aufbau wurde zunächst anhand von Pyren, einem gut untersuchtem Farbstoff[19–25], getestet und charakterisiert. Pyren weist ein hohes Diplolübergangsmoment, klar charakterisierte elektronische Übergänge, eine relativ kleine molekulare Struktur und klare Franck-Condon-Progressionen auf. Die Untersuchung von Pyren mittels TA und 2DPE deutet auf zwei mögliche Mechanismen der Relaxation auf. Die Anregung in den S_4 Zustand bewirkt eine subpicosekunden Relaxation der angeregten Population in den Phantomzustand S_3, gefolgt von Abregung in den S_2 ($8\,\mathrm{ps}$) und schlussendlich in den L_b Zustand ($24\,\mathrm{ps}$), unter der Annahme der Eigenschaften von S_1 im Minimum; die Population ist dann für einen längeren Zeitraum im S_1/L_b Flaschenhals-Minimum gefangen, bevor diese in den Grundzustand relaxiert. Alternativ gibt es eine einzelne konische Verschneidung zwischen S_3 und L_b, und die Fluorezenzstruktur bei $350-368\,\mathrm{nm}$ ist stattdessen mit der Relaxation des L_b nach der konischen Verschneidung mit dem Phantomzustand assoziiert; der S_2 Zustand ist hierbei nicht involviert.

Weiterhin haben die TA und 2DPE Untersuchungen der Nukleobasen einen universellen Mechanismus einer aus zwei Schritten bestehenden Photodeaktivierung hervorgebracht, welcher für alle untersuchten *ssDNA* Nukleobasen gültig ist und welcher bisherige Studien, die diesen Mechanismus für Cytosin[26] und Adenin[27] vorgeschlagen haben, erweitert. Die angeregte Population relaxiert über einen zunächst hellen angeregten Zustand $\pi\pi^*$ durch einen (dunklen) Zustand $n\pi^*$ über zwei konische Verschneidungen (CI) in den Grundzustand; der dunkle Zustand $n\pi^*$ findet sich in allen Nukleobasen. Diese Ergebnisse wurden mittels theoretischer Berechnungen der 2D Spektren in der Nähe der zwei CI und den Absorption des angeregten Zustandes vervollständigt.[28] Diese Simulationen reproduzieren die experimentellen Spektren sehr gut, da diese die zwei Banden mit gegensätzlichem Vorzeichen aus dem experimentellen 2DPE Spektren reproduzieren.

Soweit bekannt sind dies die ersten experimentellen breitbandigen TA und 2DPE Spektren von *ssDNA* im tiefen UV, die jemals berichtet wurden. Der Vergleich von experimentellen TA und 2DPE Spektren der einzelnen Nukleobasen mit *DNA* Strängen zeigt, dass die Lebensdauer sich vergrößert, wenn Nukleobasen in gestapelter Form in *ssDNA* vorliegen und die Amplitude des decay associated spectra mit der assoziierten längsten Lebensdauer auch zunimmt. Diese Ergebnisse könnten erweitert werden mithilfe weiterer theoretischen Modelle, sowie der experimentellen Untersuchungen Doppelstrang-*DNA*.

Preface

This section is dedicated to the copyright holders of data and images (especially when published elsewhere and in collaboration with other scientists).

Chapter 2. The simulations presented in Fig. 2.8, 2.9, and 2.10 were performed by Michal Kochman, so the simulations in Figures A.7, A.8 and A.9, in the appendix A.2.

Chapter 3. Figures 3.1, 3.2, 3.3, 3.6, 3.7, 3.9, 3.10, 3.11 and 3.13, and Tables 3.1 and 3.2 are used with permission from applicable sources.[18,29] Portions of the text are used with permission from *A. Picchiotti et al., Rev. Sci. Instrum., 2015, 86, 093105*[18] of which I am an author.

Chapter 4. Figures 4.7, 4.8 and 4.9 are used with permission from applicable sources.[30,31]

Chapter 5. Nenov and Giussani are the authors of all the simulations presented in chapter 5. In particular Giussiani has performed all the dynamic simulations, and Nenov all the time-resolved simulations (TG and PE).

Chapter 6. Figures 6.7, 6.10, 6.13, 6.8, and Tables 6.3 and 6.4 are used with permission from applicable sources. Portions of the text are used with permission from *V. I. Prokhorenko, A. Picchiotti et al., J. Phys. Chem. Lett. 4445–4450 (2016)*[28] of which I am an author. Figure 6.12 represents data collected by Florian Biebl from the group of Prof. Rübhausen.

Chapter 9. The original idea in Sec 9.1 and the two following, and the planning of the experiment are mine, while Anne-Laure Calendron and Ling Ren participated with the acquisition of the preliminary data (Fig. 9.1) and the development of the idea. The rest of the outlook (Sections 9.4 and 9.5) are conceptualized by me.

Acknowledgements

Here, you can find various acknowledgments that were not included in the previous section. I would like to thank Dr. Valentyn Ivanovich Prokhorenko, Prof. Arwen Ruth Pearson and Prof. R. J. Dwayne Miller for having accepted me as a PhD student and tutored me until I was ready for graduating. Dr. Prokhorenko has always been an invaluable mentor and presence in the lab.

I'd like also to thank Ling Ren, Ryan Field, Nele Mueller, Samansa Maneshi and Amy Stevens for helpful discussions in those past years. To Samansa goes my deepest gratitude for facilitating my way through experimental multi-dimensional spectroscopy. I wish to extend my acknowledgments to all the people that have read and commented on my thesis before being submitted; Aradhana Choudhuri, Peter Kroetz, Anne-Laure Calendron, Johannes Kaub, and Miguel Ochmann for various contributions. I would like to thank all the IMPRS staff, the IMPRS itself, and especially Julia Quante and Sonia Utermann. I would like to extend my acknowledgment too all the people in my group, and in the groups I have worked with, the SPC facility, the groups of Prof. Huse, Prof. Rübhausen, and Prof. Henning, moreover, all the collaborators and colleagues I interacted with in the past years. Thanks also to the administration and IT people, that facilitated my stay in multiple ways. My friends and my family supported me, and I would like to thank them as well.

Separate and special thanks to Alex for proof-reading page-by-page multiple times with an incredible patience, as many other things he has done to support me, from bringing me dinner in the lab at least three times a week for the past four years, to cheering me up in uncountable occasions. To him I dedicate my thesis.

Chapter 1

Introduction

1.1 Motivation

DNA is the building block of life, but in some aspects, it remains poorly understood. The photostability of *DNA* is highly complicated, as several bases can interact through stacking and base pairing. New quantum states arise as linear combinations of single base wavefunctions, denoted by Frenkel excitons[32]; these represent the collective excitation of two or more bases. The spatial extent of excitation and the dynamics of the quantum states are hotly debated, and excitons are crucial, as dimerization of neighboring bases in *DNA* could lead to skin cancer. This is the starting point of the research and investigations of this study.

Uncovering the physical properties of *DNA* will in turn lead to a greater understanding of its biochemical functions and pathology, such as the influence of UV light on cancer formation; in particular, the presence of thymine photoproducts, a well-known cancer inducer.[1] In this process, the presence of excitons in the UV excitation of *DNA* has been proposed[2–17], but has not been conclusively proven. Very sensitive optical techniques that can overcome these difficulties are pump probe, time resolved fluorescence and two-dimensional photon echo spectroscopies.

One technical limitation of the existing literature is that it lacks the coverage of a wide spectroscopic window, which is necessary in order to effectively investigate the photodynamics of nucleobases and *DNA*; for instance, West et al.[33] and Tseng et al[34] have already conducted 2D spectroscopy on adenine, but in a 6 and $3\,\mathrm{nm}$ window respectively, which limits the available information. Thus, it would be better to

8

have broadband time-resolved spectroscopy in the UV, so as to cover the full absorption peak of DNA and nucleobases.This is a challenging task with stringent requirements. It is necessary to generate coherent broadband light pulses in the UV range and with short pulse durations. In order to prevent strong background scattering, cuvettes and windows should absolutely be avoided. Furthermore, there is the solvent response to consider, and the very low transition dipole strength of nucleobases and DNA, which leads to a small signal. Finally, 2D spectroscopy requires high phase stability, which is not trivial in the UV. The novel aspect of this work is that it overcame said challenges with an innovative optical setup, described in 4, that allows the full coverage of nearly all the lowest absorption bands and excited-state emission bands of DNA and nucleobases (250 to 300 nm), and therefore enables a coherent and comprehensive approach to the photodynamics of nucleobases and DNA. With a broadband spectral window and short pulse length ($6-8$ fs in fwhm), the setup can record very short dynamics, including oscillatory behaviors related to Raman frequencies. This is in particular enabled by the absence of cuvettes windows by means of a closed-loop wire-guided jet system, described in Chapter 3.

Overcoming the technical challenges is only the first step. The performance of such a novel setup has to be tested, and this was done in Ch. 5 by using pyrene, a well-known dye.[19–25] Pyrene was chosen due to its high transition dipole strength, well-known electronic transitions, and relatively small chemical structure.Pyrene has a clear Franck-Condon progression, making it easier to disentangle vibrational and electronic excitations. Therefore, pyrene is the dye of choice for the characterization of the setup. As an aside, as in the case of DNA, all reported photon echo (PE) and transient absorption (TA) experiments in the deep UV were conducted in a one-color fashion and with a small bandwidth pump; this limits the type of information in the experimental data.[22,35,36] Yet, this setup can detect all de-excitations and Raman frequencies in both the ground and excited states presented in this work.

In the quest to uncover excitons, the first step is the investigation of nucleobases, as their photodynamics are a long-standing question in chemical physics. As an example, the survival of nucleobases during the UV bombardment of the pre-biotic world remains a mystery. The exact mechanisms are still unclear, due to limitations in available

techniques until recently, although this is changing with the increasing availability of femtosecond lasers and higher computational power. There are a wide variety of questions related to nucleobase excitation pathways, including the role of solvents in the release of excessive energy, the interaction of different solvents with nucleobases, the possible differences between nucleobases themselves, and conversely, the possible existence of an universal mechanism applicable to all nucleobases. The data presented in this study sets out to answer these questions, though they are limited to the "natural" nucleic acids (thymine, guanine, adenine, and cytosine) and some "natural" modifications (presence of a sugar ribose and phosphate groups), mimicking the molecules present in unmodified *DNA*.

Some groups have already reported a number of femtosecond time-resolved spectra on nucleobases, using various techniques: transient absorption[6,13,15,16,37–45], time-resolved fluorescence[6,44,46–48], and photoelectron spectroscopy.[49–53] However, these highly-focused studies reach a number of different conclusions. Rather, this work, based on a comprehensive approach, seeks to uncover an universal scenario for nucleobases, which will enable the foundations for future work on *DNA*, for which preliminary data are presented here.

1.2 A brief history of *DNA* spectroscopy

Nucleobases were first isolated by Kossel, during the final phase of the Industrial Revolution in 1879.[54,55] In tandem, radiation was used for the first time for inactivating or killing microbes by damaging their DNA.[56,57] This first step was followed by a number of proposals and discoveries in the first half of the 20th Century. Hartley examined the UV absorption of nucleobases in 1905.[58] In 1928, Koltzoff was the first to propose that the genetic information of a cell is encoded in a long chain of amino acids[59], while Altenburg demonstrated that UV radiation induces mutations in fruit flies[60], and Findlay proved that the exposure to UV radiation causes skin cancer through *in vivo* experimentation.[61] Finally, by 1951 further studies had uncovered limits to photoinduced repair mechanisms.[62]

The fifties and sixties saw a spate of discoveries, the most salient being that of the double-helix structure of DNA.[63,64] This was followed by the first study on steady-state fluorescence of adenine and guanine at room temperature by Duggan et al. in 1957[65], and of the

fluorescence quantum yield of DNA by Pisarevskii et al. in 1966,[66] In 1968, Eisinger and Shulman attempted to identify the excited electronic states of nucleobases and DNA based on fluorescence and phosphorescence quantum yields.[67] Finally, in 1969 Falk et al. initiated the study of photophysics by uncovering the role of hydration in DNA by means of infrared studies.[68]

This mid-century wave of discoveries has been recently supplemented by time-resolved spectroscopic studies with femtosecond resolution of nucleobases and DNA due to the development of titanium-sapphire lasers.[69] The first femtosecond fluorescence spectroscopy on nucleobases was recorded in 2001 by Peon and Zewail[46], and in 2003 on DNA by Markovitsi et al.[70] Subsequently, Pecourt and Crespo-Hernandez studied nucleobases and DNA with transient absorption spectroscopy[53,71], and Onidas with fluorescence up-conversion spectroscopy.[47] Photon echo spectroscopy on nucleobases is even more recent.[33,34]

1.3   Absorption and circular dichroism

The etymology of spectroscopy draws on the Latin *spectron* for ghost and the Greek $\sigma\kappa o\pi\varepsilon\bar{o}$ (*skopèō*) for sight.[72] These roots are telling. Molecular spectroscopy allows one to use light in order to interrogate matter without ever directly observing said molecules, only their influence on the light. Different spectroscopies grant different perspectives. Absorption or emission spectroscopies are referred to as linear spectroscopy, as they involve a weak light-matter interaction, with one primary incident radiation field, and are typically presented on a single frequency axis.

Absorption spectroscopy is a widely used technique to measure the wavelength-dependent intensity at which molecules absorb the light. The incident light I_0 passes through the sample and after being absorbed by it, is measured in transmission. The transmittance T of a material is defined as:

$$T = 10^{-OD},\tag{1.1}$$

where OD is the optical density, also known as absorbance. In liquids and in case of uniform attenuation, the Beer-Lambert law states that the optical density is related to a sample's wavelength-dependent

extinction coefficient $\varepsilon(\lambda)$, measured in $\texttt{cm}^{-1} \cdot M^{-1}$, via:

$$OD(\lambda) = c \cdot l \cdot \varepsilon(\lambda) \tag{1.2}$$

where l is the path length (in $\texttt{cm}$) of the sample, and c is the concentration of the solute (in M). In turn, the extinction coefficient (or molar attenuation coefficient) depends on the dipole strength D, defined as the square of the electric dipole transition moment μ, measured in Debye $[D]$. The magnitude of $D := \mu^2$, measured in $[D^2]$ relates to the measured absorption spectrum by[73]:

$$D := \mu^2 = 9.2 \cdot 10^{-3} \int \frac{\varepsilon(\nu)}{\nu} \mathrm{d}\nu, \tag{1.3}$$

where ν is the wavenumber with units of $\texttt{cm}^{-1}$. Hence, integration is done globally across the absorption spectrum to retrieve μ^2.

Circular dichroism is a widely used chiro-optical technique in biochemistry. It provides information on the three-dimensional configuration of the molecules and on the direction of their transition dipole moments.[74–81] A dipole moment oriented in space interacts with a circularly polarized electromagnetic field differently depending whether the field is left- or right-circularly polarized. Thus left- and right- polarized light is absorbed to a different extent, and the difference can be defined as:

$$\Delta\varepsilon = \varepsilon_L - \varepsilon_R, \tag{1.4}$$

where, ε_L is the extinction coefficient of the left (L) polarized light and ε_R is the extinction coefficient of the right (R) polarized light.

One has to mention the molar ellipticity, a unit of measurement used in circular dichroism spectroscopy for historical reasons. Molar ellipticity $[\theta]$ is defined as the circular dichroism corrected for concentration, where it depends on the definition of ellipticity of the polarization θ:

$$\tan(\theta) = \frac{E_R - E_L}{E_R + E_L}, \tag{1.5}$$

where E_R and E_L are respectively the magnitudes of the electric field vectors of the right-circularly polarized light and the left-circularly polarized light. One can approximate the tangent function to its argument in equation 1.5, based on the assumption that θ is generally small:

$$\theta = \frac{E_R - E_L}{E_R + E_L}, \tag{1.6}$$

and using the Beer law for liquids in its natural logarithm form:

$$I = I_0 e^{-A \ln 10}, \tag{1.7}$$

where I is the intensity of light, I_0 is the incident light at the beginning, A the absorbance, and that I is proportional to the square of the electric field vector, the equation 1.6 becomes:

$$\theta(\text{radians}) = \frac{(e^{\frac{-A_R}{2} \ln 10} - e^{\frac{-A_L}{2} \ln 10})}{(e^{\frac{-A_R}{2} \ln 10} + e^{\frac{-A_L}{2} \ln 10})} = \frac{e^{\Delta A \frac{\ln 10}{2}} - 1}{e^{\Delta A \frac{\ln 10}{2}} + 1}. \tag{1.8}$$

Another approximation can be used, that the differential of absorbance $\Delta A := A_L - A_R$ is much smaller than 1, therefore applying the Talyor expansion up to the first-order, one obtains:

$$\theta(\text{degrees}) = \Delta A \left(\frac{\ln 10}{4} \right) \left(\frac{180}{\pi} \right). \tag{1.9}$$

One can now remove the dependence from the concentration and define the molar ellipticity $[\theta]$, measured in `deg · cm`^{2}`/dmol` as:

$$[\theta] = \frac{100\theta}{C l}, \tag{1.10}$$

where C is the concentration in M and l is the path length in cm. This last equation can be related to the differential extinction coefficient by using again the Beer law (Eq. 1.7):

$$[\theta] = 3298.2 \Delta \epsilon. \tag{1.11}$$

CD provides information on the arrangement of subunits and on the direction of their transition dipole moments.[81,82] A dipole moment oriented in space interacts differently with a circularly-polarized electromagnetic field depending whether it is left-(L) or right-(R) circularly polarized.

1.4 Time-resolved and multidimensional spectroscopy

The static techniques traditionally used in spectroscopy - absorption, circular dichroism, and fluorescence - are unable to follow the fast changes that occur after (electronic or vibrational) excitation. The linear optical (LO) interactions are substituted with non linear optical (NLO) interactions. Time-resolved techniques (also NLO techniques) are an evolution of these static techniques, whereby molecules

are investigated at a delay time after initial excitation. There are significant difficulties inherent in building a more complicated setup, but the effort is nonetheless justifiable, as the molecular system is not immutable and after excitation will alter either its chemical or physical properties. After a time delay the molecule will either relax to its previous initial state or to a new state with different properties, once an energy barrier (potential) is passed over.[83] The key element to understanding these changes is time sensitivity; the shorter the light pulses, the faster the phenomena that can be investigated. For instance, the atoms in a molecule typically perform one vibration in $10 - 100\,\mathtt{fs}$, so pulses must be ultrafast to be sensitive to the time-scales investigated in this study. This was possible only due to the advancement of laser technology, and the development of ultra-fast lasers.[69]
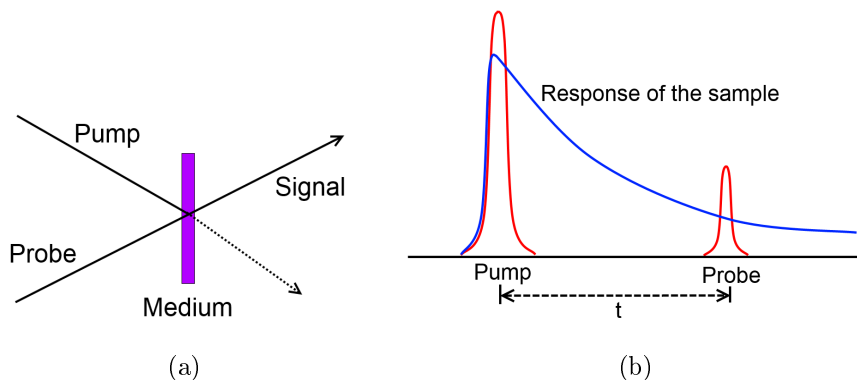

Figure 1.1: Schematic showing the geometrical disposition (1.1(a)) and the time ordering (1.1(b)) of the two pulses interacting with the sample (the medium) in a pump-probe spectroscopy setup.

The simplest NLO technique is pump-probe (transient absorption). This technique uses two laser pulses, as schematically shown in Fig. 1.1. The first pulse, called the pump, is the more powerful of the two and excites the sample. The second pulse, called the probe, is less powerful and detects the sample at a delay time, especially changes in the sample. Modifying the delay time allows one to detect how rapidly the sample changes, and excitation leads to the sample possibly going through one or more transition states, which each will have a distinct spectrum.

However, pump-probe does not provide sufficient information to immediately understand the spectra, as it is often heavily congested with information overlaps. The ambiguities that arise when interpret-
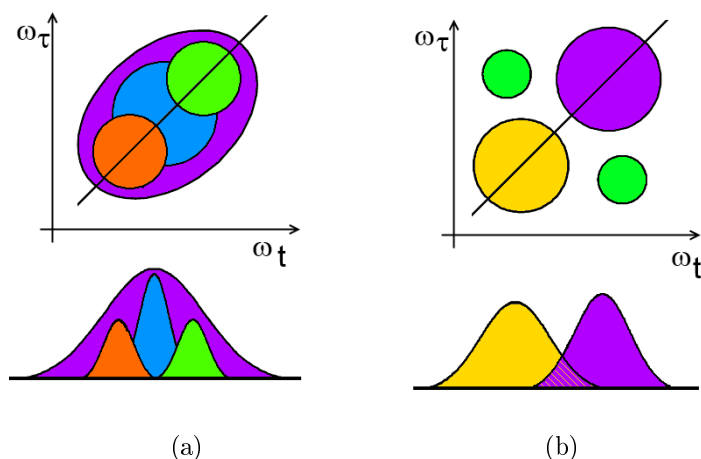
(a)   (b)

Figure 1.2: Schematic showing the congestion of absorption spectra
(bottom) and the extra information carried by the 2D spectra (top) in
two different cases: (a) broadening of the spectra due to coupling of the
molecules with the environments. (b) Coupling between two electronic
excitations within the molecules. Figure modified from Ref.[84].

ing linear spectroscopy, including transient absorption, can be illus-
trated using two examples:

- Broad lineshapes. Whether a feature is a homogeneous line-
  shape broadened by fast irreversible relaxation, or an inhomo-
  geneous lineshape arising from a static distribution of different
  frequencies is difficult to determine, given that linear spectra
  cannot uniquely interpret line-broadening mechanism, or decom-
  pose heterogeneous behavior in the sample. See Fig.1.2(a).

- Absorption spectrum with two peaks. Do these resonances arise
  from different, non-interacting molecules, or are these coupled
  quantum states of the same molecule, given that couplings or
  spectral correlations cannot be directly resolved? See Fig.1.2(b).

Linear spectroscopy and pump-probe do not offer systematic ways to
attack these types of problems. Linear spectroscopy also has no abil-
ity to interpret dynamics and relaxation. These issues become more
urgent in the condensed phase, when lineshapes broaden and spectra
are congested. Nonlinear spectroscopy techniques like 2D spectroscopy
provide a way of resolving these scenarios, as they uses multiple light
fields with independent control over frequency or time-ordering in or-
der to probe correlations between different spectral features, and the
time evolution of the system under study.

15

Photon echo is a "time-resolved optical spectroscopy in which the inhomogeneous broadening of absorbers is eliminated by the proper choice of geometry in a four-wave mixing experiment."[85] This is mathematically equivalent to the spin-echo in NMR spectroscopy.[86–88] Photon echo differs from other third-order processes due to the time ordering of the field interactions.[87] In photon echo, this generates rephasing[86] in the polarization, thus removing inhomogeneous contributions to the absorption linewidth.[85]
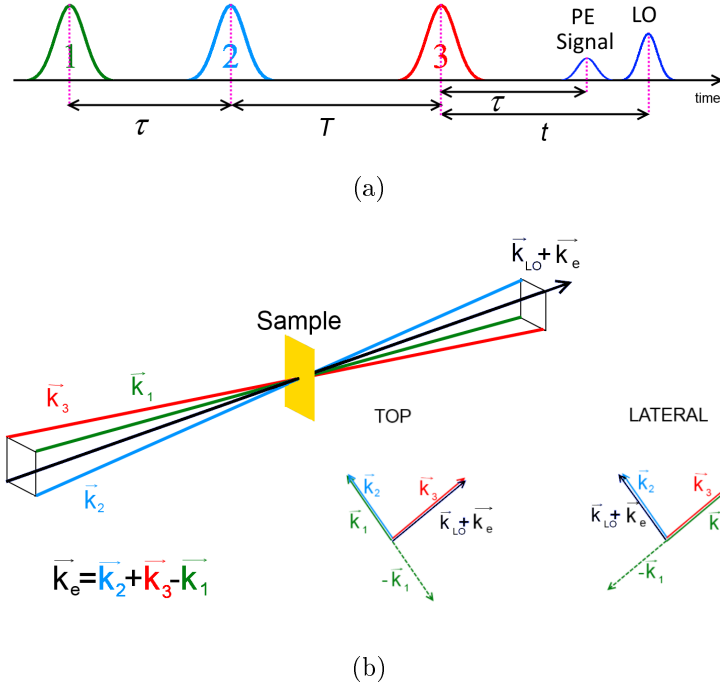

(a)

(b)

Figure 1.3: Schematic showing the time-ordering (1.3(a)) and the phase-matching conditions (1.3(b)) in a box-car geometry type of photon echo spectroscopy.

PE spectroscopy employs three different pump pulses and one probe pulse, all delayed in time, as shown in Fig. 1.3(a). In a molecular system, a coherence is created after the first pulse interacts with the molecules, or in other words, the first pulse prepares the system in an excited quantum state. Thus the dipoles of the molecules start oscillating. Due to interaction with the solvent, the frequencies of the oscillators are slightly different, inducing a dephasing between them. After a delay time τ a second pulse induces a second interaction that reverts all the phases of the oscillations, applying a $-\pi$ phase inversion. Ideally after the time delay $T = \tau$, when a third interactions is induced, all the dipoles are again oscillating in phase. The delay time

16

τ is called phasing time, recalling its task of phasing the dephased oscillators. The delay time T is called population time, to highlight that there is still a difference of population of electrons (or other quantum particles) between the ground state and the excited state. The third time t is called detection time, and this is literally the time when the signal is (experimentally) detected, it is also sometimes called emission time. The physical process described above is possible only because the three pump pulses (the first three pulses in Fig. 1.3(a)) are properly phase-matched[86], this is assured by the use of proper geometric configurations of such pulses. The most commonly used ones are the pump-probe scheme and box-car geometry.[86] In this thesis work the box-car geometry was used, as depicted in Fig. 1.3(b). Here the three pump pulses are emerging at the corners of a square, and the fourth corner gives the direction of the signal, and this is also the direction of the LO pulse. This geometry automatically ensures the preservation of the phase-matching between all the pulses.

From an experimental point of view, in 2D spectroscopy one detects the electric field emitted by an induced third-order polarization as a function of coherence time τ and detection time t.[86] The population time T is the mathematical and physical equivalent to the delay time in transient absorption spectroscopy. The detection can be done in a homodyne or heterodyne fashion, the advantage of the latter is that the signal to noise ratio is improved as the white noise is canceled. In heterodyne detection the generated signal is mixed (spatially but not temporally overlapped) with a strong reference pulse called a local oscillator (LO), the detector receives the interference between the electromagnetic field of the signal and of the LO. The original signal, a complex spectral field, is then retrieved using the method of Lepetit.[89]

The reader can find a comprehensive mathematical treatment of the nonlinear concepts of this section in the text books of Cho[87] and Hamm and Zanni.[86]

1.5 Chemical structure of nucleobases and *DNA* and their notation

Deoxyribonucleic acid (*DNA*) carries the genetic instructions used in the growth, development, functioning and reproduction of all known

living organisms and many viruses. *DNA* is a nucleic acid first isolated by Friedrich Miescher in 1869.[90] Its molecular structure was identified by James Watson and Francis Crick in 1953[63], whose model-building efforts were guided by X-ray diffraction data acquired by Rosalind Franklin. Most *DNA* molecules consist of two biopolymer strands (*ssDNA*) coiled around each other to form a double helix (Fig. 1.4). The two helices, also called strands, are bound by hydrogen bonding forces.
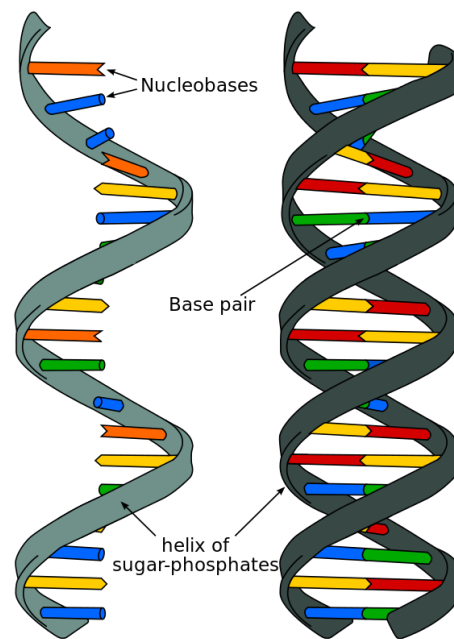

Figure 1.4: Schematic of single and double stranded DNA, image taken from wikipedia[72].

The two *ssDNA* are termed polynucleotides since they are composed of simpler monomer units called nucleotides.[91,92] A nucleotide is composed of a nitrogenous base, a five-carbon sugar called deoxyribose, and at least one phosphate group. A nucleoside is a nitrogenous base and the deoxyribose sugar. Thus, a nucleotide is formed by a nucleoside and a phosphate group.

In *DNA*, the nucleotides are joined in a chain by covalent bonds between the deoxyribose of one nucleotide and the phosphate of the next, resulting in an alternating sugar-phosphate backbone. There are four single natural (un-modified) bases in *DNA* (see Fig. 1.5. Two of them are purines: guanine (G or Gua), and adenine (A or Ade). The other two are pyrimidines: thymine (T or Thy) and cytosine (C or Cyt). When these bases are linked to the deoxyribose sugar, they

become ribonucleosides, and in particular they change their name into guanosine (Guo), adenosine (Ado), 5-Methyluridine (m^5U) and Cytidine (C). When the OH group at the position $2'$ of the sugar ring (the bottom right one of the two) is removed, the molecules become deoxyribonucleosides, and they are called dG, dA, dT, and dC. Lastly, when one or more phosphate groups are added to the fourth position of the sugar ring, the molecules are called deoxynucleoside n-phosphate, where n stands for the number of phosphate groups present. Therefore dATP is deoxyadenosine triphosphate, dAMP is deoxyadenosine monophosphate, and so on.

With respect to single strands of DNA, one should distinguish between homogeneous and inhomogeneous $ssDNA$. Homogeneous $ssDNA$ are composed of the same type of nucleobases, e.g. poly-A or poly-T. On the contrary, inhomogeneous $ssDNA$ are strands composed of different bases, e.g. A-T repeats. Moreover, the composition and length of the sequence can be specified as follows: $(dX)_n$ where X is one of the four bases (A, T, C or G) and n is the number of bases. As an example, the single strand $5'$AAA AAA AA$3'$ is called $(dA)_8$, and the strand $5'$ATA TAT$3'$ is called $(dAT)_3$. In order to specify that the molecule is a double strand, a dot between the two single strands can be added; for instance the $dsDNA$ $5'$AAA AAA AA$3'$ hybridized with $5'$TTT TTT TT$3'$ is called $(dA)_8 \cdot (dT)_8$.

(a) Ade   (b) Ado

(c) Cyt   (d) Cyd
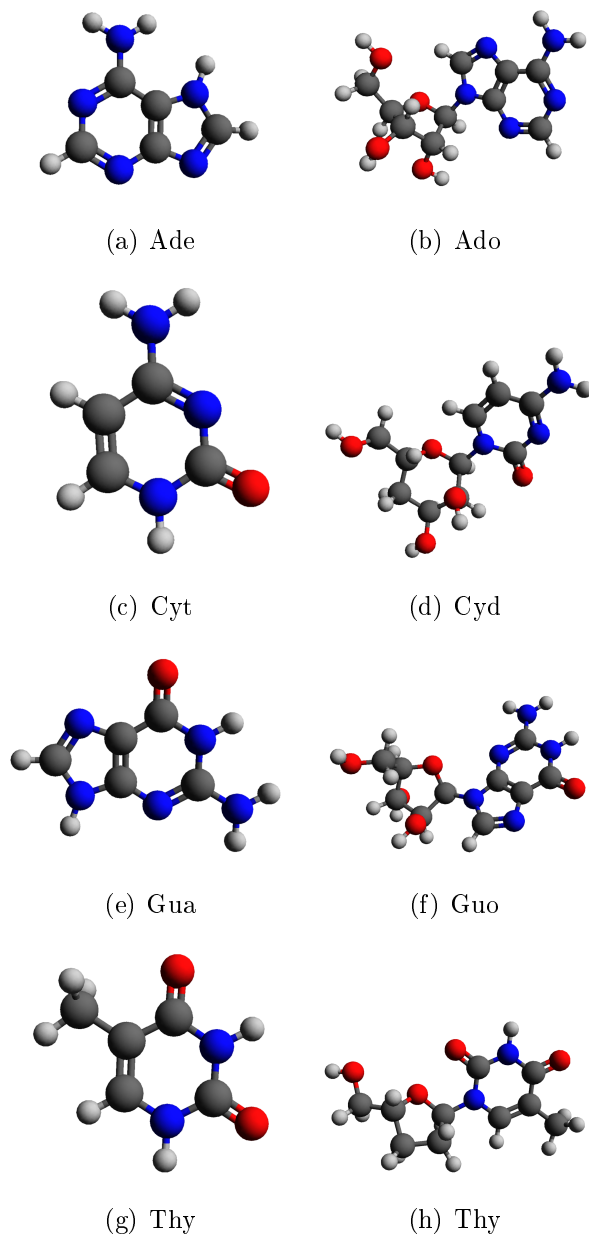
(e) Gua   (f) Guo

(g) Thy   (h) Thy

Figure 1.5: Ground state equilibrium chemical structure of several nucleobases. 1.5(a) Adenine, 1.5(b) Adenosine, 1.5(c) Cytosine, 1.5(d) Cytidine, 1.5(e) Guanine, 1.5(f) Guanosine, 1.5(g) Thymine, 1.5(h) 5-Methyluridine.
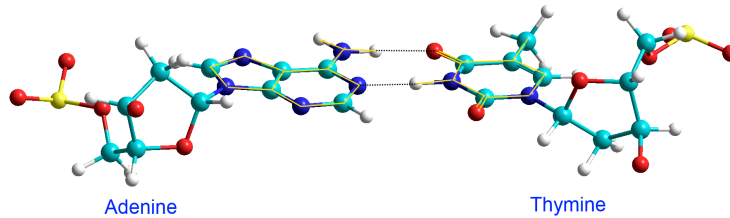
1.6   H- and J- aggregates

H- and J-aggregates are historically linked to the self-association of
dyes in solution, due to the very strong van der Waals and hydrogen
bonding intermolecular forces between two molecules (the monomers).
The aggregates exhibit distinct changes in their spectral properties
compared to monomers; these changes can be detected by absorp-
tion and circular dichroism spectroscopy. In addition to the opti-
cal density and the dipole strength mentioned earlier, the absorp-
tion spectra can reveal the presence of interactions between stacked
bases in the *ssDNA*, from which excitons arise. When comparing
monomer and multimer (aggregates) spectra, the absorption peaks
shift and the absorption bands narrow. Two diametrically different
situations have been proposed. The peaks are either bathocromically
shifted (J-aggregates), or hypsochromically shifted (H-aggregates). A
bathochromic shift, from Greek "deep color"[72], is the shift of the
positions of peaks to longer wavelengths, also called "red shift". A
hypsochromic shift, from Greek "height color"[72], is the shift of the
positions of the absorption peaks at shorter wavelengths, therefore
also called "blue shift". These shifts are illustrated in Fig. 1.6, where
thymine and adenine are used as monomers. In Fig. 1.6(b) an adenine
and a thymine monomer are linked through the phosphate backbone,
forming a *pi*-stack between their dipole moments. In Fig. 1.6(c) the
thymine and the adenine are hydrogen bonded, and the dipole mo-
ments are disposed in a parallel fashion. The stacking of the dipole
moments causes the shift of the peaks to be blue (left, H-aggregate) or
red (right, J-aggregates)[93,94], as shown in the energy level diagram of
Fig. 1.6(a), where only the higher (blue-shift) or lower (red-shift) tran-
sitions are respectively allowed for the H-aggregate and J-aggregate.

Excitons, firstly introduced by Frenkel[32,95], are defined as current-
less collective excitations, which correspond to a change in the state
of motion of loosely bound electrons of the monomers in an aggre-
gate.[96,97] They consist of an excited electron and a hole in a different
monomer in the aggregate, which are coupled together by electrostatic
forces.[98] The energy splitting in Fig. 1.6(a), and the subsequent peak
shift, arise from exciton coupling[99], and in particular the arrangement
of the two dipoles and symmetry rules that eliminate one of the two
possible transitions. In *pi*-stacked monomers, the two dipoles are out-
of-phase and correspond to a lowering of energy as compared to the
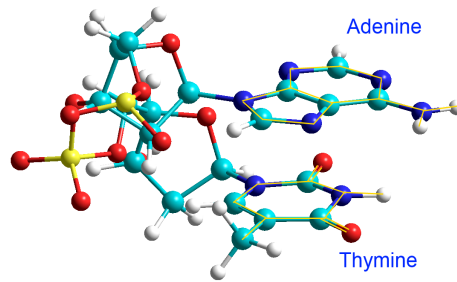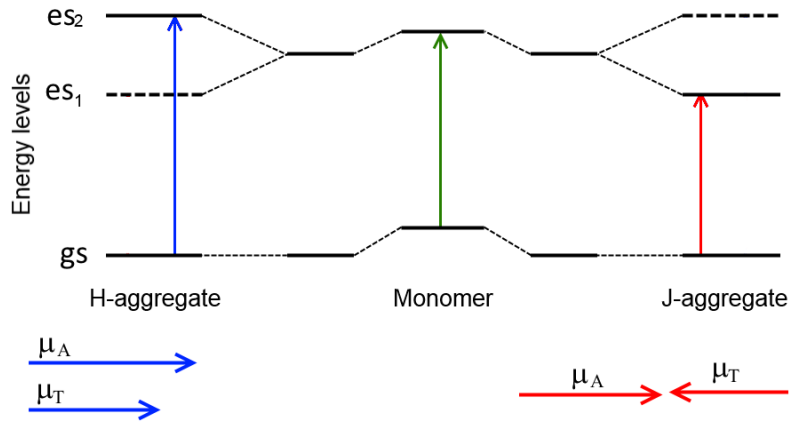
(b) (dAT)

(c) $(dA \cdot dT)$

Figure 1.6: (a) Energy diagram representing the energy shift of H- and J- aggregates with respect to the monomer, image modified from Katoh et al.[93] Examples of (b) H-aggregate and (c) J-aggregate in *DNA*. (b) An adenine and a thymine monomers are linked through the phosphate backbone forming a $pi - pi$ stack between their dipole moments. (c) The thymine and the adenine are hydrogen bonded and the dipole moments are disposed in a parallel fashion.

van der Waals displaced states of the component molecules.[100] As the transition moment is the vector sum of the two transition moments, only the higher energy level es$_2$ is allowed. The opposite holds true for parallel-stacked monomers. The two energy levels are due to Davydov splitting[96,99], a result of a weak dipole interaction between the stacked monomers in the aggregate. The splitting can be used to calculate the electronic coupling V whose upper limit for symmetric systems is[101]:

$$|V| = \frac{\Delta E_{mn}}{2} = \frac{|E_m - E_n|}{2}. \tag{1.12}$$

A mathematically rigorous treatment of excitons can be found in Davydov.[96,99] As a final remark, while $ssDNA$ is an H-aggregate polymer, $dsDNA$ is usually a mixture of both H- (the two single strands) and J-aggregate, therefore complicating the model further.

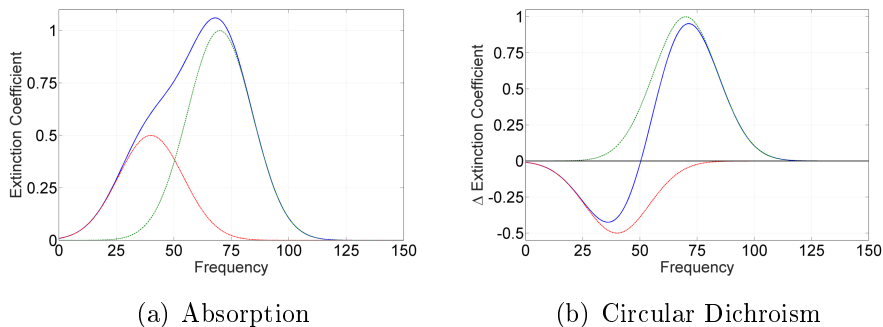|	
(a) Absorption	(b) Circular Dichroism

Figure 1.7: Representative nucleobase absorption (left) and circular dichroism (right) spectra of a model dimer that mimics the spectra of an H-aggregate. The spectra were obtained by summing (absorption) or subtracting (circular dichroism) two Gaussians centered at 40 and 70 frequency units, with 0.5 and 1 extinction coefficient units respectively and 20 frequency units width each.

The interaction between stacked monomers, as in $ssDNA$ manifests as three effects in absorption and CD spectra. First, the absorption peak shifts in $ssDNA$ spectra with respect to the nucleobase spectra, as explained above. Second, the absorption bands narrow.[100] Third, in CD spectra, evidence for excitons originating from stacked-based interactions manifests as the Cotton, or so-called "butterfly", effect (Fig. 1.7). This is a zero-crossing (nodal) point of the CD spectrum that corresponds to an absorption band. The full butterfly shape, made by two bands in the CD spectrum, correlates with two transition dipole moments of opposing sign that arise from excitonic electronic-level

splitting. The Cotton effect in *DNA* can be understood by using the definition in Eq. 1.4. *ssDNA* has its nucleobases disposed in a right-handed helix. At shorter wavelengths, near the nodal point, the dipole moments of interacting bases are almost parallel, creating a combined exciton state; here the right-hand polarized light is most strongly absorbed. At longer wavelengths, the dipole moments are directed almost opposite to each other, therefore there is a strong absorption of left-hand polarized light and hence the positive Cotton effect. The opposite is true for a negative Cotton effect, where the left-handed polarized light is most strongly absorbed at shorter wavelengths, and right-handed polarized light is most strongly absorbed at longer wavelengths.

As an example of dimerization, the formation of dimers, Rhodamine 6G(Rh6G) was employed, a dye that self-dimerizes at high concentrations. Rh6G is a xanthene derivative with a strong transition dipole moment and an absorption spectrum in the visible ($400 \approx 600 \, \text{nm}$), as shown in Figure 1.8. Here Rh6G was dissolved in double distilled water (ddw). The concentration was determined using the measured absorption spectrum and the extinction coefficient from literature.[102]
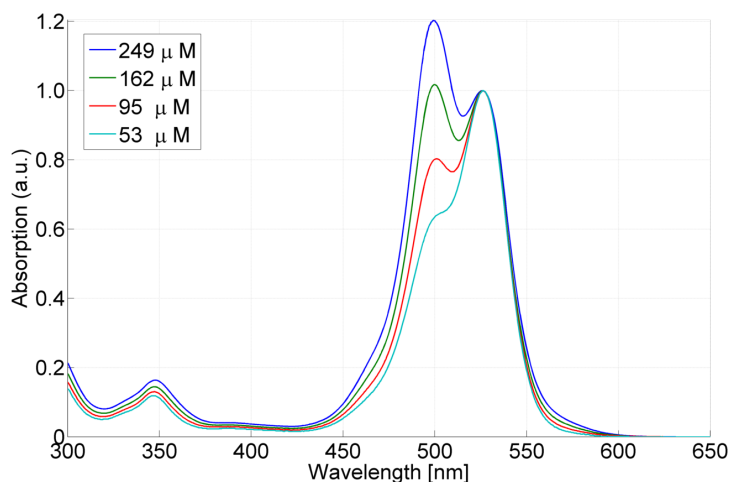
Figure 1.8: Absorption spectrum of rhodamine 6G at different concentrations, normalized to the max value of the peak at $530 \, \text{nm}$. Note that the peak at $500 \, \text{nm}$ is increasing in magnitude while the concentration increases, showing clearly the dimerization of rhodamine 6G.

From Fig. 1.8, one notices that the peak at $500 \, \text{nm}$ rises as the concentration is increased. This effect is a sign of dimerization, as shown in the literature.[103,104] Given the effects of dimerization on the

absorption spectra, the self-dimerization of nucleobases can be investigated when their solutions are very concentrated, as described in the following section. The exact formation of self-assembling dimers and Rh6G dimers is out of the scope of the present section, but a curious reader can find more information in Refs.[94,104]

Chapter 2

Selection and characterization of biological samples

In order to uncover excitonic signatures using 2D spectroscopy, it is critically important to select the *DNA* sample that shows the strongest evidence of excitonic behavior; the samples with the strongest characteristics will be studied with non-linear optics (NLO). This was achieved by a systematic investigation of various nucleotides and *ss-DNA* using absorption and circular dichroism (CD) spectroscopy. The content of this chapter is partly reproduced from a paper to be submitted; the authors are A. Picchiotti, M. Kochman, V. I. Prokhorenko and R. J. D. Miller. The simulations presented in this chapter were performed by M. Kochman.

2.1   Introduction

Unraveling the excitation dynamics of *DNA* is essential to understanding certain pathologies, such as the influence of UV light on cancer formation.[1] It has been theorized that UV light induces the formation of excitons in *DNA*; these could be formed either on the hydrogen-bonded base pair and/or between adjacent bases along the *DNA* backbone.[6,7,105] It is thought that the appearance of excitons signals the presence of long-lived photoexcited states in *DNA*.[39,106] The slow decay of these excited states increases the chance that excess energy will dissipate via higher-energy deactivation pathways, possibly resulting in photo-induced biological damage and conditions such as cancer. Although extensive effort has gone into investigations in this area[3,5,6,13], definitive exciton signatures in *DNA* have remained

elusive and sometimes contested.[13,42] In contrast, single nucleobases are devoid of excitons and decay quickly and safely via non-radiative pathways.[42,105] Clearly, it is vital to identify the spectroscopic signatures of and discern the role of excitons on the excited-state lifetimes in DNA.

Non-linear spectroscopic tools, such as transient absorption (TA) and two-dimensional photon echo (PE) spectroscopy, can identify exciton-transfer pathways and, moreover, interactions between the DNA bases. However, before performing such involved measurements, the DNA strands that show the strongest evidence of excitonic behavior must be identified. To simplify matters, the focus of this work was on detecting interactions between stacked nucleobases in single-stranded DNA ($ssDNA$), which are predominantly H-aggregate in character, and lack the contribution of the Watson-Crick hydrogen bond in double-stranded DNA. In the present section, two different families of homogeneous $ssDNA$ were selected, meaning a single strand of DNA composed of the same type of nucleobases, e.g. $d(A)_4$. Those two families were chosen to represent purines (adenosine-homo oligomers) and pyrimidines (thymine-homo oligomers).

The primary tools were absorption and circular dichroism (CD) spectroscopies at UV wavelengths around $260\,\mathrm{nm}$ where nucleobases and $ssDNA$ exhibit strong optical responses.[82,107–109] In particular, CD is very sensitive to structural changes upon UV-light irradiation.[110] The comparison of single nucleobases with chains of nucleobases (as $ssDNA$) aims to find the signatures of excitonic behavior, as explained in Sec. 1.3. Moreover, the transition dipole strength and extent of the spatial delocalization of excitons was analyzed. This approach aimed to identify the most promising $ssDNA$ candidate for further research into the intricate role that exciton dynamics have on long lifetimes in DNA.

The DNA was scrutinized for evidence of excitonic signatures, based upon a set of specific parameters, including length and nucleobase sequence. As already mentioned, the investigation was limited to $ssDNA$ to avoid base-pair interactions. These interactions would obscure the excitons which are delocalized along the same strand of DNA due solely to the H-aggregation of nearby nucleobases. The $ssDNA$ was kept relatively small, 2 to 20 bases, to minimize the complexity of the system.

The material is organized as follows. In section 2.2 and 2.3, after

a brief description of sample preparation and acquisition of data, the methodology used to analyze the spectra is described. In sections 2.6 and 2.7, the experimental absorption and CD spectra are presented, as well as their analysis, where the results from different samples are compared.

2.2   Buffer selection and preparation

This section introduces some basic concepts of chemistry required to understand the effects of a buffer on the solutions. Moreover, it describes the buffer chosen for the set of experiments presented in this thesis.

In order to maintain a constant pH in a solution, it is necessary to use a solvent able to absorb an excess of protons ($[H^+]$) or hydroxide anions ($[OH^-]$) that occurs as a result of production or uptake of protons by the system. A buffer is a water-based (aqueous) solution of a weak base and its conjugated acid, or a weak acid and its conjugated base. The purpose is to maintain the set pH stable, even when adding acids or bases in small or moderate amounts. When a weak acid [HA] and its conjugated base [A$^-$] are mixed together, a chemical equilibrium is reached:

$$HA \rightleftharpoons H^+ + A^-$$
(2.1)

where the equilibrium constant is pK_a is given by:

$$pK_a = -Log\left(\frac{[\text{HA}]}{[\text{A}^-][\text{H}^+]}\right)$$
(2.2)

where the square parentheses indicate the concentration (activity) (in $M := mol/liter$) and Log is the log_{10}. This leads to the Henderson-Hasselbalch equation for a monoprotic reaction:

$$pH := -Log[\text{H}^+] = pK_a - Log\left(\frac{[\text{HA}]}{[\text{A}^-]}\right)$$
(2.3)

Monoprotic acids are defined as being able to donate only one proton per molecule during the process of full dissociation, in contrast to polyprotic acids that can donate more than one proton per molecule. In conclusion, given the values of pK_a it is possible to calculate the concentration of an acid and its conjugated base necessary to prepare the desired buffer.

Molecule	Site	Nucleoside	$3'-$Phosphate
Adenosine	N1	3.52	3.70
Cytidine	N3	4.17	4.43
Guanosine	N1	9.42	9.84
Uridine	N3	9.38	9.96
2'-Deoxythymidine	N3	9.93	-

Table 2.1: pK_a values for bases in nucleosides and nucleotides, redacted from Saenger[111]. For an explanation of $N1$ and $N3$ sites, see section 1.5.

Using a buffer is of particular importance for nucleobases and DNA due to their propensity to protonate and deprotonate with time, once they are solvated. The pK_a value of DNA nucleobases can be seen as the propensity to lose a proton to the environment; the values reported in table 2.1 are taken from Saenger.[111] Adenosine and cytidine tend to become acidic when in aqueous form, whereas guanosine and thymidine tend to become basic.

The pH of distilled desalted water (ddW) is theoretically 7, but due to the presence of carbon dioxide in the air drops to approximately 5.5 as soon as water drips from the distillation machine into a container, as described by the following chemical reaction:

$$CO_2 + H_2O \xrightleftharpoons{pK_{a1}} HCO_3^- + H^+ \xrightleftharpoons{pK_{a2}} CO_3^{2-} + 2\,H^+ \qquad (2.4)$$
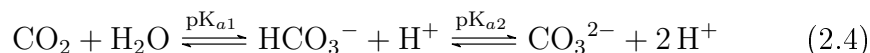
H_2CO_3 is very rapidly converted into HCO_3^- and dissolved $CO_2(aq)$ is often present, as carbonic acid, when in equilibrium with carbon dioxide, at a much lower concentration than $CO_2(aq)$. In this case, the equilibrium constant is $pK_{a1} = 6.3$.[112] For the reaction step that produces CO_3^{2-}, the equilibrium constant is $pK_{a2} = 10.32$.[113] By referring to the partial pressure p_{CO_2}, it is possible to find the concentration of the different species in the water for $pH = 5.65$:

$$CO_2 = 1.18\,10^{-5}\,M \qquad (2.5)$$

$$H_2CO_3 = 2.00\,10^{-8}\,M \qquad (2.6)$$

$$HCO_3^- = 2.23\,10^{-6}\,M \qquad (2.7)$$

$$CO_3^{2-} = 5.60\,10^{-11}\,M \qquad (2.8)$$

Due to their very low concentrations, it is safe to ignore the second and the last of the species in future calculations. The final buffer strength

(its concentration) is of the order of tens of milliMolar, and thus the first and third terms can also be ignored as they are four orders of magnitude less important.

In the literature, one finds a staggering variety of buffer recipes for different pH values and with different strengths and chemical components. Nevertheless, to set the desired pH value at 7, the most commonly used buffers are based on phosphate molecules.[39,107,114–119] The References[120–122], specify the details of the buffers: di-sodium phosphate (Na_2HPO_4) and mono-sodium phosphate (NaH_2PO_4), adjusting the pH with sodium chlorate ($NaClO_3$). Aside from sodium chlorate, which was unneeded, we used the same chemicals to prepare the buffer for the experiments.

In a buffer composed by di-sodium phosphate and mono-sodium phosphate, NaH_2PO_4 acts as the weak acid and Na_2HPO_4 as the conjugated base:

$$H_2PO_4{}^- \rightleftharpoons HPO_4{}^{2-} + H^+ \qquad (2.9)$$
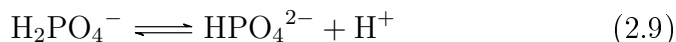
The pK_a is 7.21. Considering that the desired pH is 7, the percentage of mono-sodium phosphate ($MW = 120\,\texttt{g/mol}$) needed is 5.8362% m/v and of di-sodium phosphate ($MW = 141.96\,\texttt{g/mol}$) is 15.466% m/v.

The two salts were purchased from Sigma Aldrich and used without further purifications. They are in the following hydrate versions: mono-sodium phosphate mono-hydrate and di-sodium phosphate hepta-hydrate. Due to the presence of extra water molecules, one has to adjust the previous percentages accordingly. In particular, the molecular weight of $Na_2HPO_4 \cdot 7H_2O$ is $268.07\,\texttt{g/mol}$, while that of $NaH_2PO_4 \cdot H_2O$ is $138\,\texttt{g/mol}$. The percentages of the two aforementioned salts in the buffer solution respectively become 8.19% m/v and 5.08% m/v.

Experimentally, in $100\,\texttt{ml}$ of ddw the following quantities were dissolved: $8.20\,\texttt{g}$ of $Na_2HPO_4 \cdot 7H_2O$ and $8.84\,\texttt{g}$ of $NaH_2PO_4 \cdot H_2O$, leading to a buffer at pH 7.13 and with $1\,\texttt{M}$ strength. The buffer was thereafter filtered, with filters with $0.2\mu m$ pore size, and kept at $-20°C$ in small aliquots. When needed, the buffer was thawed and diluted to $10 - 20\,\texttt{mM}$, and the pH was checked every time after dilution.

2.3 Preparation of the samples

The dependence of the UV-absorption spectra of *ssDNA* upon its composition[123], due to bases interacting dissimilarly with each other, adds another layer of complication. Hence, homogeneous strands, or so-called homo-oligomers, of the nucleobases adenosine and thymidine, referred to as $(dA)_n$ and $(dT)_n$, respectively were used. Here n defines the number of bases of each type per homo-oligomer.

The nucleobases and the *ssDNA* strands were purchased from Jena Bioscience GmbH in lyophylized (*ssDNA*) and powder (nucleobases) forms and used as received. The nucleobases were solvated in double distilled water (ddW) and used without any filtering. Desalting and purification of the *ssDNA* were performed by the vendor. The strands were solvated in a phosphate-based buffer, made from desalted and distilled water, and filtered through 0.1 μm polypropylene syringe filters. For each sample, the *pH* was neutral (approximately 7). The solute concentrations of the *ssDNA* solutions were adjusted such that the maximum absorbance at 260 nm was between 0.5 and 1 for each absorption and CD measurement. The absorption measurements were performed using a *UV2600* spectrophotometer from Shimadzu Corp. CD spectra. A second comparison set of absorption spectra were acquired on a Chirascan-plus circular dichroism spectrometer from Applied Photophysics Limited. Each scan was performed with a resolution of 0.5 or 1 nm and an accumulation of 2 seconds. The spectra of the samples were measured in Hellma quartz cuvettes with path lengths of 0.1 cm and 1 cm.

2.4 Treatment of the absorption and CD spectra of *ssDNA*

To retrieve the dipole moment from the absorption spectra, one has to integrate Eq. 1.3, and the spectral peaks must be fitted accurately with Gaussian functions. However, when multiple transitions occur too near in wavelength to be distinguishable in the experimental spectra, the peaks partially overlap. Then it becomes necessary to use multiple Gaussians to fit the spectral lines, with some starting guesses of the fitting parameters, in order to increase the quality and speed of the fitting. This is shown for adenosine and thymidine strands in

appendix A.2, in figures A.1 and A.2, respectively. The fitting starts from $210\,\mathrm{nm}$ due to the experimental limitations of the quartz cuvettes. The results of this fitting routine, with peak wavelengths and μ^2, are given in Table 2.2.

Sample	MW [g/mol]	ε_{260} [$\mathrm{M^{-1} \cdot cm^{-1}}$]	pH (± 0.05)	c [μM]	First Gaussian λ_{peak} ($\pm 0.5\,\mathrm{nm}$)	μ^2 [$\mathrm{D^2}$]	Second Gaussian λ_{peak} ($\pm 0.5\,\mathrm{nm}$)	μ^2 [$\mathrm{D^2}$]
$dATP$	611	15100	6.84	98.7	263.3	7.87	249.6	8.84
$(dA)_2$	564	31000	7.09	230.1	260.2	24.04	236.8	26.00
$(dA)_4$	1191	61000	7.05	131.2	261.0	40.55	240.3	48.14
$(dA)_6$	1817	92000	7.11	94.3	258.7	90.33	235.5	50.03
$(dA)_8$	2444	122000	7.09	58.9	258.6	117.61	235.3	72.72
$(dA)_{10}$	3070	153000	7.22	55.6	257.1	175.58	233.7	58.36
$(dA)_{15}$	4636	230000	7.08	30.1	257.0	265.29	234.1	59.07
$(dA)_{20}$	6202	306000	7.10	34.0	256.9	350.02	234.4	71.27
$dTTP$	602	9600	6.96	186.5	274.1	5.13	258.4	8.24
$(dT)_2$	546	19000	6.97	469.7	272.6	9.72	257.5	15.87
$(dT)_4$	1155	37000	7.04	191.8	272.7	18.71	257.6	30.84
$(dT)_6$	1763	56000	7.11	138.8	272.5	28.04	257.5	46.76
$(dT)_8$	2372	74000	7.09	104.7	272.6	36.30	257.8	63.91
$(dT)_{10}$	2980	93000	7.19	81.8	272.8	44.68	257.8	79.31
$(dT)_{15}$	4501	140000	7.08	87.5	272.7	65.71	257.8	116.84
$(dT)_{20}$	6022	186000	7.12	40.5	272.5	88.17	257.6	157.38
(dAT)	555	25000	6.98	277.3	262.7	22.86	233.47	20.09
$(dAT)_2$	1173	49000	7.13	120.2	262.6	46.26	238.10	27.30
$(dAT)_5$	3025	123000	7	55.4	262.8	119.16	235.4	82.51
$(dAT)_{10}$	6112	246000	7.01	26.06	266.5	187.54	246.9	177.15

Table 2.2: Various parameters and values for the family $(dA)_n$ and $(dT)_n$. The molecular weights (MW) and extinction coefficients (ε_{260}), at $260\,\mathrm{nm}$, were given by the manufacturer[124], whereas pH was measured. The absorption peak wavelengths (λ_{peak}) emerge from fits to the measured absorption spectra, while the sample concentrations (c) and dipole strengths (μ^2 in units of Debye squared D^2) are calculated from these same spectra. See text for details of the data-extraction techniques used.

Furthermore, CD spectra can reveal the extent of exciton delocalization in oligomeric chains. If one assumes that the basic element of the chain is a dimer, increasing the number of dimers leads to two possible kinds of behavior, as shown in Fig. 2.1: at the top, the basic

elements ignore each other, so the contribution to the CD signal is only the product of the dimer signal with the number of dimers. At the bottom of Fig. 2.1, the elements interact, and the CD signal is composed of the preceding non-interacting dimer signal together with the dimer-interaction signal. To separate these two cases, the normalized peak values of the negative and positive bands of a butterfly-shaped CD spectrum were subtracted for different $ssDNA$ lengths. In the first case, where excitons are localized solely among nearest neighbors, the relative strength of the CD signal does not increase as the number of bases per DNA strand increases. In the second case, where excitons are delocalized over more than one dimer, an increased value is expected as the number of bases per strand increases. Qualitatively, as the slope increases, so does the extent of the spatial delocalization.
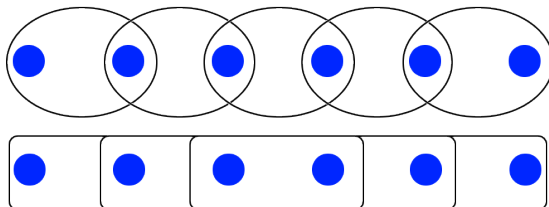
Figure 2.1: Image showing (top) the interaction of the monomers only with nearest neighbors, and (bottom) the interaction of the monomers with next-to-nearest neighbors. The filled circles represent the monomers.

To be able to compare different sets of absorption and CD spectra, with different sample concentrations, it is necessary to perform a normalization, through the following relationship:

$$[x(\lambda)] = x(\lambda)/OD(\lambda_0), \tag{2.10}$$

where $[x(\lambda)]$ and $x(\lambda)$ are, in the case of absorption, the normalized and the experimental values of the optical density or, in the case of CD degrees of ellipticity, while λ_0 is the wavelength of the band around $260\,\mathrm{nm}$.

Within the frame of Van Vleck theory, exciton coupling can be extracted from absorption and CD spectra, overcoming the effect of inhomogeneous broadening. Burin et al. derived the sum rules for the absorption and CD spectra of polymer molecules[125], and applied this to DNA hairpins. The same general results were used here for

calculating the nearest-neighbor and the second-to-nearest-neighbor contributions of the exciton coupling of the samples in this study. Summarizing the results of Burin, the following equation was applied:

$$V_0 = \frac{2}{\ln(10)} \frac{n}{n-1} \frac{\hbar c}{d \, n_r \, \sin(\phi)} \frac{\int_\infty^\infty \mathrm{d}E \frac{CD(E)}{E}}{\int_\infty^\infty \mathrm{d}E \frac{OD(E)}{E}} \qquad (2.11)$$

where n is the number of monomers composing the polymer, n_r is the refractive index, d is the distance between two monomers along the axes, ϕ the angle between their the dipole moments, $CD(E)$ is the energy dependent ellipticity angle in radians (the CD spectrum) and $OD(E)$ is the energy dependent absorbance.

2.5 Simulation methods

The oligonucleotide molecules studied in the present work are too large to be included in electronic structure calculations in their entirety. Taking advantage of the fact that the photoabsorption and CD spectra of DNA molecules are dominated by $\pi\pi^*$-type transitions predominantly localized on the nucleobase moieties, in our simulations we represented the oligonucleotides by reduced models which explicitly included only the nucleobase moieties. Each such model was constructed by positioning a number of nucleobase molecules in an idealized B-DNA-like arrangement. The geometry of each individual nucleobase was taken as the ground-state equilibrium geometry of the isolated molecule as optimized at the the density functional theory (DFT) level. The optimization was performed with the use of the M06-2X functional[126] in combination with the Pople 6-31G(d) basis set.

It has been previously demonstrated[127,128] that for vertical excitation spectra of π-stacked nucleobase clusters, the time-dependent density functional theory (TDDFT) formalism with the M06-2X functional provides reasonably good agreement with benchmarks provided by correlated wavefunction-based methods, such as the second-order algebraic diagrammatic construction (ADC(2)) method[129,130], and an equation of motion coupled cluster including perturbative triple excitations (EOM-CCSD(T)).[131,132] Therefore, the vertical excitation spectra and CD spectra were calculated at the M06-2X/6-31G(d) level of theory, as implemented in the computational chemistry software package Gaussian 09, Revision D.01.[133] The effects of aqueous solva-

tion on the excited states of the oligonucleotide models were included through the continuous surface charge implementation of the polarizable continuum model (CSC-PCM).[134,135] Nonequilibrium, linear response solvation was imposed. A dielectric constant of $\varepsilon = 78.3553$ was used for the aqueous solvent and, as per default, the solute cavity was constructed as a set of overlapping spheres centered at the solute atoms, using the universal force field atomic radii scaled by a factor of 1.100.

2.6 Absorption spectroscopy of nucleobases: concentration tests

This section presents the experimentally collected absorption spectra of a diverse group of DNA nucleobases (with and without modifications) at different concentrations. The goal of this particular research is a systematic study of the single bases in order to better characterize them before performing nonlinear spectroscopy (pump-probe and photon echo, see Ch. 6).

At the beginning of the project an initial question was tested: is the self-dimerization of nucleobases in solution possible? To address this, the absorption spectra of four single nucleobases dissolved in water were collected, at $pH \approx 7$ and at different concentrations. Dimerization would be visible in the absorption spectra as the appearance of peaks not present in the spectra of the monomer, representing interactions between molecules (inter-molecular interactions).

Knowledge of the absorption properties of nucleobases is fundamental, not only as complementary information for time-resolved spectra, but also to ensure that the molecule studied is not protonated or deprotonated (changing of pH), and it is not dimerizing (possible by increasing the concentration). By gradually increasing the concentration and comparing the absorption spectra it is possible to uncover extra peaks arising from inter-molecular interactions.
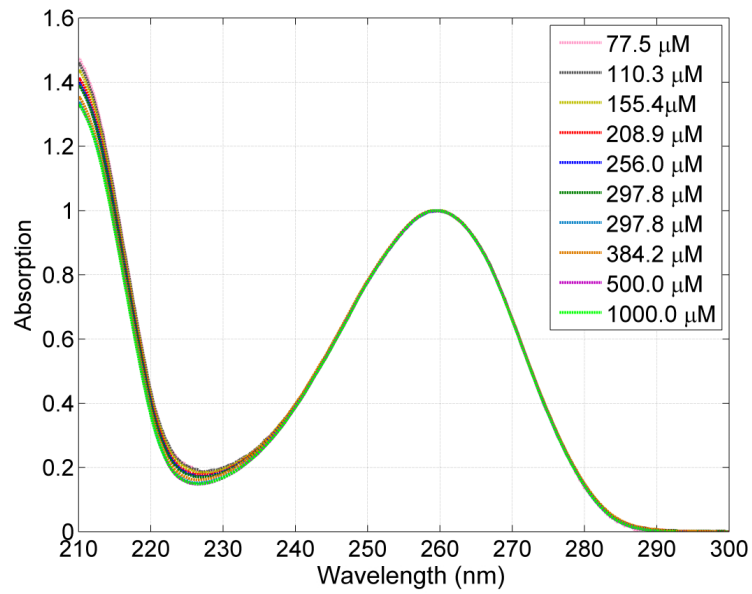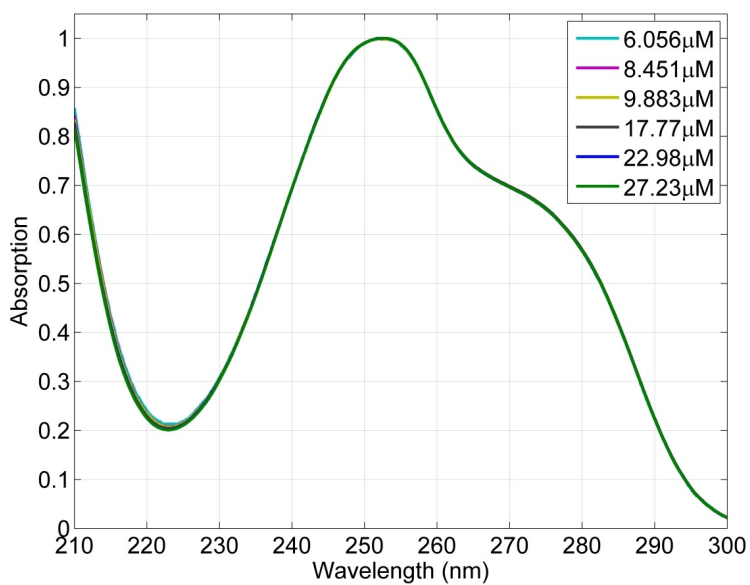
(a) dATP
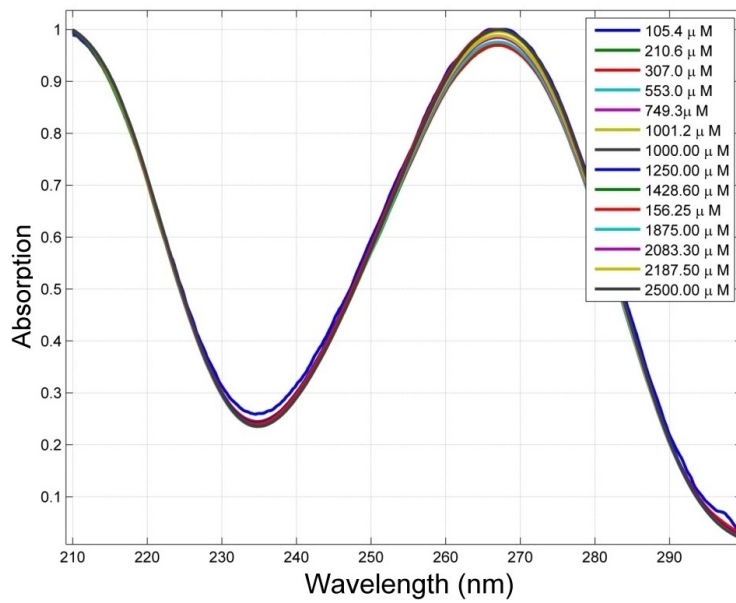
(b) dTTP
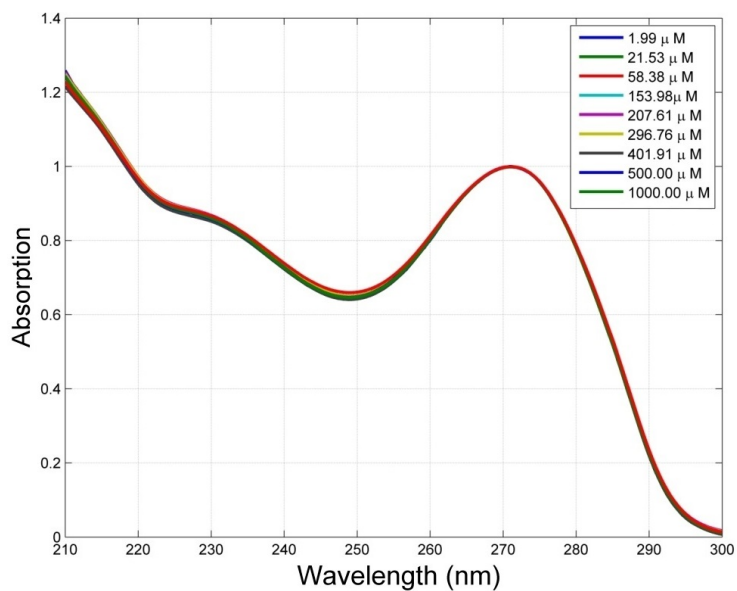
(c) dCTP

(d) dGTP

Figure 2.1: Concentration tests at pH ≈ 7 for the following molecules dissolved in water: 2.2(a) dATP, 2.2(b) dTTP, 2.2(c) dCTP, 2.2(d) dGTP.

The family of nucleobases studied was $dXTP$ where X is for A (adenine), T (thymine), G (guanine) or C (thymine), (Sec. 1.5 for an explanation of their molecular composition). The spectra shown in figure 2.1 present the absorption spectra at different concentrations (concentration tests) performed at pH ≈ 7, for the molecules dissolved in water (ddw). The spectra are normalized to the peak near $260\,\mathrm{nm}$. No significant variation was noticeable in the range of concentrations studied, therefore no dimerization was detected. The small variations visible for dATP, dCTP and dTTP at wavelengths less than $240\,\mathrm{nm}$ are due to scattering from sample powder that was not completely dissolved. In the latter experiments, the samples were sonicated and filtered to remove such artifacts from the spectra.

In conclusion, the solutions with high concentration of nucleobases can be safely used, because the system studied or its properties are unmodified.

2.7 Absorption and circular dichroism of $ssDNA$

This section presents a systematic study of short single strands of DNA, with a sequence-specific nucleobase composition.

Two different types of nucleic acids were employed: homo-oligomers and hetero-oligomers. In the first case, each strand contained a single type of nucleobase, either adenosine or thymidine, and the strand length ranged from 2 to 20 bases. By examining the absorption and circular dichroism spectra of these poly-(dT) and poly-(dA) oligomers, evidence for the existence and the extent of excitons was sought. In the case of hetero-oligomers, nucleic acids with an alternating sequence of adenines and thymines were studied, with a strand length ranging from 2 to 20 bases. The spectra of Figures 2.2, 2.3 and 2.4 show features of excitonic coupling, including absorption hypochromism and butterfly-shaped circular dichroism spectra. Further analysis demonstrated that the extent of this coupling is limited to adjacent nucleobases in the case of adenosine strands, but spans multiple thymidines, at least to their next-nearest neighbors. Following up on this preliminary work, exciton transport and interactions were scrutinized in these DNA strands with time-resolved non-linear optical techniques, such as transient absorption and photon echo two-

dimensional spectroscopy. This preliminary and additional work is vitally important as the link between exciton formation, de-excitation rates, and the mutagenic behavior of DNA needs to be explored and understood fully.

Table 2.2 shows data for $(dA)_n$ and $(dT)_n$, with n from 2 to 20. The molecular weights (MW) and extinction coefficients (ε_{260}) at 260 nm were given by the manufacturer. All other values were extracted from the experimentally-determined absorption and circular dichroism spectra, as explained in Sec. 1.3.

The absorption spectra of the single base deoxy-adenosine triphosphate $(dATP)$ and the $ssDNA$ strands $((dA)_n)$ in Fig. 2.2 show a large band centered near 260 nm, and an intense band near 215 nm, as has been reported in the literature.[15,40,78] The the valley at 230 nm is higher for the $ssDNA$ than expected, as the ratio between its value and the value at the peak near 260 nm should be 0.5[136], but is instead $0.6 - 0.7$. This is possibly due to the presence of impurities (phenolate ion, thiocyanates)[136] from the synthesis process. The absorption peaks of the $(dA)_n$ strands are blue shifted by $3 - 4$ nm compared to the peak of $dATP$. However, this blue shift does not linearly increase with the number of adenosines in the chain. Moreover, there is no broadening of the absorption peaks with increasing adenosine number, although there is a small shape change at ≈ 285 nm. An exciton delocalized between the bases along the strand, and detectable due to the existence of a blue shift, was previously proposed by Hu[105]; nevertheless the shift does not increase as n grows, implying that this delocalization occurs only at a few sites. The lack of broadening is not conclusive as other effects, such as strong coupling to the bath, could cancel out this excitonic effect.

The CD spectra of $(dA)_n$ in Fig. 2.2 have a complicated structure, as has been previously reported by other groups.[82,137–139] Positive bands are present at 271 nm and at 218 nm, whereas negative bands occur at 250 nm and at 207 nm; there are zero crossings at 260 nm and near 215 nm, whereas a positive shoulder appears at 230 nm. Therefore, a clear negative Cotton effect is recognizable, corresponding to the absorption peak at 257 nm. From the perspective of the secondary structure, it has been shown by Brahms et al.[140] that $(dA)_n$ is a "single-chain stacked-base helix", based on their CD spectroscopy data. Likewise, the spectra in this study show a β-helix type due to the broad positive band between 260 nm and 280 nm, preceded by a negative band
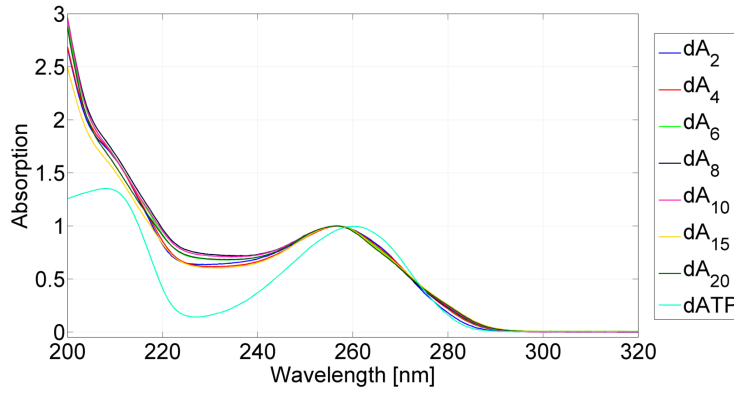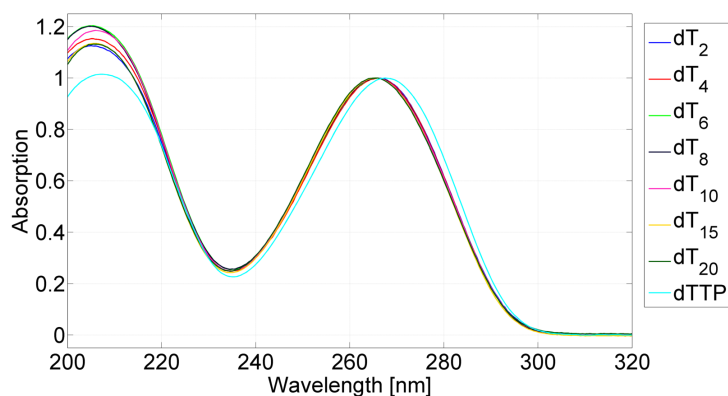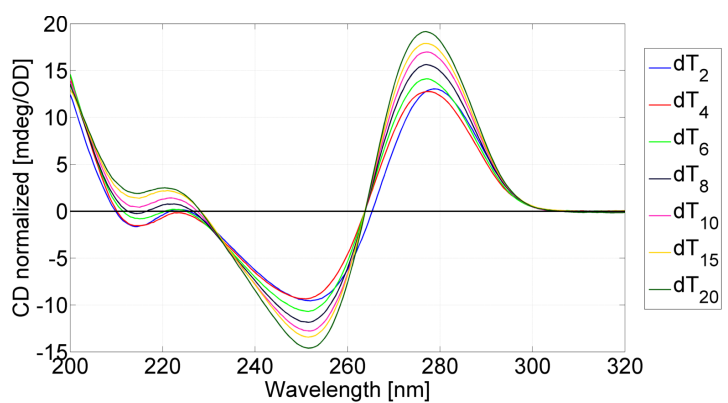
(a)
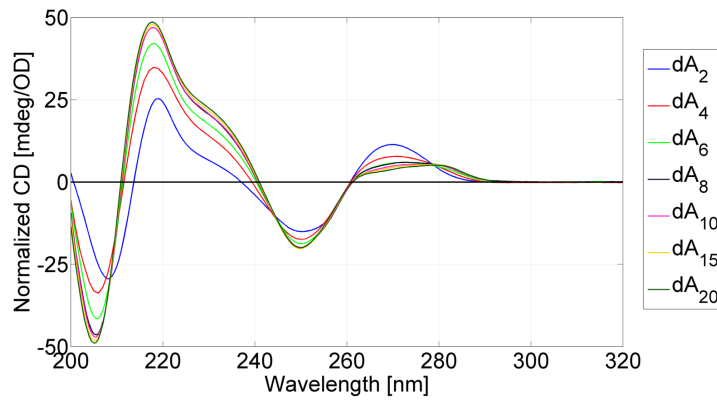
(b)

Figure 2.2: Normalized at the peak near 260 nm absorption (a) and circular dichroism spectra (b) of $(dA)_n$ in 10 mM phosphate buffer, $pH = 7$, where n is the number of adenosines composing the strand. The absorption spectrum of $dATP$ (deoxyadenosine triphosphate) is also included for comparison, while its CD spectrum is omitted because the signal is negligibly small. The scans were performed at room temperature and at neutral pH. The normalization employed is described in Eq. 2.10.
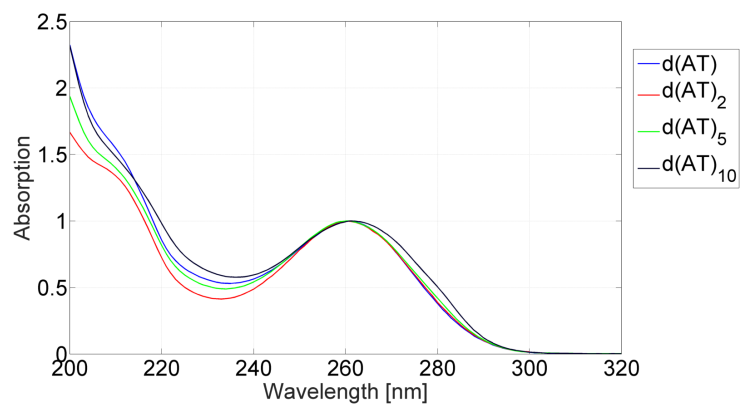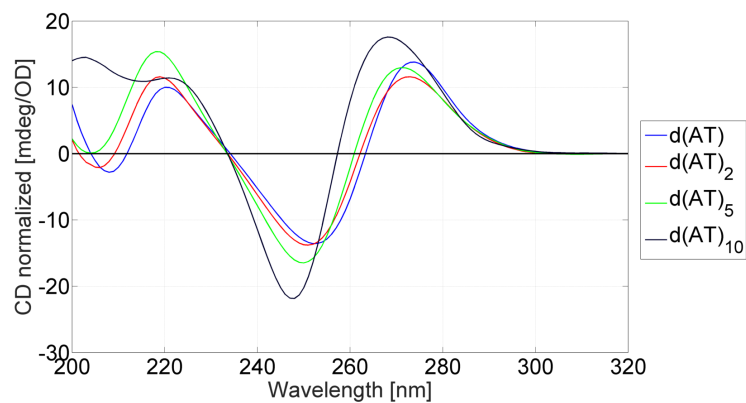
(a)

(b)

Figure 2.3: Peak-normalized absorption (a) and circular dichroism spectra (b) of $(dT)_n$ in $10\,\mathrm{mM}$ phosphate buffer, $pH = 7$, where n is the number of bases composing the strand, from 2 to 20. The absorption spectrum of $dTTP$ (deoxythymidine triphosphate) is included for comparison, while its negligibly-small CD spectrum is omitted. The scans were performed at room temperature and at neutral pH. The normalization employed is described in Eq. 2.10.

(a)

(b)

Figure 2.4: Peak-normalized absorption (a) and circular dichroism spectra (b) of $(dAT)_n$ in $10\,\mathrm{mM}$ phosphate buffer, $pH = 7$, where n is the number of bases composing the strand, from 2 to 20. The scans were performed at room temperature and at neutral pH. The normalization employed is described in Eq. 2.10.

between 240 nm and 260 nm. When normalized CD spectra of different $(dA)_n$ are compared, the magnitude of the maxima at 270 nm and minima at 250 nm increases with chain length (Fig. 2.2).

Experimental absorption spectra of single chains of thymidines in Fig. 2.3(a) are consistent with other studies in the literature.[110] The spectrum of single-base $dTTP$ (deoxythymidine triphosphate) exhibits a large peak centered at 268 nm. Relative to the monomeric absorption peak, the $(dT)_n$ homo-oligomer spectral peaks are blue-shifted to approximately 266 nm, independent of strand length. Another broad absorption band is present at around 206 nm, but is not completely resolved due to the limit of the spectral window, and hence will not be discussed any further. The two aforementioned absorption bands are connected via a deep valley at 235 nm. As was the case for the $(dA)_n$ homo-oligomers, the $(dT)_n$ strands do not show broadening when compared to each other or to the single base $dTTP$. Regardless of the lack of peak broadening, the blue shift for multiple-base $ssDNA$ suggests that there is an exciton delocalized between the bases along the strand, and overall it behaves as a H-aggregate. Due to the constancy of the shift, this may occur only at a few sites, but the broad nature of the absorption peak limits the available information.

The CD spectra are shown in Fig. 2.3(b), and are in agreement with spectra from the literature.[137,139] The complicated structure of the CD spectra for homo-oligomer strands composed of two or more thymidines consists of four peaks of alternating sign. There are two negative peaks at 214 nm and 251 nm and two positive peaks at 223 nm and 278 nm. These are separated by nodal points at 220 nm, 231 nm, and 278 nm. This is interpreted as a combination of two negative Cotton effects above and below 230 nm, corresponding to the absorption peaks centered at 266 nm and 208 nm, respectively. The spectral features show an increase in amplitude only when the number of thymidines in the homo-oligomer strand increases above four. However, there is a 1 nm blue shift of the two red-most peaks between $(dT)_2$ and $(dT)_4$ onwards, and the extremely short strand $(dT)_2$ appears to behave similarly to the short strands ($n = 2, 3$) presented in Holm et al.[137], with respect to this blue shift. The CD spectra indicates a β-helix secondary structure, similarly to $(dA)_n$.[82]

The absorption and circular dichroism spectra of $(dAT)_n$ strands studied in the present work are shown in Fig. 2.4, and are similar to those obtained by other groups[141]. Here one can notice that the

features recall both the spectra of $(dA)_n$ and $(dT)_n$ as expected. The maximum of the main absorption band of $(dAT)_n$ is at $260\,\text{nm}$, with the lone exception of $(dAT)_{10}$ ($261\,\text{nm}$). For comparison, the maximum absorption of $(dA)_n$ is $256.5\,\text{nm}$ and of $(dT)_n$ is $266\,\text{nm}$. The absorption maximum of the A-T repeat strands is located exactly between the constituting homo-oligomers at $261.25 \pm 0.5\,\text{nm}$. Therefore the contribution to the transition dipole strength is distributed equally towards the two nucleobases adenine and thymidine. One would expect similar behavior in the circular dichroism spectra, but the features are more mixed. For example, the positive band at $280\,\text{nm}$ has a completely different shape than the one of $(dA)_n$, while it is analogous to the band of $(dT)_n$. Moreover, the shoulder present at $\approx 230\,\text{nm}$ in $(dA)_n$ spectra is completely absent here and replaced with a (slightly positive) nodal point at $233\,\text{nm}$, a feature present in the spectra of $(dT)_n$ at $231\,\text{nm}$, where the nodal point is slightly negative instead. The difference on the y-scale is due to the influence, although reduced, of the shoulder of $(dA)_n$.

$(dAT)_{10}$ deserves a special comment, since $(dAT)_n$ are self complementary and known to form hairpins at low concentrations of sodium ions[142]. The completely different character of the CD spectrum below $220\,\text{nm}$ of $(dAT)_{10}$ as compared to shorter $(dAT)_n$ strands, is indeed due to some or all of the nucleobases forming parallel hydrogen bonds with the complementary base.[141] Therefore, the tertiary structure of $(dAT)_{10}$ is mostly a hairpin. This occurs with lessened intensity or probability for shorter strands mainly because the length is not sufficient to allow the necessary bending. In fact, the loop of the hairpin is formed of at least five nucleobases. While $(dAT)_5$ is just long enough to create a hairpin, its melting temperature is lower, and hairpins are less likely to exist at room temperature. In fact, using the software UNAfold, the melting temperature of $(dAT)_{10}$ is $69.1°\,C$ (see Fig. A.6 in SI), well above room temperature, while the melting temperature for $(dAT)_5$ is only $30.3°\,C$.

The absorption spectra were fitted with three Gaussians (four in the case of $(dAT)_n$), using the methodology described in the previous section. The fitting reveals two Gaussians underneath the band at $260\,\text{nm}$; both are taken in consideration when calculating the transition dipole strengths. The transition dipole strengths (μ^2, from Table 2.2) were calculated and plotted for the peaks at $257 - 274\,\text{nm}$ and at $235 - 250\,\text{nm}$ as a function of the number of nucleobases present in the
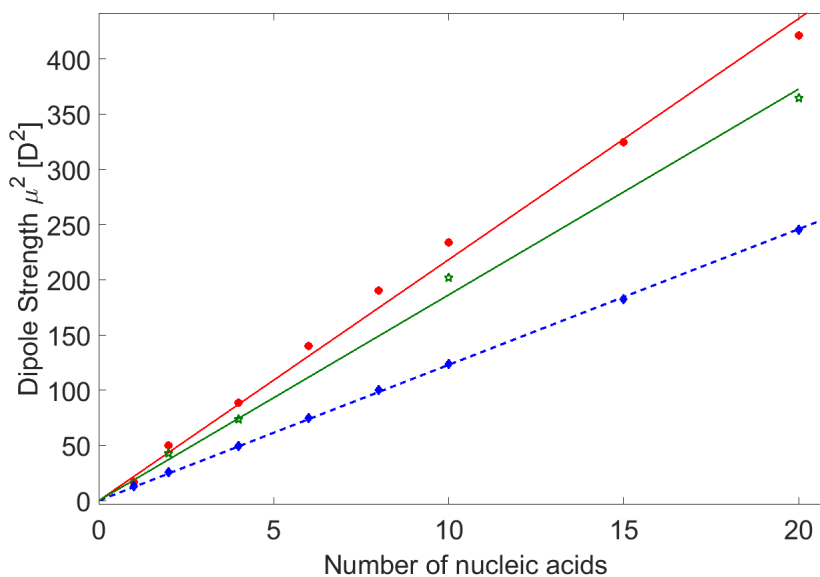
Figure 2.5: Dipole strength of $(dA)_n$ and $(dT)_n$ as a function of the number of nucleobases per $ssDNA$, adenosines in red circles, thymines in blue diamonds and green stars for $(dAT)_n$. The symbols correspond to values extracted from experimental data, given in Table 2.2, whereas the line is a linear fit to the data.

strand of all the studied $ssDNA$. The result is shown in Fig. 2.5. The three interpolating lines are first-order polynomials, with a coefficient of determination (R^2) of 0.9934 $((dA)_n)$, 0.9997 $((dT)_n)$ and 0.9948 $((dAT)_n)$. From these linear fits, one can calculate the dependence of the transition dipole strength on the number of bases. The transition dipole strengths of $(dT)_n$ strands depends on the number of bases in DNA, as $12.3\,\mathtt{D}^2$ per base. This value is less then half than the one obtained for $(dA)_n$, $21.83\,\mathtt{D}^2$, while the transition dipole strength-per-base for $(dAT)_n$ lies between the previous two values: $18.64\,\mathtt{D}^2$. It is clear that the transition dipole strength grows linearly with the number of nucleobases, and one could estimate the value of the transition dipole strength for any given $ssDNA$, by knowing the pattern of the nucleobases in the strand.

The normalized CD spectra carry information on the type of interaction for either the top or the bottom situations in Fig. 2.1. The CD peaks, once the spectra are properly normalized, can be extracted and plotted versus the length of the strand (number of nucleobases composing the DNA), as shown in Figures A.3 for $(dA)_n$ and A.4 for $(dT)_n$. The values of these CD peaks can be treated to extract the
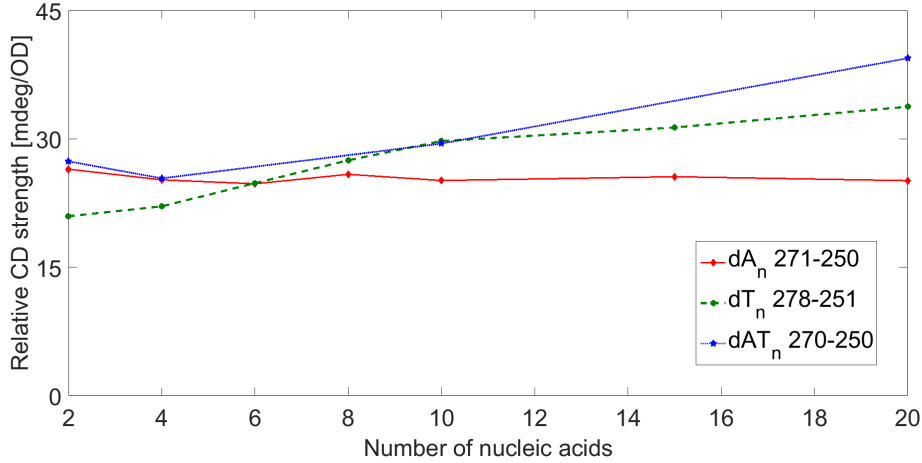
Figure 2.6: Concentration-normalized CD values at the first exciton peak subtracted from those at the second exciton peak as a function of the number of adenosines (full lines) or thymidines (dashed lines) in the single-stranded DNA. The peaks which have been used, are noted in the legend (in $\mathtt{nm}$). The y-axes is also referred in the text as the relative strength of the CD peaks.

exciton interaction strength, where one identifies which peak couples are related. The maxima at $270 - 278\,\mathtt{nm}$ and minima at $250 - 251\,\mathtt{nm}$ in the CD spectra both fall under the same broad absorption peak and arise from an exciton coupling. The difference of the absolute values of the related maxima and minima is shown in Fig. 2.6, plotted versus the number of nucleobases per strand, $(dA)_n$ in red and $(dT)_n$ in blue. While both the CD peaks of adenosine and thymidine strands increase in magnitude when the strands increase in length, the trend is not universal. In the case of adenosine it is constant, while for thymidines the relative CD strength increases with the number of thymidines per strand and does not saturate. It is known that β-DNA has a helicity of 10.5 bases per turn, therefore both the situation where DNA is not fully twisted ($n \leq 10$) and where it is ($n > 10$) were covered. In both ranges the value of the difference between CD peaks is stationary (adenosine) or it increases (thymidine), therefore the trend does not depend on whether the DNA is fully or partially twisted. This suggests that the excitons increasingly delocalize as the $(dT)_n$ becomes longer regardless of the completeness of the helix, as opposite to the excitons in $(dA)_n$ that stay localized in few nucleobases. In other words, for adenosine strands the closest bases are the main contributors to the base-base interaction strength, and the extent of the excitons is among

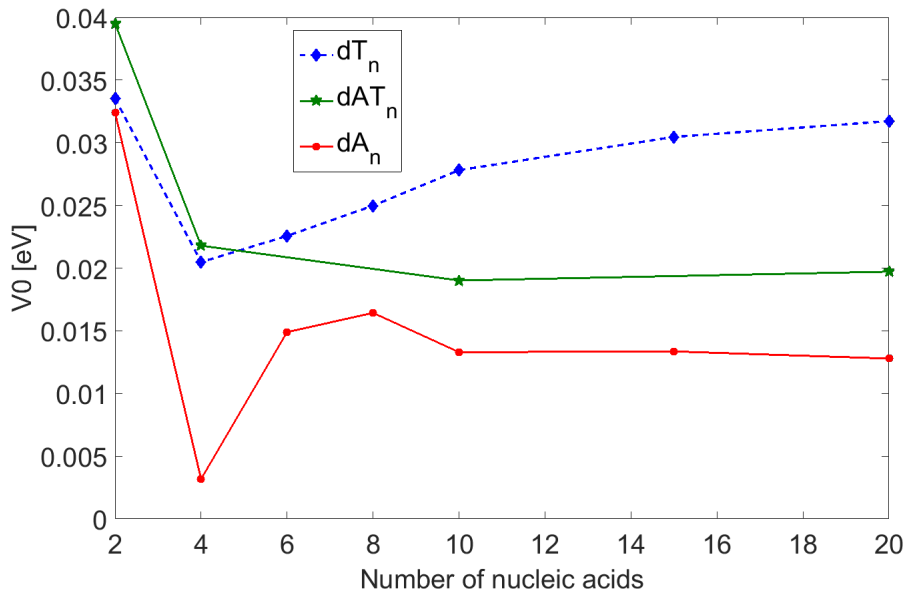merely the nearest adenosines.

Figure 2.7: Exciton coupling calculated through the use of Eq. 2.11 and the experimental absorption and CD spectra of the single-stranded *DNA* of this study. Red circles are reserved for adenosine, blue diamonds for thymidine homo-oligomers and green stars for $(dAT)_n$.

The sum rules for absorption and circular dichroism spectra derived by Burin,[125,143] can be used to express exciton coupling strength through the integral properties of the experimental spectra 2.11. The sum rules have been applied to the spectra of this study, and the resulting values are plotted in Fig. 2.7. The calculated values in Fig. 2.7 match well the values of excitonic coupling reported by Blancafort et al[101] (Table III). Moreover, the values of the exciton coupling are similar to the values found for DNA hairpins by Burin. Considering that hairpins are double-stranded, the lower values of exciton coupling that are found are to be expected. In fact, the values Burin finds for A-poly-T sequences (0.035 eV, 0.036 eV, 0.033 eV for $n = 4, 6, 8$) are 4% smaller for $n = 6$ and 20% smaller for $n = 8$ than the values in this study. This is not surprising, considering that a double-stranded structure is more rigid than a single-stranded one, and its nucleobases are closer, therefore the electronic excitations are farther apart due to the stronger H- and J-shifts. The growing trend of thymine oligomers and the steady trend of adenine oligomers confirms the analysis (Fig. 2.6); the exceptions are strands of 2 and 4 nucleic acids. This might be due to an underestimated difference in the Van Vleck theory be-

tween strands too short to complete even half of a chain twist (5 nucleic acids in B-type DNA). Using Burin's method, the $(dAT)_n$ family holds steady, whereas using the method here it grows; as previously mentioned, $(dAT)_n$ is a self-annealing repeat that has high chance to become double stranded when long enough, while it stays un-folded when short. Consequently, the exciton couplings for shorter and longer A-T values represent two different structures (single and hairpin double stranded DNA).

A surprising difference exists between the results of Fig. 2.6 and Fig. 2.7 on the one hand, and Fig. 2.5 on the other, where the order of the three families is inverted. For example, the values of the dipole strength of adenine homo-oligomers are the highest at any given number of nucleic acids, while the value of the exciton coupling is the lowest. Due to the dipolar nature of exciton coupling, the oscillation strength is greater for quantum states with larger transition dipole moments.[143] Therefore, the exciton coupling should scale with the dipole strength. Consequently, the aforementioned difference might be simply due to a different geometry of the DNA, meaning that the nucleobases are not disposed in a parallel fashion or with a 36° angle between the nearby bases, as originally hypothesized.
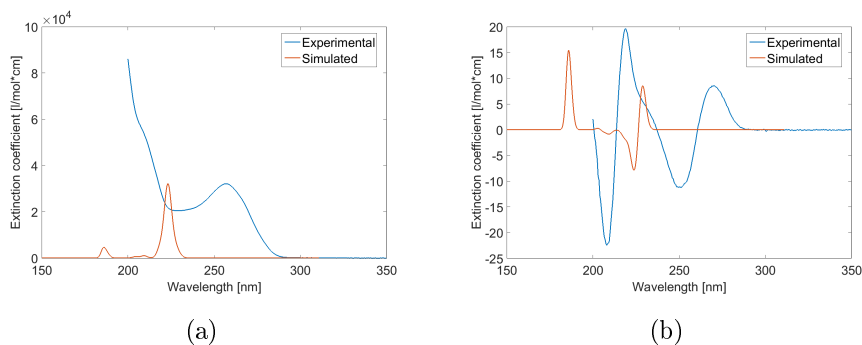

(a)   (b)

Figure 2.8: Absorption(a) and circular dichroism spectra (b) of $(dA)_2$, comparison between experimental (blue dashed line) and simulated (red full line) spectra.

To further investigate such hypotheses, some simulations were performed using the software package Gaussian 09, with a fixed B-type structure geometry for the strands. The simulated circular dichroism spectra of adenine homo-oligomers (Fig. 2.8(b)) match qualitatively the experimental spectra, if one accounts for a shift of $34\,\mathrm{nm}$ between the experimental and simulated spectra, caused by an insufficiently

refined computational method. The CD spectra of thymidine homo-oligomers (Fig. 2.9(b)), when a shift between experimental and simulated spectra of $37\,\mathrm{nm}$ is included, show transitions with the opposite sign when compared to the experimental spectra, suggesting that in the experiments, the angles between two neighboring thymidines in the strand are not close to the theoretical value of $36°$. This holds for the $(dAT)_n$ family as well (Fig. 2.10(b)), where a shift of $33\,\mathrm{nm}$ between the experimental and simulated spectra is seen. Given the approximate nature of the spectral simulations, which were performed on a reduced model of B-*DNA* (nucleobases-only, to diminish the computational time), and then only at a single, highly idealized geometry, better agreement with experiment can not be expected. Simulations of CD spectra with different geometry, and including solvation effects are planned.
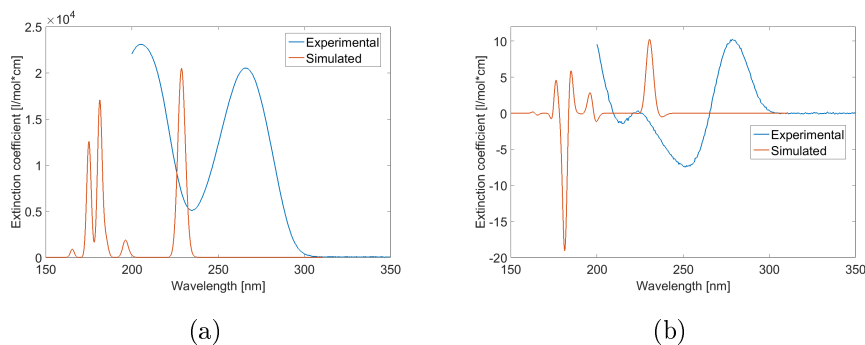

(a)   (b)

Figure 2.9: Absorption(a) and circular dichroism spectra (b) of $(dT)_2$, comparison between experimental (blue dashed line) and simulated (red full line) spectra.

2.8 Conclusions

This chapter starts with the description of the protocol for the buffers of all samples used in the present dissertation. The majority of this chapter is on sample selection and characterization, which is based on the physical and chemical properties of the samples, especially the possibility of dimerization of nucleobases (*dATP*, *dTTP*, *dCTP*, *dGTP*). Through their absorption spectra in solution at different concentrations and pH, it was demonstrated that no visible dimerization occurs. On the contrary, dimerization does occur when the nucleobases are linked by a phosphate backbone, as in the case of single-stranded
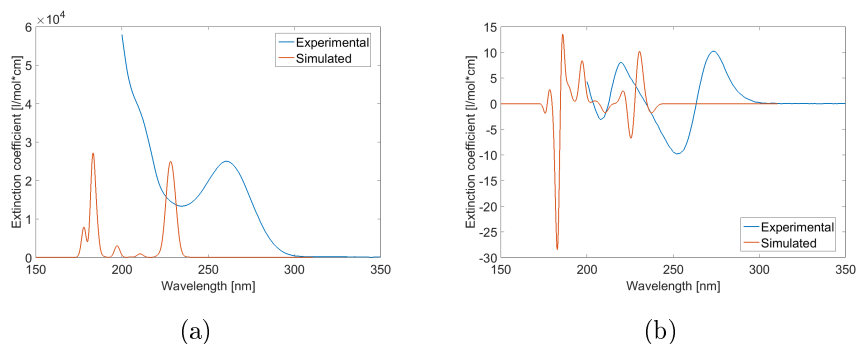
Figure 2.10: Absorption(a) and circular dichroism spectra (b) of (dAT), comparison between experimental (blue dashed line) and simulated (red full line) spectra.

DNAs, also referred to as oligomers; from a spectroscopic perspective, an exciton is created upon electronic excitation. Oligomers display a small wavelength shift of the absorption peak. Furthermore, circular dichroism spectroscopy shows an evident Cotton effect in the spectra of the studied oligomers, though the expected narrowing of the absorption peaks is absent due to strong solvent interaction.

The Gaussian decomposition of the absorption peaks reveals a linear relationship between the number of nucleobases present in the single-stranded DNA and dipole strengths. This allows for the prediction of the transition dipole strength values of strands with different numbers of bases. Further analysis of absorption and CD spectra by a clever normalization (see methods section) uncovers a non-trivial dependence of the delocalization extent of excitons on the length of the oligomeric chain. It was experimentally proven that excitons delocalize only amongst nearest neighbors in adenosine oligomers, while thymidine and $(dAT)_n$ oligomers have excitons that delocalize over a growing range of neighbors as strand length increases.

Furthermore, in order to test the findings the method described by Burin et al.[125] was applied. While the results qualitatively agree with the samples in the study, there are two exceptions. First, all three families present with outliers in the samples with two and four nucleobases, while this is not observed when using the normalization procedure used in this study. Second, the order of the strength of the excitonic coupling calculated using Burin's method and the method in this study is reversed in this study as compared to the dipole strength order. Currently, the origin of these differences is not fully understood;

it may be due to a non-canonical disposition of the nucleobases within the strands, as supported by the simulated CD spectra.

In conclusion, by employing linear spectroscopic methods, evident excitonic behavior in single-stranded *DNA*s was demonstrated. The details and the strength of such behavior strongly depend on the composition of the strands, specifically on the nucleobases bordering any other given nucleobase.

Chapter 3

Closed-loop pump-driven wire-guided flow jet

The content of this chapter is partly reproduced from the paper *A. Picchiotti et al., Rev. Sci. Instrum., 2015, 86, 093105* [18].

3.1 Introduction

Ultrafast spectroscopic techniques are rapidly developing to cover the ultraviolet spectral range, where the light scattering and stretching of ultrashort pulses in the sample holder window material become serious and often create overwhelming problems. For example, after passing through a 1-mm thick UV-grade fused silica substrate, an $8\,\mathrm{fs}$ laser pulse centered at $275\,\mathrm{nm}$ will be stretched up to $\sim 170\,\mathrm{fs}$. Additionally, in ultrafast experiments with high-repetition laser pulses, the need to constantly replenish the sample in order to avoid the accumulation of photochemical products and associated artifacts. For this reason, flow-cuvette systems were developed and are commercially available. However, in some circumstances, additional problems arise and these systems are not adequate. In particular, light scattering grows nonlinearly with decreasing wavelengths, which in turn dramatically increases the back-ground and decreases the signal-to-noise ratio (SNR).

In ultrafast experiments, such as transient absorption and two-dimensional photon-echo based spectroscopies performed in the deep UV ($200-300\,\mathrm{nm}$), the fact that the non-linear signals are very small, and light scattering becomes the major limitation in the application of flow cells with windows must be taken into account (see, e.g., discus-

sion in Tsent et al.[34]). All transparent materials are subject to scattering in the UV: any type of glass or crystal windows and the solvents themselves (the Rayleigh scattering grows as $1/\lambda^4$). This scattering affects the SNR significantly, especially in experiments performed in the UV. Therefore, avoiding windows and reducing the path length in order to decrease the solvent scattering and its non-linear contribution to the signal are attractive solutions.

A wire-guided flow jet (WGJ) system can overcome the limitations aforementioned. It should be stable enough, in terms of both short- and long-term stability, for performing experiments with femtosecond UV-pulses, and have a flow speed which is high enough for a complete sample exchange in the interaction volume between laser pulses to avoid artifacts from accumulated laser-induced photochemistry.

For this study and beyond, a wire-guided closed-loop pump-driven flow jet system was developed that delivers high SNR values in the deep UV with both high short- and long-term stability. Similar WGJ-systems have been previously reported[144,145] but the present design significantly improves the simplicity, performance, stability, and most importantly, greatly reduces the needed volume for stable operation. This later feature is particularly important for the study of precious biological samples. Moreover, the WGJ system in this study is compact ($7 \times 20\,\mathrm{cm}$ foot-print), and thus can be readily implemented into a typical pump-probe or 2D-setup with focusing optics with focal lengths in the $100 - 150\,\mathrm{mm}$ range.

Besides the design details provided in Section 3.2, this chapter reports the results of the full characterization of the WGJ system with respect to flow and optical stabilities, which are important factors for long-term measurements with high SNR.

3.2   Design of the wire-guided jet system

The *WGJ* allows for the creation and continuous maintenance of a stable liquid film between two wires. It includes a microfluidic pump, a collector, a sandwich block which holds the wires, a damping syringe, and connecting tubes (Fig. 3.1). The active parts of the *WGJ* (block with wires and collector) are mounted into an L-shaped bracket attached to a XYZ manual translation stage (Newport, model 9062), which positions the jet with respect to the laser beam and the beam focal plane with $10\,\mu$m precision; see Fig. 3.2 for a rendered 3D image of the whole *WGJ* system.
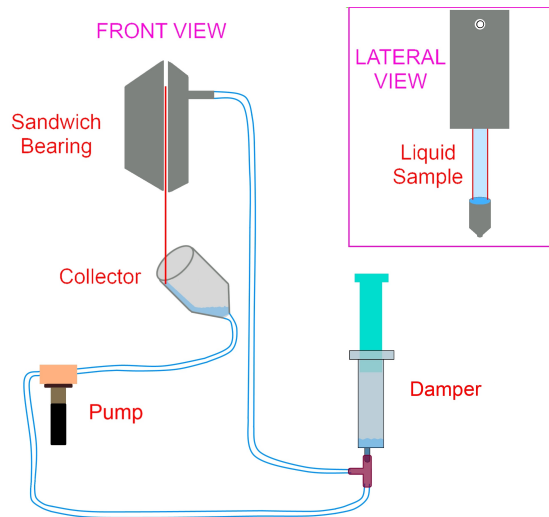
Figure 3.1: Schematic of the *WGJ* system (description of parts see in text).

The sandwich block is home-built, based on an initial design by the H.F. Kauffmann group (University of Vienna, Austria) which was modified to improve its performance. For a secure holding and to ensure reproducibility of the positioning of the wire, a $0.2\,$mm deep channel was milled into the sandwich block. The internal channel is symmetrically present on both sides of the sandwich block. It has an important role in preventing lateral leaks and in the creation of a high quality liquid film at the immediate exit from the block, the surface is smooth and without ripples. The width of the channel defines the spacing between the wires. In the optimized design, with wires of $0.5\,$mm in diameter, the channel width is $3.5\,$mm. The blocks are made from stainless steel (AISI 316-L), as are all other metal parts exposed to liquid. Two stainless steel wires (same type as the steel of the block)
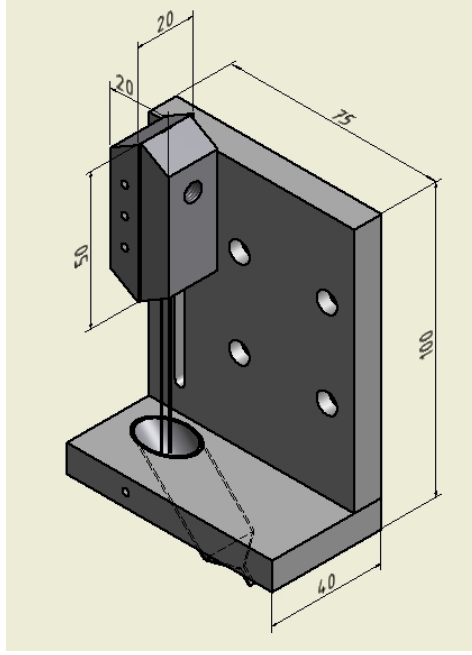
Figure 3.2: Rendered 3D image of the whole *WGJ* system.

guide the liquid between them. The wires are manually bent to a *U*-shape and have a length of 90 mm. They have a distance (as internal width between them) of 2.5 mm. In general, the length can vary up to 5% but the width is fixed by the presence of the internal channel that maintains parallelicity. These dimensions were found to lead to the best liquid film stability for solutions with a wide range of viscosities, ranging from ethanol to water-based buffer.

The wires were purchased from Advent Research Materials Ltd (UK). It should be noted that they are provided straight by the manufacturer with good precision so that no additional straightening is required. The straightening of coiled wires is possible but introduces non-uniform stress to the material and therefore some sections of the wire will have a smaller diameter than others, introducing unpredictable fluid dynamical effects into the liquid layer and thus non uniform thickness. The ends of the wires are immersed into a home-built collector, which is tilted by 45° with respect to the wires (see Fig. 3.1 and Fig. 3.3), and with the tips of the wires very close to, but not in direct contact with, the internal wall of the collector. This design allows the creation of a smooth curtain flow, and prevents standing waves (ripples) forming at the end of the jet due to contact with the liquid surface in the collector, that might affect the stability of the liquid film (especially its thickness in time). Any variations of the liquid

height in the collector will not affect standing waves on the jet surface; this secures a smooth, stationary and continuous flow of liquid in the *WGJ*, even when evaporation causes the level of the liquid to drop inside the collector. The optical quality of the liquid film between the wires can be visually inspected in Fig. 3.3.
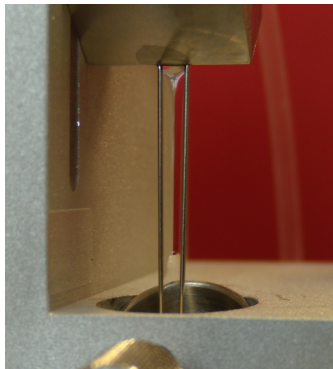

Figure 3.3: View of the flowing liquid between the wires. Due to the lens effect on the liquid film the wires do not appear parallel, but they are. The collector is tilted by 45° with respect to the wires.

The outlet of the collector is directly connected to the inlet of a microfluidic pump by a plastic tube, whereas the inlet of the sandwich block is connected to the outlet of the pump via a damper (a plastic syringe), and a plastic T-bridge (see in Fig. 3.1).

This damper has two functions: first, it serves to fill the *WGJ* system with the liquid sample and allows precise control of the amount of sample (and its height) in the collector. Second, it attenuates the pulsations in the flowing liquid caused by the pump. The microfluidic pump implemented in the *WGJ* system is a gear-type pump from Mikrosysteme GmbH (Germany).[29] The controller mzr-S06 powers the pump motor and controls its rotation speed with good precision and reproducibility (Sec. 3.3.2). Two different pump models were employed, the sole difference being the materials of the internal gears: for solvent compatibility reasons mzr-2942cp is used for pumping of biological samples in water-based solutions, and mzr-2921 for organic dyes dissolved in alcohols.

Tubing from chemically resistant tygon (B-44-4X and 2075, purchased from Riesbeck GmbH, Germany) was used for biological samples, with an inner diameter of $1/16'' \approx 1.6\,\text{mm}$, and for the alcohol-based solutions PTFE tubing with an inner diameter of $1/16'' \approx 1.6\,\text{mm}$ was used (type BOLA-Tubing, purchased from Bohlender GmbH, Ger-

many).

3.2.1 Estimate of Volume

The minimization of volume is an important factor in building a *WGJ* due to the costs of samples, especially biological. In the following section, an estimate of the total volume circulating in the system is provided. The tubing used is approximately 56 mm long and its diameter is 1.60 mm, therefore the volume of liquid contained in the tubes alone is ≈ 0.6 ml. The volume in the collector is approximately 0.67 ml; this value is overestimated, because of the triangular shape of the collector (see Fig. 3.4). The liquid contained in the collector is estimated by halving the volume, due to its inclination of 45°, of a cylinder with a diameter of 13 mm and a height of 5 mm. Inside the damper there can be as little as 0.5 ml, but best results are obtained when there is 1.5 to 2 ml. The dead volume in the pump itself is 69 µl = 0.069 ml.[29] The sum gives a total volume of ≈ 3.5 ml, which can become ≈ 2 ml by reducing the liquid in the collector, or modifying its shape. Such a new modification has been made but not yet tested.
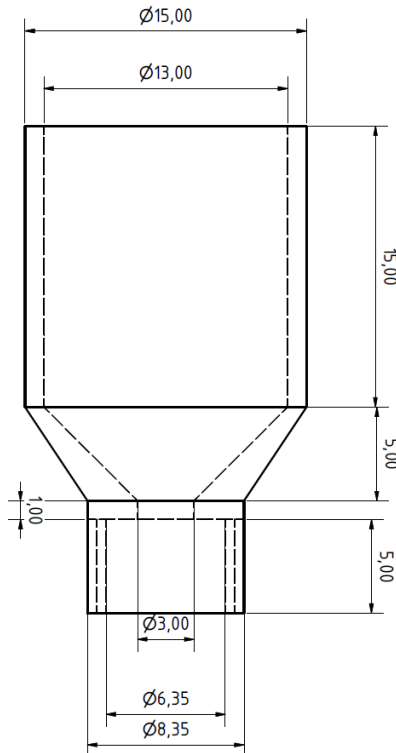

Figure 3.4: Technical drawing of the collector, with the real dimensions given in millimeters.

The volume of the liquid film itself is more complicated to calculate. Approximating the shape of the film to a parallelepiped of 0.5 mm thickness, 3.5 mm width and 90 mm height, an upper volume of 0.157 ml is obtained. This value is overestimated due to the crude approximation of the profile of the liquid. With a better approximation, the profile of the film displays some nonlinear behavior, as shown in Fig. 3.5; the blue area can be estimated to be slightly more than half of the inscribing parallelepiped, therefore the minimum volume of the film between the wires is 0.078 ml. By using instead a catenary approximation, the blue area in Fig. 3.5 is 23.21 mm^2 and the volume is ≈ 0.09 ml. Nevertheless, the total volume of liquid contained in the jet does not exceed 3.66 ml.

Achieving smaller volumes is possible with thinner tubings. The tubing currently used in the system has an internal diameter of 1/16″ (≈ 1.6 mm), while tubing with an internal diameter as small as 0.5 mm is commercially available and can be used. In this case, using 40 cm of total tubing, the minimum operational volume is 847 μl. In particular, there is a total volume of 500 μl of liquid in the dumping syringe and 200 μl in the collector as the liquid has to cover the outlet to avoid air bubbles inside the system, moreover the tubes contain 78 μl and there is 69 μl volume in the pump itself.

Minimizing the "dead" volume to sub-1 ml is theoretically possible. However, evaporation of liquid will restrict the operational time significantly, and the pressure inside the tubes will be significantly higher than in the current system; this may introduce unpredictable fluid dynamical behaviors that could impair the stability of the liquid film.
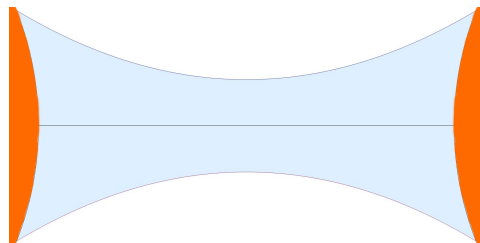

Figure 3.5: Estimated horizontal profile of the liquid film between the wires (depicted in orange), using a catenary function.

3.3 Characterization of the *WGJ* system

3.3.1 Flow rate

The *WGJ* system can be adjusted to a variety of specific needs. In particular, the volumetric flow of the jet can be controlled by setting the number of revolutions per minute (RPM) of the pump motor through the controller, and can also be externally set from a computer using corresponding software provided by the company. The error of the rpm-values is estimated to be ± 30 RPM, see Section 3.3.2.

The flow rate was measured by using a known volume of liquid passing through an empty system. The time was taken with a stopwatch. This procedure was repeated five to ten times with different volumes and at different pump speeds. Fig. 3.6 presents the determined relationship between RPM and flow.
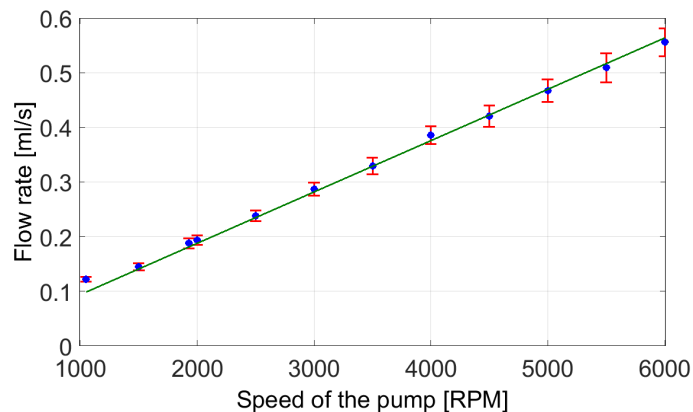

Figure 3.6: Flow rate of the *WGJ* as a function of the speed of the pump. Dots and error bars: experimental data, line: linear fit.

From the linear fit (the green line in Fig. 3.6) with a correlation of 0.98, the flow rate can be linked to RPM with a proportionality coefficient of $9.4 \cdot 10^{(-5)}$ [ml/s]/RPM.

However, for ultrafast experiments with high repetition rate laser pulses, it is more important to know the speed of the sample exchange at the excitation spot. This estimation requires, aside from the flow rate and the spacing between the wires, the film thickness in the working area.

3.3.2 Error of the speed of the Mikrosysteme pump

The pump employed in the system is a micro annular gear pump. It contains two rotors rolling inside one another, as shown in Fig. 3.7. The rotors are eccentrically displaced with respect to each another, thus creating non-circular motion. The indenting is cycloid so as to always keep the rotors interlocked. Pumping occurs as the rotation increases the suction side and decreases the delivery side of the pump, eventually generating a flow between the inlet and the outlet.
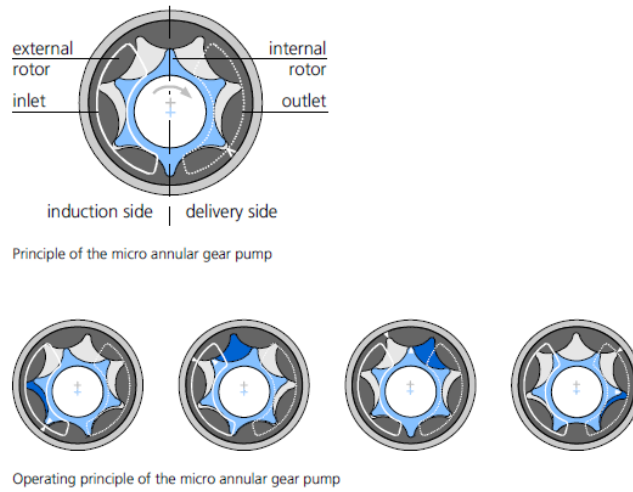
Figure 3.7: Cartoon of pump internal motor, from the manufacturer's manual.[29]

Set Velocity [$rounds/min$]	Min deviation [$rounds/min$]	Max deviation [$rounds/min$]
1000	-18	25
1500	-17	24
2000	-24	25
2500	-23	26
3000	-22	26
3500	-23	25
4000	-21	32
4500	-25	32
5000	-29	22

Table 3.1: Minimum (Min) and maximum (Max) deviation values from the velocity of the rotor gear set on the potentiometer.

Due to the technical characteristics of the pump, in particular its head gear, the speed of the rotor is not stable in time with sufficient

accuracy for the purposes of this study, because this instability transfers to a thickness fluctuation. Therefore, setting a specific speed on the control module does not ensure a stable *actual velocity* of the rotor itself. It is possible to estimate the error on the actual velocity by measuring the divergence of the pump velocity using the software available from Mikrosysteme GmbH. An example of collected data is shown in Table 3.1; data were collected by operating the system filled with distilled water (ddw) and connecting the pump to a computer through the control module. Each point on the plot in Figure 3.8 and Table 3.1 is the maximum/minimum deviation of a statistically relevant number of data at least 60 data points for each set velocity, as it is shown in Fig. A.0, in appendix A.
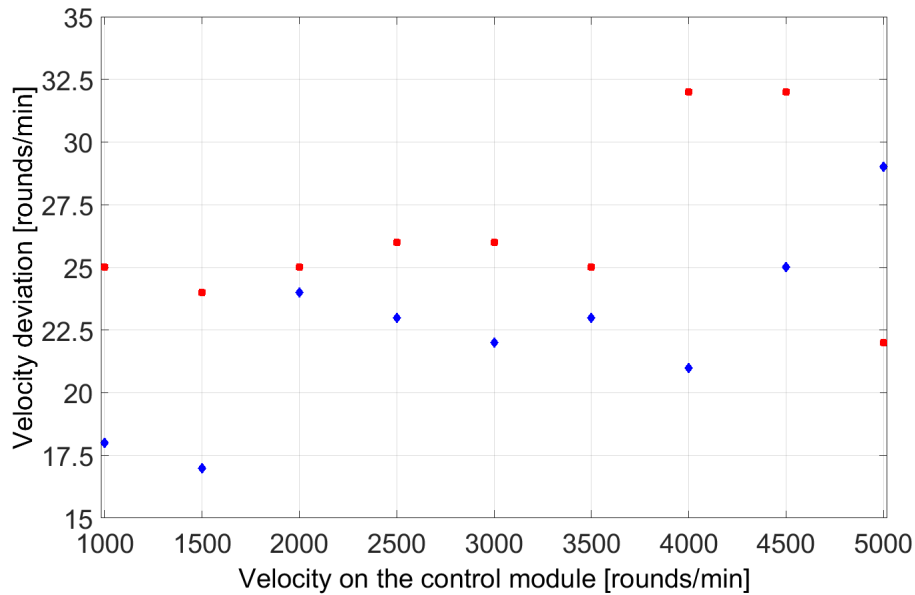

Figure 3.8: Minimum (blue) and maximum (red) deviation values from the velocity of the rotor gear set on the potentiometer

From the graph in Fig.3.8 one can infer that the deviations from the actual velocity of the rotor vary between $17\,\mathtt{rounds/min}$ and $32\,\mathtt{rounds/min}$. Consequently it is safe to assume that the error of the speed of the pump is $\pm 30\,\mathtt{rounds/min}$; this has to be taken in account to determine the flux of the liquid and its fluctuations.

3.3.3 Characterization of the film thickness

Characterization of the film thickness and its stability is done by operating the *WGJ* system filled with an aqueous solution of an organic

61

dye and measuring transmission using a He-Ne laser and a photodiode (PD) connected to an oscilloscope. A schematic of this measurement is depicted in Figure 3.9(a). Rhodamine 6G (Rh6G, purchased from Radiant Dyes Laser GmbH, Germany) was used, because it has an absorbance peak close to that of the He-Ne laser $(543\,\mathrm{nm})^{146}$, and is water-soluble. At this wavelength the extinction coefficient of Rh6G is approximately $10.5 \cdot 10^4\ \mathrm{M^{-1}cm^{-1}}$ [102] so that only a small amount of dye is needed to achieve solutions with high OD. More information on the optical properties of water-based solutions of Rh6G can be found in Subsection 1.6. Concentrations of Rh6G and absorption spectra of solutions were checked using a commercial spectrophotometer (Shimadzu UV-2600, Japan) using a quartz cuvette (Hellma GmbH, Germany) with path length $l = 1\,\mathrm{mm}$. Measuring the optical density OD_0 (at $543\,\mathrm{nm}$) required the prepared solution to be diluted five times in order to be used in the 1 mm cuvette, in order to have a comparable optical density to the jet.
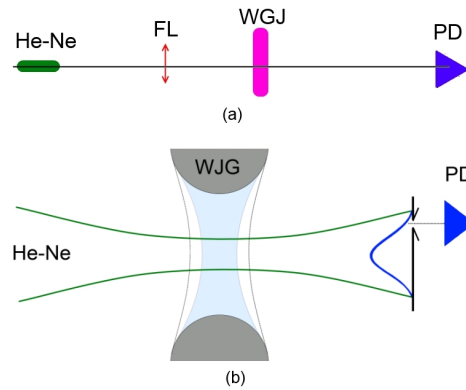

Figure 3.9: (a): Schematic of the optical system used for measurement and test of thickness stability in the *WGJ*. He-Ne – laser, FL - focusing lens, PD - photodiode connected to the oscilloscope, and *WGJ* is the jet. (b): Top view of schematic diagram for measurement of the optical stability. The photodiode collects the light at the edge of the beam where instabilities are maximal. The light, depicted as two green convex lines, passes through the jet film (light blue) whose thickness varies up to the gray dotted lines. The dark gray semi-circles represent the stainless steel looped wire sides.

The laser beam was focused with a 150-mm focal length lens to achieve a small spot size on the jet. The laser power was measured without liquid and with the jet running, using a photodiode PD (New-

62

port, USA) with a set of attenuating filters (Thorlabs, USA); the signals were collected using a digital oscilloscope (Tektronix 24658, USA). The transmission of sample was calculated as $T = I/I_0$ (without accounting for reflections from the jet surfaces). Here I_0 is the mean value of the PD-signal without sample (jet is stopped), and I - the mean value of PD-signal with sample (jet is running). The thickness d of the sample film can be thus calculated from the cuvette's path length l, as:

$$d = l\frac{10^{-T}}{OD_0} \qquad (3.1)$$

Neglecting the reflections leads to up to 2% inaccuracy in estimating the thickness. Variations in the jet film thickness were estimated by the deviations in the PD-signal measured after the jet (ΔI). The experimental data collected in Table 3.2 is a representative set of the results from one of the measurements. This table also gives calculated flow rates at a given RPM (see previous sub-section), the thickness deviation Δd in absolute units and normalized to the values of the layer thickness (RTD).

S.P. [rpm]	Q [ml/s]	d [μm]	Δd [μm]	RTD [%]
1200	0.11	99	7	1.06
1300	0.12	95	7	0.94
1400	0.13	113	9	0.94
1500	0.14	123	10	0.80
1600	0.15	146	5	0.89
1700	0.16	169	6	0.88
1800	0.17	184	7	1.23
1900	0.18	227	13	1.40
2000	0.19	214	10	1.18
2500	0.23	284	11	1.94
3000	0.28	368	15	3.68

Table 3.2: Experimental results of the thickness measurements. S.P. is the rotational speed of pump, Q is the flow rate, d and Δd is the thickness and its absolute deviation, and RTD is the relative thickness deviation.

Figure 3.10 shows the measured film thickness as a function of flow rate. It can be well fitted to a second-order polynomial with goodness

of fit 0.95 (presented in the figure as a green solid line):

$$d = 645Q^2 + 313Q. \qquad (3.2)$$

As can be seen from Fig. 3.10, the thickness is nearly linearly proportional to the flow rate; deviations from the linear dependence are due to non-linear change in the meniscus geometry of the jet. Jet thickness was measured at different vertical positions of the laser beam spot and found to vary insignificantly within 1 to 1.5 cm. It can also be seen in the photograph (Fig. 3.3) that the jet surface has excellent flatness in the vertical direction.
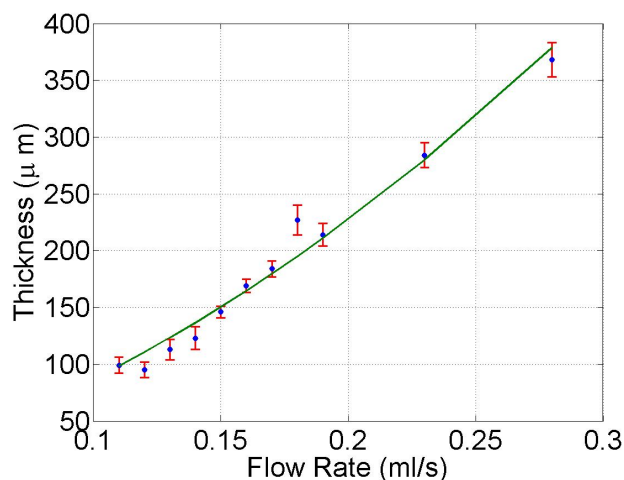
Figure 3.10: Thickness of the water layer in the jet as a function of the flow rate. Dots: experimental points, line: fit from Eq. 3.2.

The relative thickness deviation $RTD = \Delta d/d$ vs. flow rate is plotted in Fig. 3.11. At the highest flow rates the thickness variations values never exceed 4%. This dependence shows a clear minimum (approximately at 0.15 ml/s flow rate) which corresponds to the maximal stability of the jet thickness (0.8% at 0.76 ml/s flow rate).

The jet becomes unstable at low flow rates due to instability in the pump itself, and at high rates due to strong pulsations of the pumped liquid, as expected also caused by the pump. It must also be noted that the region of good stability has a plateau between 0.12−0.17 ml/s flow rates. In ultrafast spectroscopy experiments, this range of flow rates is used to ensure sample exchange between laser shots. More specifically, it is possible to calculate the flow speed and to estimate the sample exchange rate. For $Q = 0.28$ ml/s (the highest measured flow rate) the water jet thickness corresponds to 0.37 mm (see in Table 3.2), and

taking into account inner spacing between wires (2.5 mm), we obtain a flow speed 300 mm/s, without accounting for the meniscus influence on the geometry of the jet cross-section. The stable regime corresponds to a flow rate of $Q = 0.15$ ml/s; however, due to significant lowering of the jet thickness to 0.14 mm (Table 3.2) the actual flow speed becomes higher: ~ 430 mm/s. For a laser spot of 0.1 mm in diameter, this gives a sample exchange rate of 4.2 kHz. In the experiments in this study, a 1 kHz laser is used, and the spot diameter is approximately $60 - 70$ μm so that this flow rate is sufficient to ensure adequate sample exchange between laser shots.
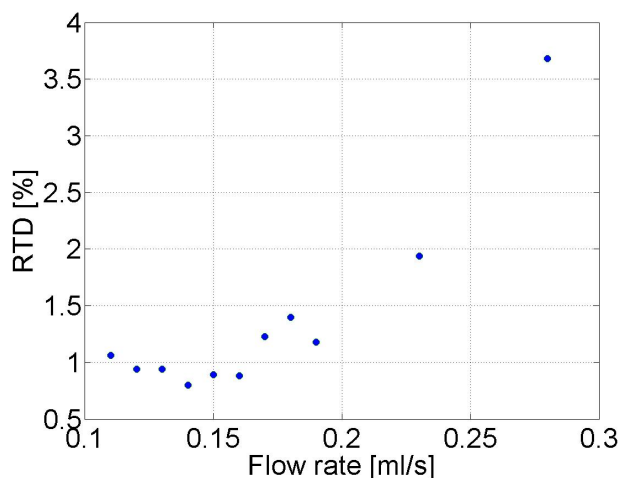
Figure 3.11: Relative thickness instability RTD as a function of the flow rate Q of the jet.

3.3.4   Optical stability

Due to the capillary effect, the profile of the liquid flowing between the wires corresponds to a negative lens, as is schematically shown in Fig. 3.9(b). The optical strength (i.e. focal length) of the formed lens and the position of its optical axis depend on the flow speed and its fluctuation. An example of the effect of the lens from the film is shown in Fig. 3.12, where the WGJ was filled with an absorbing dye dissolved in ethanol and the speed of the pump was varied. The height and horizontal position of the beam with respect to the wires was chosen to maximize the transmitted signal at the beginning of the experiment and subsequently never changed.

The flow itself is stable, even for long periods, if not mechanically perturbed. This condition was tested in the setup for more than ten

(a) 750 revolutions/min (b) 1000 revolutions/min (c) 1250 revolutions/min

(d) 1500 revolutions/min (e) 1750 revolutions/min (f) 2000 revolutions/min

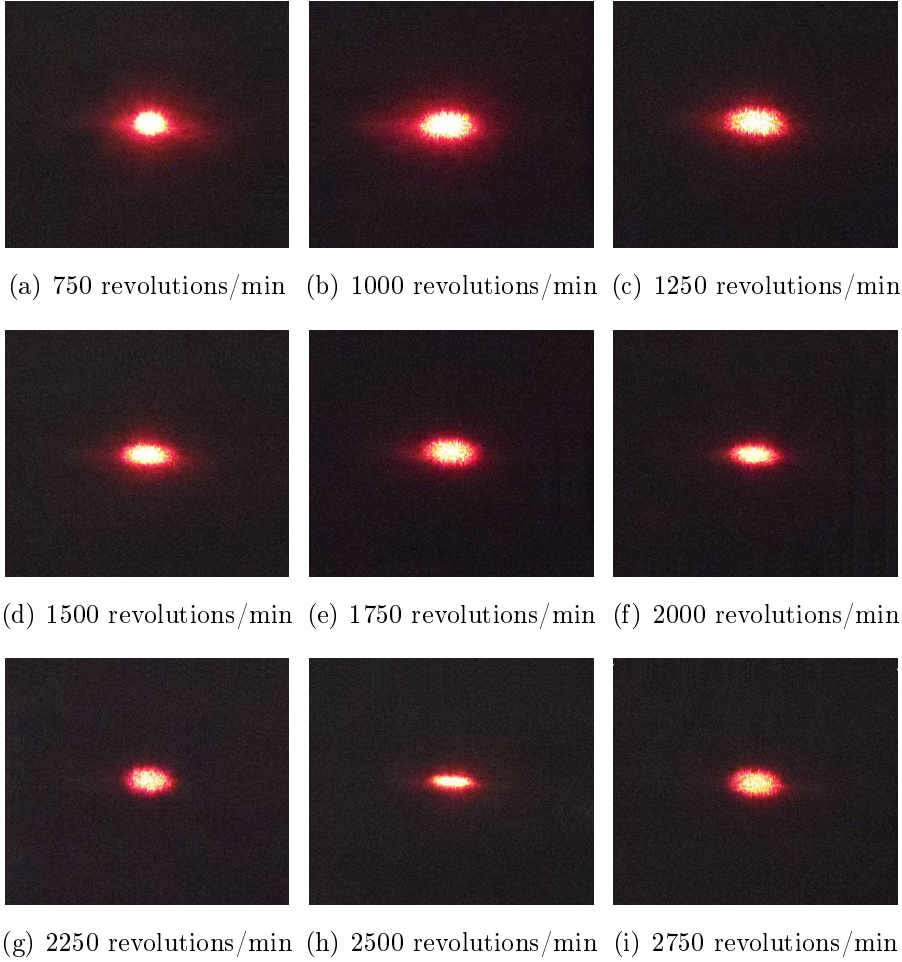(g) 2250 revolutions/min (h) 2500 revolutions/min (i) 2750 revolutions/min

Figure 3.12: [a-i] Photographs for each set pump velocity (in revolutions/minute) of the laser beam in transmission after the WGJ.

hours of continuous optical measurement.

To test the optical stability a series of measurements were performed using the configuration schematically shown in Fig. 3.9(b). The difference from the previous setup (Fig. 3.9(a)) is that a small pinhole was placed on the edge of the beam where the beam fluctuations are maximal, and the WGJ system was filled with pure water. Under the worst conditions (high flow rate, $RTD \sim 3\%$) the RMS of measured signal does not exceed 1%, i.e. it is less than the instability of the jet thickness caused by fluctuations of the gear pump. In the center of the optical beam the signal fluctuations are much lower than at the edge. In case of very thin jet films, especially at low `RPM` of the pump, the jet itself becomes less stable and the thickness fluctuations increasingly affect the optical stability due to the larger optical strength of the formed lens. Between $0.1\,\mathrm{mm}$ and $0.2\,\mathrm{mm}$, the jet is stable, and above these values, the fluctuations of the thickness increase non-linearly (see Fig. 3.11).

3.3.5 Evaporation of liquid

For long-term optical measurements, keeping the concentration of the sample at a constant level is very important, especially in time-resolved transient absorption experiments where uncontrollable changes in concentration can lead to artifacts during data collection. The concentration of the sample can change in the WGJ because of evaporation of solvent from the surfaces of the jet and from the opening of the collector, since this is an "open-space" system. An evaporation test was conducted to characterize the system's concentration stability. The system was filled with a solution based on a sample used in ultrafast pump probe studies of $(dG)_4$ and left running for an extended period of time at a pump speed of $1500\,\mathrm{rpm}$. $(dG)_4$ is a single strand of DNA formed by four guanosines linked by a ribophosphate backbone. The sample was purchased from Jena Bioscience GmbH (Germany) in a lyophilized form, and used without any further purification. The compound was desalted and purified by the vendor and has an extinction coefficient of $\varepsilon = 47000\ \mathrm{M^{-1}cm^{-1}}$ at $260\,\mathrm{nm}$. It was solvated in a phosphate-based buffer (see Section 2.2 for more details), with pH between 7.5 and 7.6 for the duration of the experiment. The WGJ system was filled with a known quantity of solution (the "dead" volume of the system is $1\,\mathrm{ml}$). The concentration of the sample was determined to be
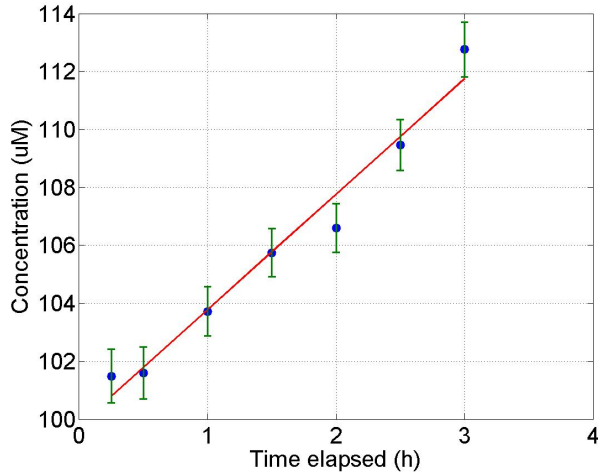
Figure 3.13: Variation of sample concentration during the evaporation test. The red line is a linear fit.

$103\,\mu$M prior to the experiment by recording the absorption at $253\,$nm (quartz cuvette with $1\,$mm inner path length).

The variation of concentration with time was calculated by monitoring the OD of the solution while the jet was running. The measured OD vs. running time and resulting concentrations are plotted in Fig. 3.13. The linear fit (green line) gives the speed of the concentration change as $4\,\mu$M per hour:

$$c = 4 * t + 99.8, \tag{3.3}$$

where c is the concentration in μM, and t is the elapsed time in hours. After three hours the overall increase in the sample concentration was $\sim 10\%$.

It is safe to assume that the quantity of $(dG)_4$ accumulated onto different surfaces of the WGJ system (tubes, sandwich block, wires, interior of the gear pump) is negligible since the materials chosen are chemically resistant and non-adsorbing. In addition, a series of measurements were performed so that if there is a small absorption of the sample, it will nonetheless be saturated after a few runs. There were no visible signs of deposition.

Using the fitting coefficients from Eq. 3.3 and the final sample concentration, the drop of volume in the case of water-based solvents can be estimated to be $100\,\mu$l per hour. In case of alcohols as solvents, evaporation rates are much higher. In the particular case of ethanol, the evaporation rate was measured to be $0.5\,$ml/h.

In long-term experiments larger volumes of solutions are used, typically $5-6\,\mathtt{ml}$ for biological samples and up to $10\,\mathtt{ml}$ for alcohol-based solutions. The longest pump-probe scan takes about 30 min (acquisition of one 2D-spectrum takes approximately 5 min); during this period the overall change of concentration is less than 1%.

3.4   Conclusions

As part of this study, a closed-loop wire-guided jet system was developed for ultrafast spectroscopic experiments in the VIS and the deep UV. Design details and the full characterization of the *WGJ* are included. The *WGJ* is a compact standalone system. It is versatile and can be fitted in a standard pump-probe or 2D spectrometer. The *WGJ* can run for a period of several hours without significant changes in the parameters of the jet, such as thickness, liquid layer, and flow speed. The most important parameters of a jet - the stability of the thickness of the liquid film, and the influence of fluctuations of the thickness on optical stability - were measured, as well as the rate of sample/solvent evaporation.

This *WGJ* allows sufficient sample exchange rate for laser repetition rates of up to 4 KHz (0.1 mm spot sizes) with stable pathlengths and less than 0.8% variation in the thickness of the jet. On the edge of the outgoing laser beam, the associated optical stability is better than 1 %. The evaporation of solvents limits lengthy operation of our *WGJ* to ~ 1 hour without any notable change in sample concentration. However, this is the drawback of an open-space system and is easily fixable with automated addition of solvent to the jet, for example in the collector.

This *WGJ* is tested in ultrafast experiments. It is currently the dedicated system for all time-resolved studies that require liquid samples and femtosecond laser pulses. One example is UV transient absorption experiments, where change in the absorbance of the samples is measured at the level of $100\,\mu\mathtt{OD}$ with $8\,\mathtt{fs}$ pulses.

Chapter 4

Methods: 2D Photon echo and pump-probe spectroscopy

This section describes the optical setup developed in the laboratory and used for acquiring the experimental data presented in the next chapters.The section begins with the commercial laser and then gives detailed account of all the steps that allow the creation of a broadband UV spectrum in the wavelength range of $250\,\text{nm}$ to $300\,\text{nm}$, as schematically illustrated in Fig. 4.1.

Briefly, after the commercial laser, the output beam passes through a homebuilt two-cascade non-collinear optical parametric amplifier (NOPA), a homebuilt achromatic second harmonic generation (ASHG), a homebuilt 2D spectrometer, a homebuilt sample holder (*WGJ*, described in Ch. 3) and eventually to a commercial spectrometer, a motorized monochromator from Newport (Oriel 74125). The system is depicted in the flow diagram in Fig. 4.1. The commercial laser is a Ti:Sapphire regenerative amplifier (Legend Elite, from Coherent Inc.). It is pumped at $532\,\text{nm}$ by a $Nd:YVO_4$ commercial laser (Micra, from Coherent Inc.). The oscillator emits 60 fs pulses centered at $800\,\text{nm}$.

Parts of this chapter can also be found in two different conference proceedings from Prokhorenko, Picchiotti et al.[30,31], of which the author of this study is an author.
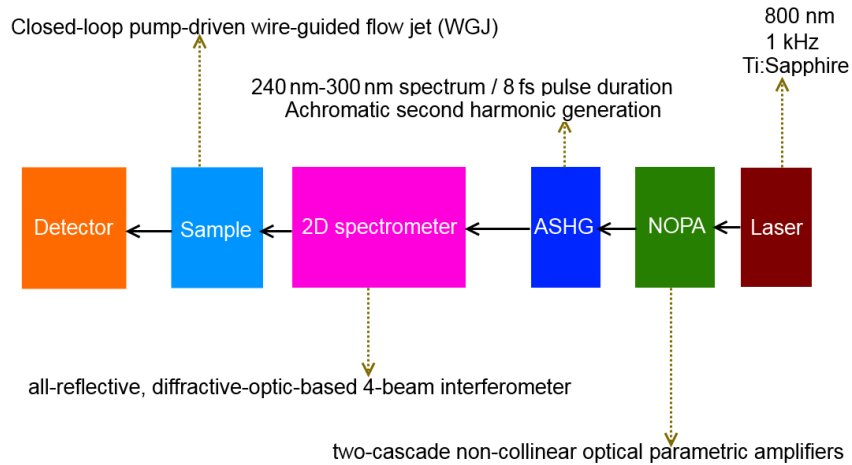
Figure 4.1: Flow diagram of the nonlinear infrared experiment consisting of a commercial Ti:Sapphire laser system, a homebuilt two-cascade NOPA, a homebuilt ASHG, the homebuilt nonlinear experimental setup (2D spectrometer), the homebuilt sample holder *WGJ*. The signal is detected by a Newport Oriel 74125 motorized monochromator (the detector). More details can be found in the text.

4.1 Two-cascade Non-collinear Optical Parametric Amplifier

4.1.1 Theoretical introduction

An optical parametric amplifier (OPA) is a laser light source emitting tunable wavelengths using a particular type of light matter interaction, (optical) parametric amplification, also called difference frequency generation. This process, when occurring in a suitable nonlinear crystal, transfers energy from a high-power, fixed high frequency beam (the *pump*) to a low-power, lower tunable frequency beam (the *signal*), and as a side-product, generates a third beam (the *idler*). The signal beam amplified by an OPA is a light source able to emit light with a tunable wavelength range and a considerably high bandwidth.[147–150]

Clearly, energy and momentum are conserved during the process:

$$\hbar\omega_p = \hbar\omega_s + \hbar\omega_i \tag{4.1a}$$

71

$$\hbar\vec{k}_p = \hbar\vec{k}_s + \hbar\vec{k}_i \qquad (4.1b)$$

where p stands for pump, i for idler and s for seed, $\vec{k}$ are the wave vectors, and ω the frequencies of the three beams, and the following relation is valid[151]:

$$\omega_i < \omega_s < \omega_p \qquad (4.2)$$

Equation 4.1 describes the phase-matching condition, ensuring that a proper phase relationship between the three interacting waves is maintained along the propagation direction. Only when the phase-matching condition is fulfilled (phase mismatch is zero or close to zero), are amplitude contributions from the different beams all in phase at the end of the nonlinear crystal, and it is possible to obtain an efficient nonlinear interaction.

A detailed mathematical description of the optical parametric amplification process For a detailed mathematical description of the optical parametric amplification processis well-described in Boyd[152], Shen[153] and Cerullo.[151] For brevity, only the main equations are reported, starting with the Manley-Rowe relationship:

$$\frac{1}{\omega_i}\frac{\mathrm{d}I_i}{\mathrm{d}z} = \frac{1}{\omega_s}\frac{\mathrm{d}I_s}{\mathrm{d}z} = -\frac{1}{\omega_p}\frac{\mathrm{d}I_p}{\mathrm{d}z} \qquad (4.3)$$

This equation states that energy flows from the two lower frequency fields (idler and signal) to the sum-frequency field (pump), and conversely from pump to idler and signal. The photon conservation is fulfilled, that is, one photon at frequency ω_p is split into a photon at frequency ω_i and another at ω_s. The peculiarity of optical parametric amplification with respect to the similar process of difference frequency generation is based on the initial conditions. In particular the signal beam has a much weaker intensity than the pump beam and gets significantly amplified during the interaction, while at the same time the idler beam is generated.

In a classical OPA, the degrees of freedom are the signal and idler group velocities and the phase matching bandwidth of the process. The choice of the nonlinear crystal, for a certain wavelength, will determine the phase matching conditions. For example, considering a negative uniaxial crystal, for which phase matching of type I is achieved when:[151]

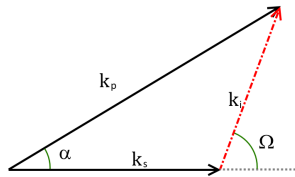$$n_{pe}(\theta_m)\omega_p = n_{so}\omega_s + n_{io}\omega_i \qquad (4.4)$$

Figure 4.2: Schematic showing the wave vectors involved in the phase matching of a NOPA.

where the subscripts e and o stand respectively for extraordinary and ordinary, and refer to the axes of a birefringent crystal. The above equation shows that there is a dependence of the phase matching condition on the angle θ_m, the angle between the wave vector of the propagating beams and the optical axis of the nonlinear crystal.

The pump and the signal wave vectors are collinear in a traditional OPA, but the angle between them (α) can also be varied, forcing the idler to emit at an angle Ω with respect to the signal. This angle introduces an extra degree of freedom into the OPA, therefore the new name NOPA (non-collinear optical parametric amplifier), as shown in Fig. 4.2. The advantages of such a geometry are evident in literature[151,154,155], mainly the three group velocities of pump, idler and signal are better matched, diminishing the group velocity mismatch.

When a very short visible seed pulse is injected into the (BBO) crystal, the generated idler pulse is still propagating inside the crystal with a different velocity than the signal pulse $v_{gi} > v_{gs}$. As these two pulses travel inside the crystal, they mutually amplify, but because of the velocity mismatch the new photons are added onto the leading edge of the signal pulse, lengthening it.

Within this non-collinear geometry, equation 4.1 becomes a vectorial equation, with a parallel and a perpendicular component of the equation with respect to the signal wave vector:

$$\Delta k_{\parallel} = k_p \cos \alpha - k_s - k_i \cos \Omega = 0 \qquad (4.5\text{a})$$

$$\Delta k_{\perp} = k_p \sin \alpha - k_i \sin \Omega = 0 \qquad (4.5\text{b})$$

Either by expanding the above equations to the first order, as in equations 32a and 32b in Cerullo et al. 2003[151] or by differentiating them with respect to the signal wavelength, as in equations 10 and 11 in

73

Riedle et al. 2000[155], there are two differential equations where variation of the three wave vectors when varying the frequencies (or the wavelengths) are related to each other and to the two angles Ω and α. Remembering the (broad band) phase matching condition $\Delta \vec{k}$ must vanish:

$$\frac{\mathrm{d}\vec{k}_i}{\mathrm{d}\omega_i} - \cos\Omega \frac{\mathrm{d}\vec{k}_s}{\mathrm{d}\omega_s} = 0 \tag{4.6}$$

which is equivalent to:

$$v_{gs} = v_{gi} \cos\Omega \tag{4.7}$$

Therefore, in practice one adjusting the angle Ω between the seed and the idle beams, it is possible to achieve zero group velocity mismatch, hence improving the temporal compression of the pulses. The generation of a broadband signal to exploit the broadband phase-matching of the NOPA is commonly realized by continuum light (white-light generation).[155]

White light generation (WLG) with femtosecond pulses is mainly generated by self-phasing modulation, whose role is to a certain extent greater than other effects (quantum noise, self focusing, avalanche ionization) depending on pulse duration.[156,157] Other effects (self-steepening, optical "shock- wave" formation, space–time focusing, plasma generation by multi-photon ionization, chromatic dispersion) also play a role.[157,158]

4.1.2 Experimental setup for the NOPA

The NOPA implemented in the laboratory is home-built, and has two cascades (or passes), each one based on a $1\,\mathrm{mm}$ thick BBO with type I phase matching, and each one an efficiency of $\approx 20\%$ (Fig. 4.3). As mentioned in the previous subsection, with NOPA it is possible to compress the output (signal) pulse.

After the laser beam is split in two by the 50% beam splitter BS1, one of the two beams is sent to the white-light generator, based on a sapphire crystal placed between one focusing lenses and one off-axes parabolic mirror (OAPM), this creates a white-light spectrum that extends between $450\,\mathrm{nm}$ and the fundamental $800\,\mathrm{nm}$.[159] The remaining beam is sent to a BBO crystal (BBO3) for second harmonic generation, the resulting beam, which pulses are centered at a wavelength of $400\,\mathrm{nm}$, is split in two by the beam splitter BS2. These two beams,
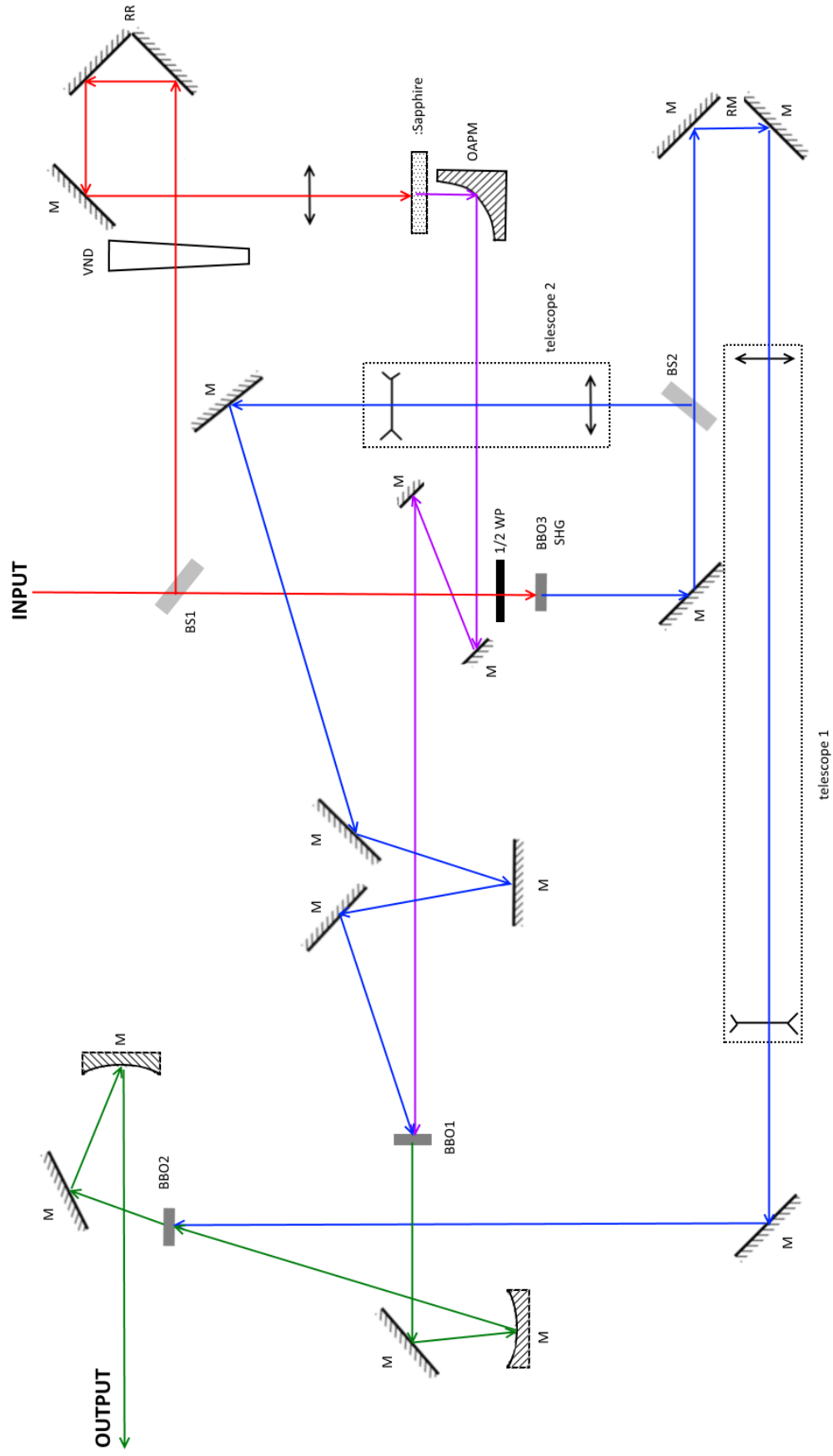
Figure 4.3: Schematic of the home-built two-cascade noncollinear optical parametric amplifier; the input is the beam from the commercial laser, the output beam is sent to the second harmonic generation (see Sec. 4.2).
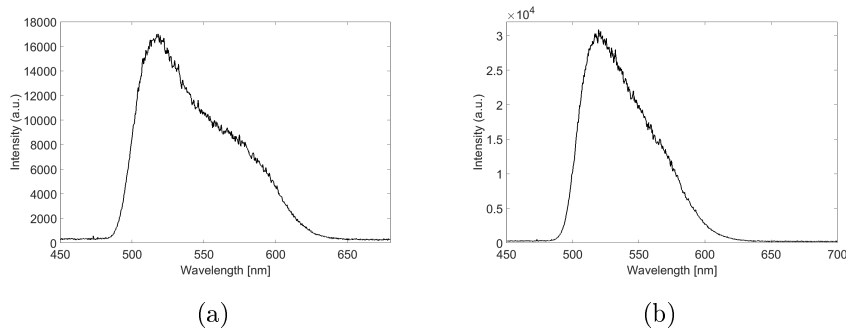
Figure 4.4: Top: typical spectra of the beam emerging from the NOPA. (a) First cascade NOPA, and (b) Second cascade NOPA

each demagnified via a telescope, will pump the two NOPA stages located at the BBO crystals (BBO1 and BBO2). A retro-reflector (RR) and a roof mirror (RM) both mounted on translational stages on each beam path, serve to reach the temporal overlap. The spatial overlap is achieved by the use of a series of coupled mirrors.

The main purpose of adding a second cascade NOPA into our setup is to increase the final output power, to the detriment of the complexity of the system. The measured power of the beam emerging from the first cascade NOPA is 650 to $700\,\mathrm{nJ}$, while the power of the beam from the second cascade NOPA is $8\,\mu\mathrm{J}$. The first BBO crystal (BBO1) is fed with the WGL and with one of the two beams at $400\,\mathrm{nm}$, the output is used on the second BBO crystal (BBO2) with the other beam at $400\,\mathrm{nm}$.

The first cascade NOPA produces a first broadband spectrum centered at $500\,\mathrm{nm}$ and with a bandwidth of $485-600\,\mathrm{nm}$. In like manner, the second cascade NOPA produced a final broadband spectrum centered at $500\,\mathrm{nm}$ and with a bandwidth of $490-600\,\mathrm{nm}$. A typical recorded spectrum is shown in Fig.4.4(a) and 4.4(b) for the first and second cascade spectra respectively, recorded through a commercial spectrometer (Avantes). The photos on the bottom of Fig. 4.4 show the beam on a black and white background for the respective cascades. Note the slightly reddish component on the bottom left of the blue-green beam in the first cascade and a slight oblungation of the beam when the second cascade is active.

4.2 Achromatic second harmonic generation

Because a direct source of ultrashort UV pulses is not available, it is necessary to produce it from visible light by second harmonic generation (SHG) or by sum-frequency mixing. Simultaneous phase matching of all spectral components in the UV would require a crystal thinner than $5\,\mathrm{um}$, therefore with very low conversion efficiency. To overcome the bandwidth limitation in SHG, it has been proposed that the broadband light is first angularly dispersed.[160] Achromatic phase matching (APM) is a relatively recent technique that allows each frequency component to propagate in the non linear crystal with its individual phase matching angle, if angularly dispersed. APM can double in frequency a spectrum with extremely broad band width, and it does so by phase matching all spectral components simultaneously, to eventually generate pulses with extremely short time width. Operationally, APM is achieved by varying the separation of the prism and the focal length (first order), and by choosing the appropriate material and apex angles of the prisms (sign and magnitude of the second order). The scheme is based on a simple prism sequence for achieving high-order achromatic phase matching. First and second order achromatic phase matching are possible by appropriately focusing on the crystal with two off-axis parabolic mirrors and by inserting two prisms before and three after the crystal.

The setup employed in the laboratory is shown in Fig. 4.5, and it is based on an already published setup.[161] The output beam from the NOPA is sent to two fused silica prisms P1 and P2 that spatially disperse it, before doubling its frequencies with a type I BBO. The efficiency of the crystal is $\approx 20\%$. An achromatic half-wave plate is inserted after P1 and P2, in order to rotate the beam polarization to be perpendicular to the spectral distribution; this fulfills the achromatic phase-matching condition for type I SHG.[160] The prisms P3 to P5 are used to compensate the spatial dispersion of the UV pulse, gathering all the spectral components to the same spot and therefore collimating the output beam.

The BBO is immediately preceded and followed by two off-axis parabolic mirrors (OAPM1 and OAPM2) to frequency double in a confocal manner, avoiding the beam passing through lenses that would introduce more unwanted chirping and stretch the pulse further. The
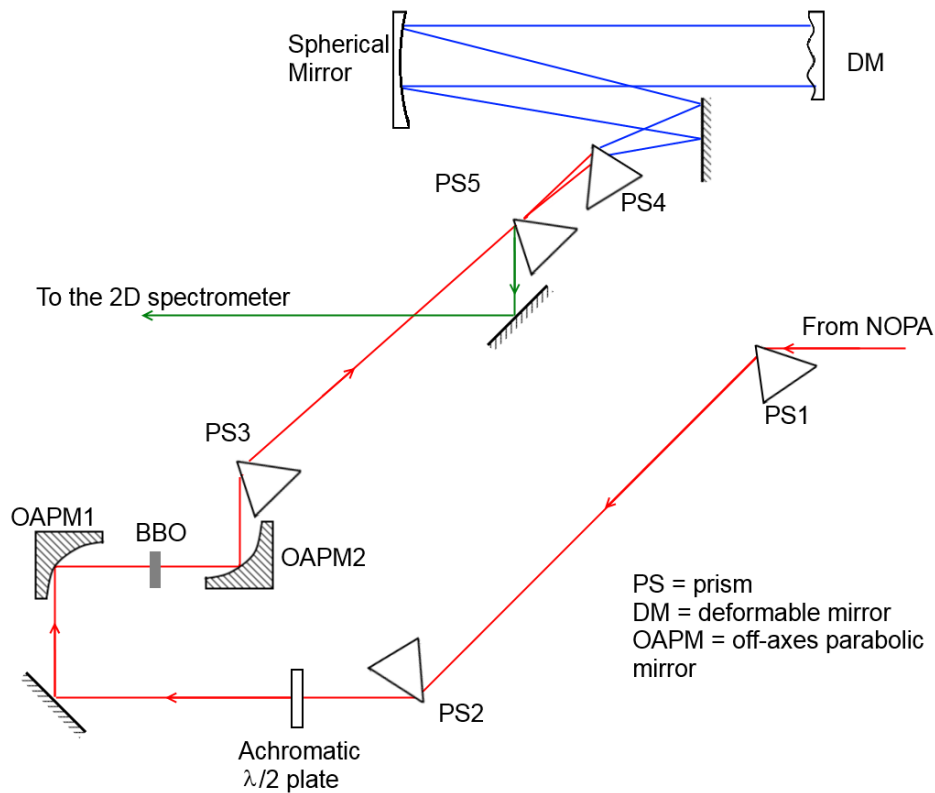
Figure 4.5: Schematic of our home-built achromatic second harmonic generation. The incoming beam on the right is the output of the NOPA (see Sec. 4.1.2) and the output from the ASHG setup on the left is sent to the 2D spectrometer.

BBO crystal is moved a bit away from the focus to reduce the intensity and avoid damage to the crystal. The re-collimation of the beam is implemented by another identical OAPM and by three fused silica prisms (P3 to P5) cut for Brewster's angle. The beam emitted by the BBO crystal passes through a P3 prism, then through P4 (over P5 but without passing through it). The role of P4 is to double the spatial width of the spectrum on a deformable mirror (DM).[161] After the DM, the beam goes back following almost the same path, reflected back by a spherical mirror. It passes through P4 again, at a lower height than before and then through P5, thereby recombining to a collimated broadband beam.

Almost all the spectral width of the beam emerging from the NOPA is transferred to the second harmonic (Fig. 4.6). The UV pulses have an energy of $650 - 750\,\mathrm{nJ}$ after compression, at the exit of the ASHG setup. Changes in the compression of the beam can be effected by scal-
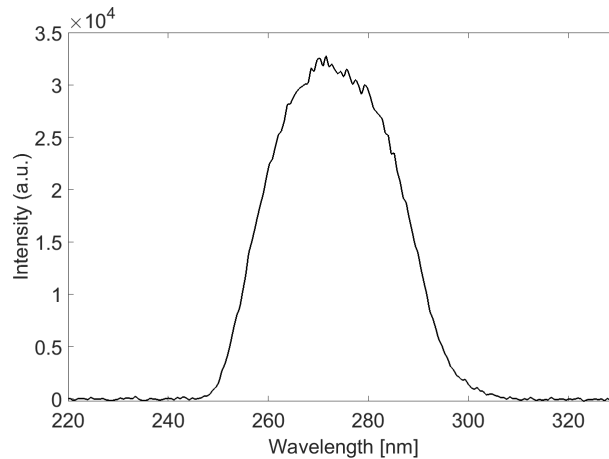
Figure 4.6: Typical UV spectrum of the beam emerging from the ASHG. The measured power in this case was $640 \, \mathrm{nJ}$. The spectrum spans from $33000 \, cm^{-1}$ to $40000 \, cm^{-1}$ (240 to $300 \, nm$) and its bandwidth is $\approx 7000 \, cm^{-1}$ ($50 \, nm$).

ing the prism separation and the focal length of the OAPM, without interfering with the behavior of the achromatic doubling.[161] The chirp of the incoming pulses is compensated by the ASHG setup itself, with the use of P1-P5 (linear chirp) and DM (higher-order chirp). There is still a bit of chirp at the position of the crystal, but this has the advantage of avoiding sum-frequency generation between the different components of the NOPA spectrum.[161] The emerging UV spectrum spans from $33000 \, cm^{-1}$ to $40000 \, cm^{-1}$ (240 to $300 \, nm$) and its bandwidth is $\approx 7000 \, cm^{-1}$ ($50 \, nm$) (Fig. 4.6).

4.2.1 Characterization of the UV pulse

Through a homebuilt frequency-resolved optical gating (FROG[162,163]) it was possible to characterize the output beam after the ASHG (Fig. 4.6). The pulses have a duration of 6 to $8 \, \mathrm{fs}$ depending on the alignment of the ASHG. the FROG is based on custom made two-dimensional diffractive optics (DO) from Holoeye (Fig. 4.7). The set-up was successively modified to become the 2D spectrometer for this study (see Sec. 4.3). The output beam from the ASHG is sent to a off-axis parabolic mirror (OAPMM1 from Newport) and focused into the DO. The out-coming four first order diffracted beams, all identical, are than sent to two retro reflectors, beams 1 and 2 are reflected by RR1, mounted on a motorized translational stage (MTS, VP-25XL from Thorlabs) and beams 3 and 4 are sent to RR2. Beam 4 is ei-
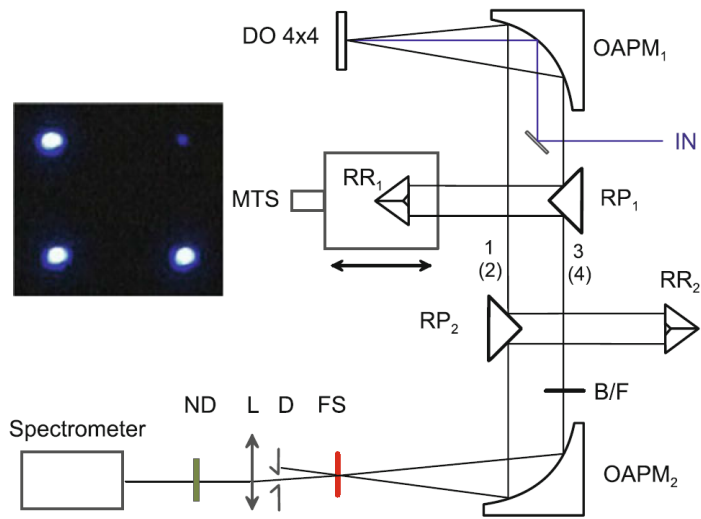
Figure 4.7: Schematic of the home-built FROG setup. The inset shows the incoming beams and the faint FROG signal in the left-upper corner, generated by four-wave mixing of the three bright beams.
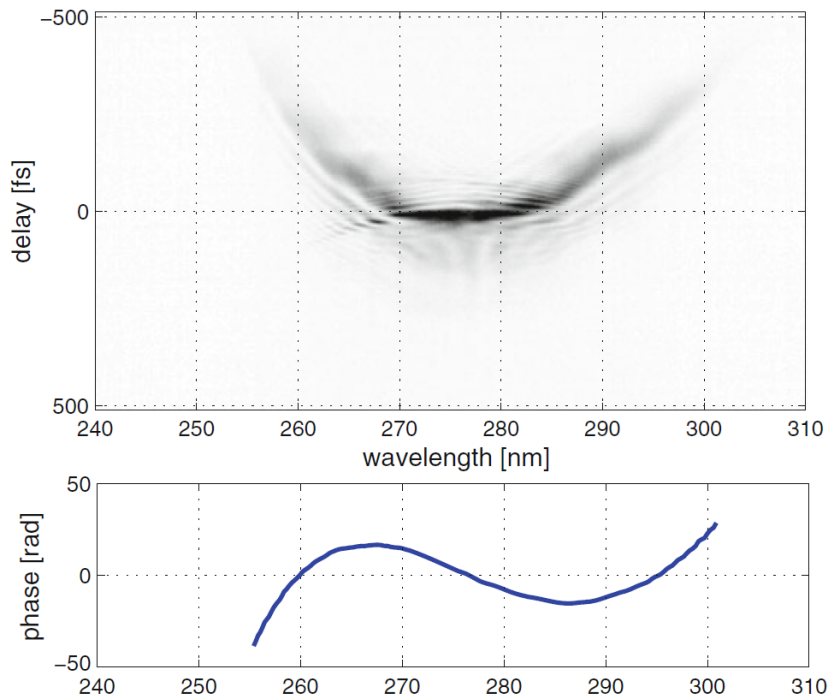

Figure 4.8: (top) FROG trace of the uncompressed UV pulse, when the deformable mirror is not activated and (bottom) its retrieved phase profile, the shape is clearly ascribable almost completely to a third-order chirp in the beam.

ther blocked completely, to obtain a homodyne signal, or attenuated

with a $200\,\mu m$ thick neutral density filter with OD equal to 2. The beam blocker or the substituted density filter are put in position B/F (Fig. 4.7). The four beams are focused through another OAPMM (OAPMM2 also from Newport) into a UV grade fused silica window (FS), with a thickness of $150\,\mu m$. The outcome is either a faint homodyne signal generated by four-wave mixing of beams 1, 2 and 3, or a stronger heterodyne signal when the three beams are mixed with the attenuated 4th beam. The advantage of heterodyning the signal is that its sensitivity is enhanced by one order of magnitude compared to the homodyne-detected FROG signal. However there is no algorithm in the literature for retrieving the pulse shape and phase.

The UV-enhanced DM from Flexible Optical B.V., is based on a membrane with 64 actuators on its back, and its main purpose is to compensate for the third and higher order chirps present in the beam (Fig. 4.8). The linear (second order) chirp is not present, due to full compensation by the prisms in the ASHG setup. An analytical and a genetic algorithm were developed that can be used with the DM, to optimize the signal and thereby minimize the chirp. The result is stunning, as the pulse width is reduced from a couple of hundreds of femtoseconds to approximately $7\,\mathrm{fs}$. Fig. 4.9 shows an example FROG trace, done with the commercial program Femtosoft Technologies, to retrieve the pulse shape. On the right of Fig. 4.9 there is the retrieved phase profile, which is almost flat on top, and the pulse with a FWHM of $32\,\mathrm{nm}$, centered at $272\,\mathrm{nm}$. The duration of the pulse in the example shown in Fig. 4.9 is of $7.3\,\mathrm{fs}$, very close to the transform-limited pulse ($6\,\mathrm{fs}$).
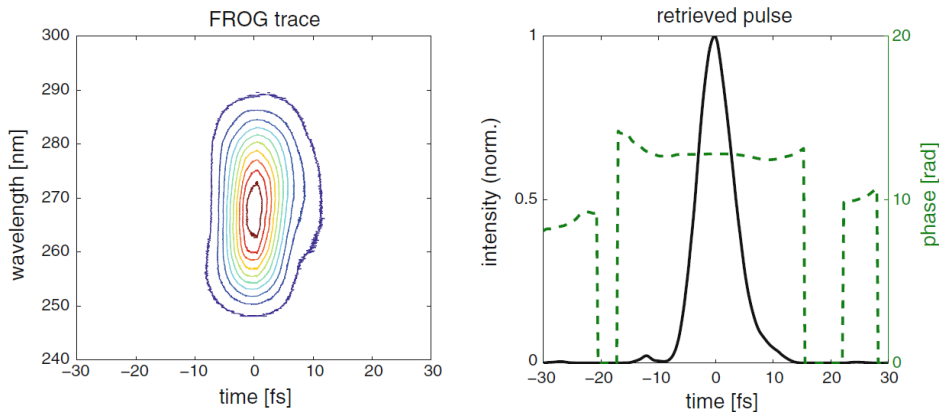
Figure 4.9: On the left a representative FROG trace and on the right the retrieved temporal profile (solid) and retrieved phase (dashed) of the compressed pulse after the activation of the deformable mirror.

4.3 The 2D setup

The previous sections described the two stages that allow the delivery of a broadband UV beam. This beam is used in the third stage, the 2D spectrometer (2DUV), where the beam is divided into four replicas that are then decoupled from each other with the use of translational stages. This stage is the core of the setup and is used to create and manipulate the four beams (three pumps and one probe) necessary for photon echo spectroscopy and at the same time, it can be conveniently transformed into a transient absorption setup.

A schematic of the 2DUV is shown in Fig. 4.10, the setup is all-reflective, to avoid any light scattering and stretching of ultrashort pulses if the beam were to pass through a window; see the introduction of Ch. 3 for a more complete discussion. To create the necessary four beams, a reflective diffractive optics (DO), with a crossed grating (Holoeye) was inserted right after two focusing parabolic mirrors. Only the first order of the reflected peaks is selected, with an efficiency of 60%. This is in contrast to previously developed 2D-setups[164], where the main difference is the use of transmissive optics and retroreflectors. In the present set-up these are replaced by DO and roof-mirrors to decrease the number of reflections, ergo more energy is transferred to the sample).

With the use of four 45° roof mirrors, three of which are mounted on two separate translational stages (XMS-50, Newport), the four beams are completely uncoupled. The left pair of beams 3(4) passes

beam	power
	$[\,\mu\mathtt{W}\,]$
beam 1	15.9
beam 2	11.6
beam 3	15.5
beam 4	11.0

Table 4.1: Power measured for each of the four beams emerging from the diffractive optics (DO).

through the roof mirror RM1, mounted on the translational stage DL2; the right pair of beams 1(2) is sent to RM2, mounted on DL1. After all four beams are collected together, they are sent to another two roof mirrors, the bottom couple of beams 2-4 is reflected by RM3, mounted on DL1, while the top couple 1-3 is sent to RM4, where beam 1 is chopped with a chopper (ratios 4/4 or alternatively 7/7). This setup is based on an extant design[165], with a second pass of the beam 2 through DL1 (with RM3), in the opposite direction of the first pass (with RM2). Now the scan of the "waiting" delay time T and the "dephasing" delay time τ are independent, this modified setup achieves good phase stability and has demonstrated overall robustness through its use.

The temporal width of the pulses is measured each *in situ* measurement, and gives values between $7\,\mathtt{fs}$ and $10\,\mathtt{fs}$. This comparable to the measurements carried out with the FROG (See Sec. 4.2.1). The most recent characterization of the power of the beams after the DO gives the values in Tab. 4.1.

The heterodyne detection is done by inserting a neutral density filter with $OD = 2$ and thickness $200\,\mathtt{nm}$ in the path of the beam 4 (LO filter in Fig. 4.10). Conversely, the transient absorption measurements are carried out by blocking beams 2 and 4, with a flag shutter (PP Shutter in the schematic of Fig. 4.10), and homodyne detection is possible by blocking the local oscillator beam with an independent shutter (LO shutter).
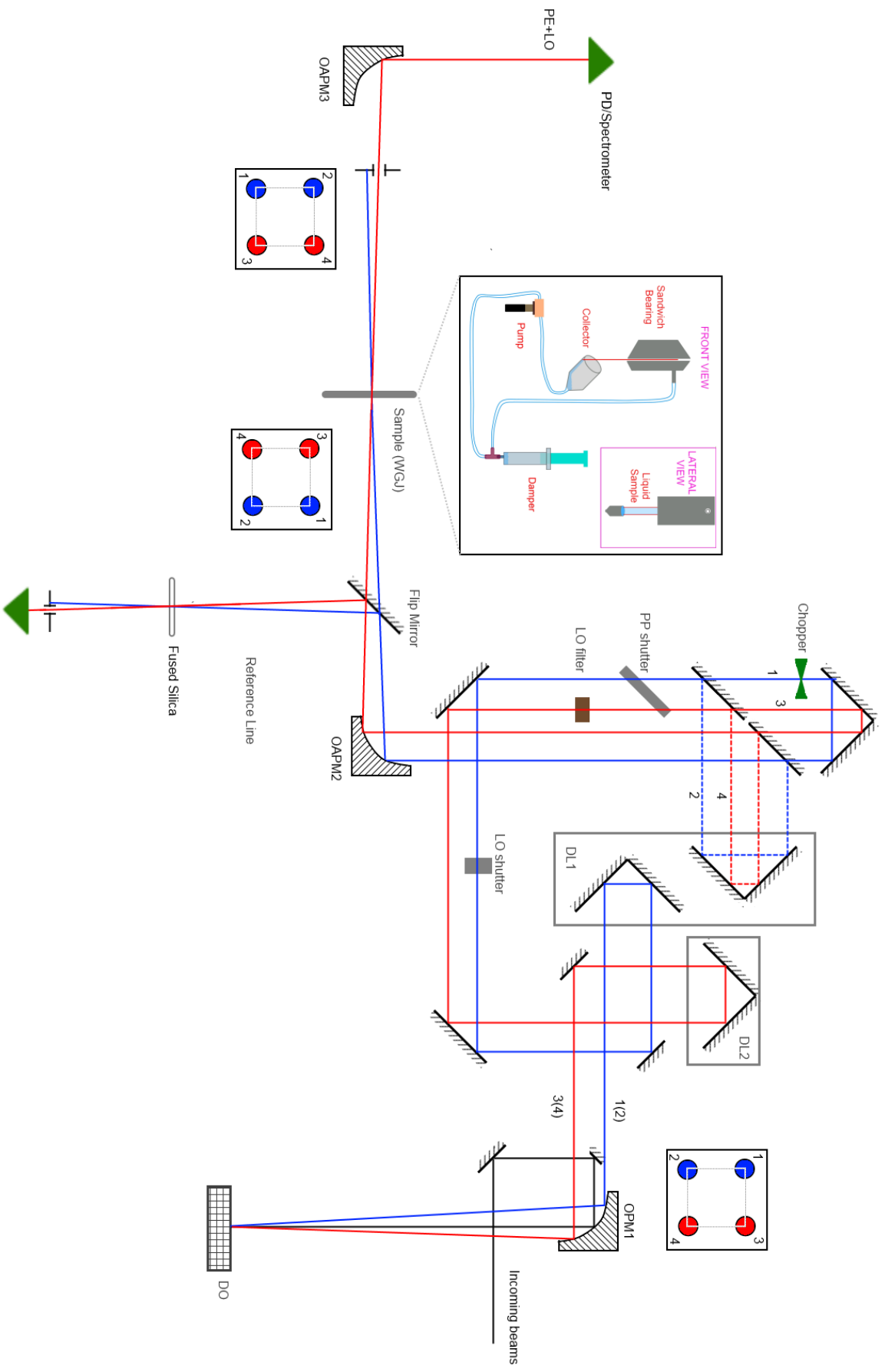
Figure 4.10: Schematic of the home-built all-reflective 2D spectrometer, based on diffractive optics and an interferometer geometry.

4.4   Collection and analysis of data

To achieve a sufficient signal to noise ratio, the final spectra are averaged from many spectra. Depending on the strength of the output signal the number of spectra varies between 100 and 400. Consequently, the collection of a photon echo (PE) spectrum can vary from five minutes to up to ten, and a transient absorption (TA) spectrum acquisition from thirty to ninety minutes depending on the range and precision of the waiting time T.

The collection of PE spectra is always performed on the same day as the TA spectra, to have the same experimental conditions, and to phase the PE spectra properly with the TA spectra. PE spectra were individually phased with their corresponding TA spectrum (at the same T), following the procedure described in Ref.[164]. TA spectra were fit with a multi-exponential model using a home-written software based on global fitting analysis.[166] For each set of experimental data presented in this work, more technical details are given in the methods sections of each chapter.

Chapter 5

2D Photon echo, transient grating and transient absorption spectroscopy of pyrene

This chapter presents the first time-resolved results of this study, collected on pyrene, a well-known UV-absorbing dye that was used for characterizing the experimental setup. This section is based on a paper to be submitted by Picchiotti, Nenov, Giussani, Prokhorenko, Garavelli and Miller.

The computations were performed by Artur Nenov and Angelo Giussani. The author is very grateful to Professor Henning Tidow for granting access to his fluorimeter, with which the static fluorescence spectra were acquired.

5.1   Motivation and Introduction

The following sections are dedicated to the first experimental results, based on pyrene, a well-known and characterized dye.[19–25] Given its high transition dipole strength, well-known electronic transitions, and relatively small chemical structure (Fig. 5.1), this dye is a perfect candidate for the characterization of such a novel (experimental and simulated) set-up.

Biological molecules generally have complicated dynamics, thus disentangling the different de-excitation channels has proven more difficult than expected, leading to an ongoing debate among experts.[167]
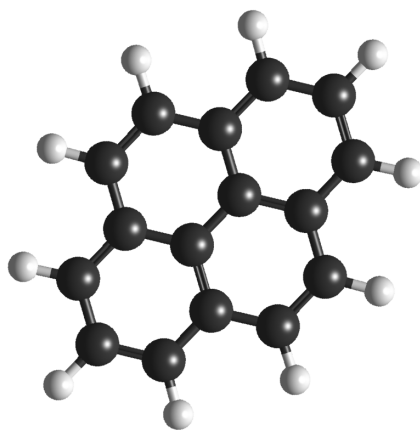
Figure 5.1: Chemical structure of pyrene in the ground state.

Generally, there is a lack of theoretical models that predict the excited state dynamics of electronic excitations in this wavelength range, and it is imperative to develop solid theoretical grounding by starting from simpler molecules, whose excitation pathways are more easily discerned. Moreover, all reported photon echo (PE) and transient absorption (TA) experiments in the deep UV were conducted in a one-color fashion with a small bandwidth pump, limiting the type of information extractable from the experimental data.[22,35,36]

The objective of the work presented here is to push the present limitations, both from an experimental and a theoretical standpoint, by demonstrating the capabilities of the techniques developed here. This is done by applying those techniques to pyrene, a relatively simple molecule, whose absorption overlaps perfectly with the experimental UV spectrum, and whose excited state dynamics are not complicated. Moreover, the clear Franck-Condon progression of pyrene makes it easier to disentangle vibrational and electronic excitations. The set-up is able to generate a broadband spectrum between $250\,\mathrm{nm}$ and $300\,\mathrm{nm}$.[30] Consequently one can follow the complete de-excitation dynamics of pyrene from the S_3 level.[25]

In parallel, theoretical work has lately become more precise[168–170] and recent published work has shown that it is possible to simulate electronic excitations in the near UV with an elevated accuracy and relatively low computational cost.[168,171–174] The previous theoretical work[171], where electronic excitations were simulated in the near UV, has been extended by the theoretical collaborators to a higher wavelength range and applied to the new experimental spectra of pyrene.

Moreover, this is the first high-resolution simulated and experimental 2D spectrum in the deep UV which resolves not only the vibronical structure of the bleaching but also includes ESA (excited state absorption) contributions, and is therefore able to detect Raman frequencies in both the ground and excited states. An analysis of those Raman frequencies detected in the experiments and in the simulation of pyrene is presented.

5.2   Sample preparation

Pyrene was purchased from Radiant Dyes GmbH and used as is, without further purification, and diluted in ethanol, either spectroscopic or HPLC quality. The concentration was adjusted in order to have an OD of ≈ 0.3 in maximum absorbance, determined with a commercial spectrometer (Shimadzu 2600) in a quartz cuvette of 1 or $10\,mm$ path length (Hellma). The solution was filtered using a syringe pump (Aladdin 300- 220Z syringe pump from WPI) in a $5\,mL$ syringe, at a speed of $0.5\,mL/min$. The filters were composed of an hydrophobic PTFE membrane with pore sizes of 0.45 and $0.22\,\mu m$ (Carl Roth). The frequency-resolved 2DPE signals were collected with a scan range of $128\,fs$ and a step of $1\,fs$ at fixed waiting times T. The absorption spectra of the employed samples were controlled before and after each experimental set.

The static fluorescence emission spectrum of pyrene in ethanol was acquired using a Cary Eclipse fluorimeter in a fluorescence quartz cuvette of $10\,mm$ path length (Starna). Excitation was set to $260\,nm$, excitation slit was $20\,nm$, while emission slit was $1.5\,nm$. Average time was set to be 5 seconds.

In order to minimize light scattering and pulse broadening, the solutions were circulated through a home-built wire-guided jet with the thickness in excited volume maintained at $\approx 200\,\mu m$ (see Ch. 3). The excitation spot size was $\approx 50\,\mu m$ and, with the jet pump speed used $(3000-3500\,rpm)$, a refreshment of excitation volume was guaranteed for the laser repetition rate ($1\,kHz$). The UV-pulse excitation energies were $15-20\,nJ$ per beam.

At each delay point 250 to 500 single spectra were averaged to achieve high SNR. Each photon echo scan took approximately 2 to 5 minutes per one delay point T . The pump-probe spectra were typically collected in a delay range of either $10\,ps$ with a step of $20\,fs$, or $200\,ps$

with a step of 100 `fs` . Each delay point is the result of averaging 3600 differential spectra (pump-on / pump-off). In the present chapter, the differential spectra are plotted as measured, without normalization to the probe spectra. In order to achieve the high spectral resolution needed for resolving the oscillations, the delay step was set to 5 `fs` in HTG (heterodyne transient grating) measurements and the associated TA (transient absorption) measurements (performed for phasing). PE spectra were always collected concurrent with a TA spectrum at the same population time T, and PE spectra were individually phased with their corresponding TA spectrum (at the same T). TA spectra were fit with a multi-exponential model using a home-written software based on global fitting analysis.[166] Fitting of the experimental data was performed through multiple home-written software within the Matlab shell. For a rationale on global analysis fitting of pump-probe data, see Sec. 6.3, for details on the mathematical treatment of 2D spectra see Ref.[164].

5.3   Computational methods

5.3.1   Electronic structure and excited states

The calculations for the characterization of the electronic structure of pyrene were performed using the complete active space self-consistent field (CASSCF) approach[175,176], augmented by second order perturbation theory (CASPT2)[177,178] in its single-state (SS) flavor. The restricted active space (RAS) variation of the scheme (i.e. RASSCF/ RASPT2)[179,180] was used, which reduces the number of simultaneous excitations, thus allowing active spaces containing all valence pi-orbitals. Excited state optimizations were performed with D2h symmetry and at the RASSCF (4,8|0,0|4,8) level of theory, thereby distributing the orbitals of the system between RAS1 and RAS3 allowing for up to quadruple excitations. The stationary nature of the obtained critical points was verified by frequency computations (w/o symmetry). Due to the lack of analytical gradients for RASSCF the frequency computations were performed at CASSCF(8,8) level, only after each geometry was first relaxed at this inferior level and it was verified that no significant changes occurred. Conical intersections (CIs) were optimized by using the restricted Lagrange multipliers technique as included in the Molcas 8 package.[181] The energies of the ten lowest

excited states of the system were recomputed at the critical points at SA-10-CASSCF(2,4|8,8|2,4)/ ANOL[3s2d1p/2s1p]//SS-CASPT2 level in order to better evaluate the energetics. Individual critical points on the potential energy hypersurface were connected via linear interpolation of the internal coordinate (LIIC). The ANO-L basis set, contracted to C[3s,2p,1d]/H[2s1p], was used[182], and the Cholesky decomposition was adopted[183] in order to speed up the evaluation of two-electron integrals. The electronic structure computations and geometry optimizations were performed using Molcas 8.[184] Parameters for the lineshape functions necessary to describe the spectral dynamics (see chapter 6.3.2 for details) were obtained from an adiabatic SA-3-CASSCF(4,4)/6-31G* mixed quantum-classical dynamics simulation in the S4 state (being the second excited state with this reduced active space of four electrons and four orbitals) for 100 fs with a time step of 0.5 fs and zero starting velocity, thereby including the highest occupied molecular orbital (HOMO, H), the lowest unoccupied molecular orbital (LUMO, L), H-1 and L+1 and the corresponding electrons. 100 higher lying states were obtained at a SA-100-RASSCF(4,8|0,0|4,8)/ ANO-L[3s2d1p/ 2s1p]// SSCASPT2 level every `2 fs`. The mixed quantum-classical dynamics were performed through the velocity Verlet algorithm implemented in COBRAMM and interfaced with Molcas 8 for obtaining quantum-mechanical gradients.[185]

5.3.2   2D spectroscopy

In 2D ES, three wave-matter interactions induce a nonlinear polarization that emits a signal along a given phase-matched direction, and is recorded as a function of the time-intervals between the pulses. The time-dependent intensity and phase of the third-order signal are recovered via heterodyning with a fourth pulse (the local oscillator):

$$
S^{(3)}(\tau, T, t) = \int_{-\infty}^{\infty} dt' \int_{0}^{\infty} d\tau \int_{0}^{\infty} dT \int_{0}^{\infty} dt \quad R^{(3)}(\tau, T, t) \times
$$
$$
\mathbf{E}(r, t')\mathbf{E}(r, t' - \tau)\mathbf{E}(r, t' - \tau - T)\mathbf{E}(r, t' - \tau - T - t)
$$

(5.1)

The local oscillator involves three temporally separated interactions with the electric field $\mathbf{E}(r, t') = E(t')e^{ikr - iwt'}$ with a central frequency ω and a complex envelope $E(t')$. The response $S(3)(\tau, T, t)$ depends parametrically on the delay times τ, T and t between the field-matter interactions. Often the time-dependent signal is Fourier-transformed

along τ and t to obtain the 2D spectrum for each waiting time T. In the simulations the impulsive limit (white light pulses of infinitesimally short duration) is adopted, and the emitted signal becomes proportional to the non-linear response $R^{(3)}(\tau, T, t)$. The latter is a sum of the different pathways of system density operator propagation, which can be categorized into ground state bleach (GSB), stimulated emission (SE) and excited state absorption (ESA). Furthermore, depending on the ordering of the interactions, it is possible to distinguish between rephasing (k_I) and non-rephasing (k_{II}) signals. It should be noted that the quasi-absorptive signals presented in this work contain both rephasing and non-rephasing contributions.

Pyrene is treated as a three-level system consisting of a ground state (g-manifold), a single bright electronic state S_3 in the first excited state manifold (i.e. the e-manifold) within the envelope of the experimentally utilized pump-pulse pair, and a number of higher lying states in the f-manifold accessible through the probe pulse. 2D ES signals are simulated in the sum-over-states approach with the response function $R^{(3)}(\tau, T, t)$ formulated in the cumulant expansion to second order[88,186,187] and expressed within the formalism of lineshape functions. In the following the expression for the rephasing ESA is explicitly formulated

$$
\begin{aligned}
R^{(3)}_{\mathbf{k_I}, ESA}(\tau, T, t) = -i \sum_f & \left|\mu_{eg}\right|^2 \left|\mu_{ef}\right|^2 e^{+i\omega_{eg}\tau} e^{-i\omega_{ef}t} \\
& \times \left\{ e^{-g_{ee}(\tau+T+t)+g_{ee}(\tau+T)-g_{ee}(\tau)-g_{ee}(-t)} \right. \\
& \times e^{+g_{ee}(-T-t)-g_{ee}(-T)+g_{ef}(\tau+T+t)-g_{ef}(\tau+T)} \\
& \left. \times e^{+2g_{ef}(-t)-g_{ef}(-T-t)+g_{ef}(-T)-g_{ff}(-t)} \right\}^*
\end{aligned}
\tag{5.2}
$$

μ_{ij} are transition dipole moments that couple the states i and j, ω_{ij} are the electronic transition frequencies, and the pure dephasing processes in the system due to the coupling of the electronic and vibrational degrees of freedom are constructed from the lineshape functions $g_{ij}(t)$ with a complex dependence on the delay times. The second order cumulant expansion is exact within the framework of the displaced harmonic oscillator (DHO) model and the lineshape functions have exact analytical solutions.

$$
g_{ij}(t) = \sum_k \frac{\omega_k \tilde{d}_{ik} \tilde{d}_{jk}}{2} \left[\coth(\beta\omega_k/2)(1 - \cos(\omega_k t)) + i(\sin(\omega_k t)) \right].
\tag{5.3}
$$
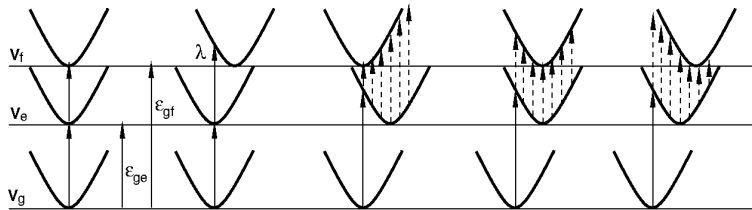
Figure 5.2: Various realizations of the relative displacement of the harmonic potentials of the singly (e-manifold) and highly (f-manifold) excited state manifolds with respect to the equilibrium.

The ES potential energy surface of every electronic state of pyrene is approximated as a multi-dimensional uncoupled harmonic potential, with each state from the e- and f-manifolds described through its mass-weighted relative displacements from the GS potential $\tilde{d}_{ik} = \sqrt{m_k} d_{ik}$ along each mode k with a frequency ω_k. Within this framework, the dynamics can be expressed through a superposition of undamped oscillators with frequencies ω_k and weighting factors (i.e. Huang-Rhys factors) proportional to the relative displacements $\tilde{d}_{ik}$ (Fig. 5.2), leading to multiple oscillatory diagonal and off-diagonal features in the 2D ES spectra reflecting the vibrational structure of the electronic states. Together with the pure electronic transition energies ω_{eg} and ω_{fg} (5.2 and Fig. 5.2) these parameters describe fully the coherent undamped dynamics of the system.

The parameters are obtained from a single 100 fs mixed quantum-classical dynamics simulation with zero initial velocity (i.e. a $0K$-trajectory) initiated in the S_3 state by computing the electronic structure (g-, e- and f-manifolds) at selected points. The choice of a reference Hamiltonian acting on the classical bath during a coherence propagation, as is the case for the delay times τ and t, is not unique as the bra and the ket side of the density matrix are subject to different electronic potentials. Furthermore, the nuclear degrees of freedom are propagated as if interacting with the state S_3. The extraction of the energy fluctuations of the states from the f-manifold must be performed in a diabatic representation in order to stay within the framework of the uncoupled harmonic oscillators, as the high state density in the visible and near UV causes the potentials of the higher lying states to cross multiple times, and the resulting adiabatic potentials are no longer harmonic. Thus the evolution of the wavefunctions should be followed instead.[171]

The extracted data series from the $0K$-trajectory were then fitted

to the analytical expression for the classical time-dependent fluctuation of the $S_3 - S_n$ energy gap (n belonging to a state from either the g- or the f-manifolds)

$$V_n(t) - V_e(t) = -\sum_k \omega_k^2(\tilde{d}_{ek} - \tilde{d}_{nk})\tilde{d}_{ek}\cos(\omega_k t)+$$
$$+\sum_k \frac{\omega_k^2(\tilde{d}_{ek} - \tilde{d}_{nk})^2}{2} + (\omega_{ng} - \omega_{eg}) \tag{5.4}$$

with $h = \{g, f\}$ which allows the extraction of the mass-weighted displacement coefficients $\tilde{d}_{ek}$ and $\tilde{d}_{fk}$, as well as the electronic transition energy ω_{eg} and ω_{fg} (the parameters $\tilde{d}_{gk}$ and ω_{gg} describing the ground state are zero per definition). In the DHO framework, the spectral dynamics of the ESA are a function of the dynamics in the photoactive state S_3, i.e. of the relative displacement of the higher lying ES PES with respect to the PES of the photoactive state; these can induce positive or negative frequency correlations (Fig. 5.2). By definition this is restricted to the normal modes describing the molecular dynamics in the e-manifold; i.e. if d_{ek} is zero, than so is d_{fk}. This is implied by the missing state-specific modes that can only be obtained by performing the dynamics of each state excited by the probe pulse. With the parameters extracted from the above fitting, it becomes possible to compute the lineshape functions $g_{ij}(t)$ (5.3) and eventually the nonlinear response (5.2). Although the derivation of the working equations (5.2) is based on the Franck-Condon (FC) approximation, whereby transition dipole moments are independent of the nuclear coordinates, their fluctuations along the dynamics are accounted for in a semi-classical fashion by using the FC values for the first and second interaction with the pump pulse, while taking the values at time T for the interaction with the probe pulse and the local oscillator.

So far, this describes the coherent vibrational dynamics in the S_4 state. These underline the vibronic structure in the system's 2D spectrum, but no broadening is yet included. To realistically describe peak shapes a composite spectral density with a fast component is assumed, due to the coupling to a bath of low-frequency solvent modes next to the slow component from the undamped molecular vibrations. Thus each lineshape function in 5.3 (and the respective GSB and SE contributions) is supplemented by a lineshape function for a single over-damped Brownian oscillator[188] in the high temperature limit

$$g(t) = \frac{\lambda}{\gamma}\left(\frac{2}{\beta\gamma} - i\right)\left(e^{-\gamma t} + \gamma t - 1\right) \tag{5.5}$$

93
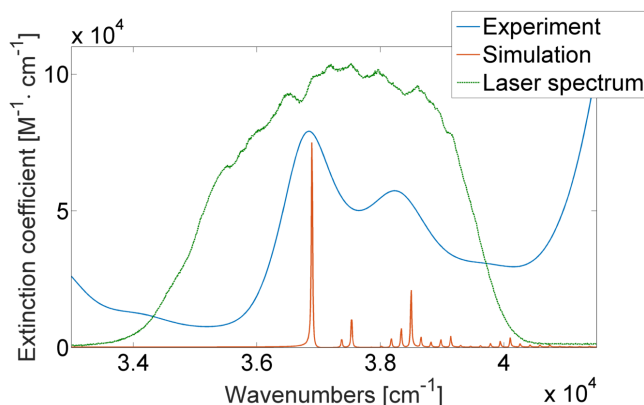
Figure 5.3: Experimental and simulated absorption spectra of pyrene, overlapped with the experimental laser spectrum.

with λ the reorganization energies. A correlation time constant of $50\,\texttt{fs}$ and phenomenological reorganization energies of $300\,\texttt{cm}^{-1}$ for the state-specific lineshape functions g_{ee} and g_{ff}, as well as of $200\,\texttt{cm}^{-1}$ for the coherences g_{ef} were used.

5.4 Photodynamics of pyrene

Fig. 5.3 presents the experimental deep-UV linear absorption (LA) spectrum of pyrene dissolved in ethanol (blue line), with the spectral envelope of the broad-bandwidth UV pulse superimposed over it (green dashed line) and the simulated spectrum (red line) without broadening to highlight the underling contributions to the individual bands. A well-resolved vibronic progression with peaks at 272.40, 261.80 and 251.80 nm is seen. Previous work attributed this progression to the allowed bright transition to state S_3 with oscillator strength of $\sim 0.25\,\texttt{D}^2$ and electronic structure B_{2U}.[25] Although the LA spectrum is generally quite informative about the electronic and vibrational structure, it is substantially less so regarding the relaxation of the excited population. Time-resolved multi-pulse techniques are required to study the dynamics of the system upon excitation. High temporal resolution, required for resolving ultra-fast processes, is achieved only through ultra-short pulses. A benefit of the temporal compression is the broad bandwidth which allows probing of the temporal evolution of state-specific signals in a broad spectral window. In the following, both experimental and theoretical transient absorption (TA) and photon echo (PE) spectra are presented.

(a)

(b)

(c)

(d)
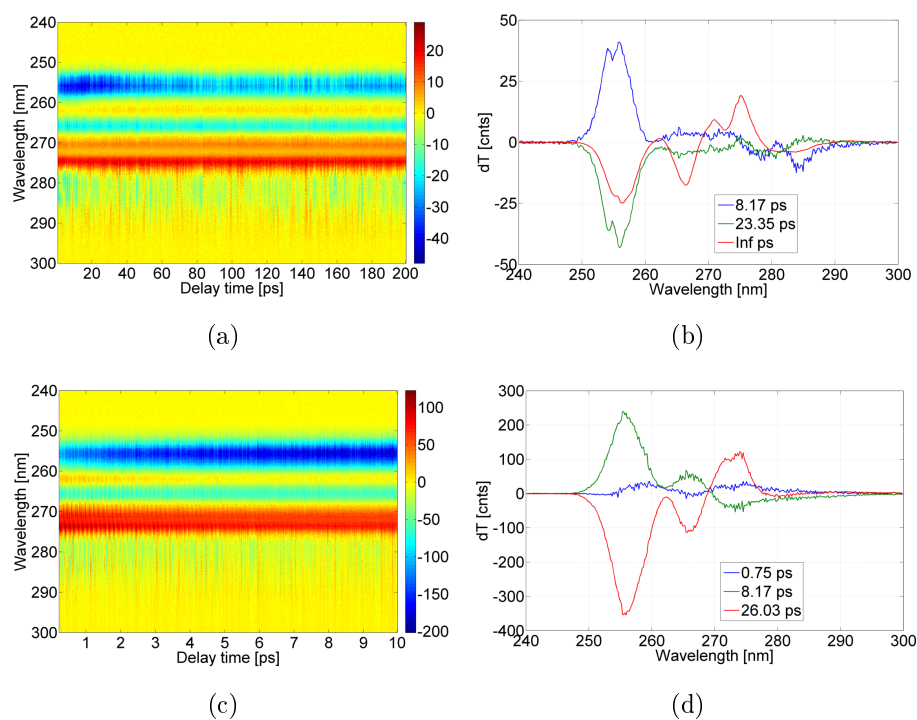
Figure 5.4: Left: Pump-probe (TA) kinetics of pyrene in ethanol, experimental spectra. Colors are in dT (counts/a.u.) Right - decay associated spectra resulting from the fitting of the TA on the left. Vertical axes in dT (counts/a.u.). Top row: long scan study up to 200 ps with 500 fs step, bottom row: short term study up to 10 ps with 20 fs step.
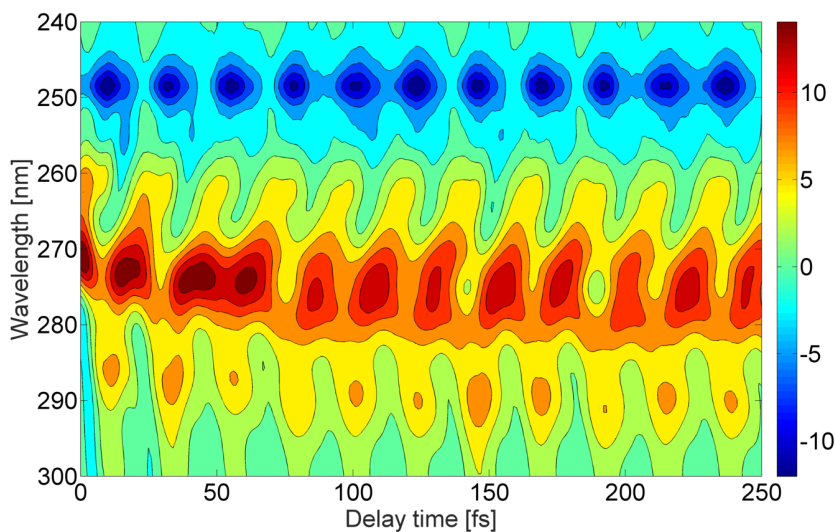
Figure 5.5: Simulated TA spectrum of pyrene in ethanol.

Figures 5.4 (a) and (c) show the transient pump-probe spectrum of pyrene up to 200 ps. Due to the undesirable scattering effects of the solvent, which are particularly strong at waiting times $T_2 < 200$ fs when the incoming pulses overlap in the sample[189], the ultra-fast dynamics of pyrene cannot be resolved. Therefore, the experimental results are supplemented with a theoretical simulation up to 250 fs. The experimental spectrum reveals pronounced dynamics in the intensity of the main traces. While the bleach at 272 nm (in red) loses intensity within the first few picoseconds, the ESA band at 255 nm (in blue) gains intensity. Thus, relaxation dynamics are expected to occur on a sub-to-few ps time-scale, in agreement with the broadening of the LA spectrum. The small bleaching at 261 nm that matches the second vibronic band of the S_3 state in the LA spectrum (Fig. 5.3) is also present in the experimental TA spectrum, although very faintly due to the overlap with the strong excited state absorption (ESA) at 255 nm. Additionally, the theoretical spectrum (Fig. 5.5) reveals a Stokes shift of 5 nm leading to broadening of the ground state bleaching (GSB) contribution at 270 nm, and a clear stimulated emission (SE) contribution at 283 nm which is absent for longer decay times.

To quantify the long-time behavior of pyrene, the decay associated spectra (DAS - Figures 5.4 (b) and (d)) were extracted, thereby obtaining two short (0.75 and 8 ps) and two long (24 and infinity) lifetimes (Fig. 5.4). The 0.75 ps lifetime (blue line) are associated with the initial increase of the intensity of the ESA band (positive contribu-

96
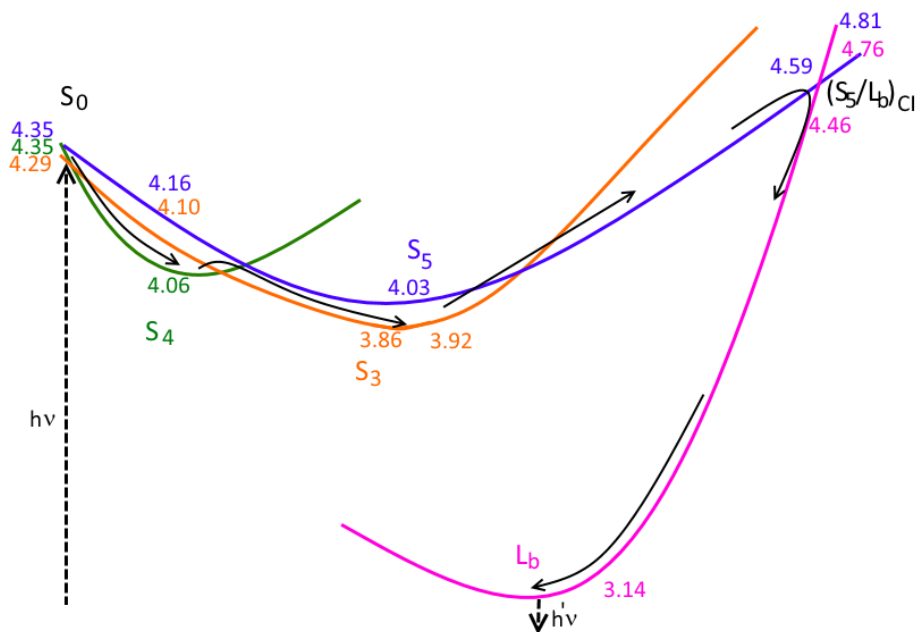
Figure 5.6: Schematic representation of the main decay paths after excitation into the bright S_4 state. Energies in eV with respect to the ground state at the ground state minima are also reported. Solid orange, solid green, solid violet, solid pink lines indicate the evolution of the system on the S_3, S_4, S_5, L_b states, respectively.

tions around $255\,\mathrm{nm}$) accompanied by the decrease of the bleach in the $272\,\mathrm{nm}$ region, followed by a vibrational cooling process (using a conventional interpretation of the data) with a $8\,\mathrm{ps}$ lifetime (green line) which blue-shifts the maxima of the contributions. The decrease of the ESA intensity at later times can be fitted with another exponential curve characterized by a $24\,\mathrm{ps}$ lifetime. The infinitely long lifetime can be representative either of ESA decay and GSB recovery, or a S_1 bottleneck trap (see following text), or sum of multiple phenomena.

In order to shed light on the changes in the electronic and geometric structure of pyrene, the possible deactivation mechanism was followed through ES energy minimization techniques, allowing for the identification of the intermediate states most likely to be populated in the course of ES deactivation. The relaxation pathways are summarized in figure 5.6. The computation at the FC (Frank-Condon) point of pyrene shows the presence of another two proximate electronic states in the vicinity of the bright S_4 (typically identified as S_3 in literature), denoted as S_3 and S_5. Despite lying only about $0.06\,\mathrm{eV}$ above S_4, S_3 (referred to as the phantom state for clarity), is spec-

State	Main CSF	$E_{VA}[\text{eV}]$	f
S_0		0.00	-
S_1 (L_a)	H$\rightarrow$ L+1 34%	3.37	0.00
	H-1$\rightarrow$ L 32%		
S_2 (L_a)	H$\rightarrow$ L 64%	3.64	0.22
	H-1$\rightarrow$ L+1 14%		
S_3	H$\rightarrow$ L+2 22%	4.29	0.00
	H-2$\rightarrow$ L 13%		
S_4	H-1$\rightarrow$ L 32%	4.35	0.25
	H$\rightarrow$ L+1 31%		
S_5	H-2$\rightarrow$ L 35%	4.35	0.00
	H$\rightarrow$ L+2 31%		
S_6	H$\rightarrow$ L 15%	4.51	0.00
	H$\rightarrow$ L+3 15%		
	H-3$\rightarrow$ L 14%		

Table 5.1: Vertical excitation energies (EVA, eV) of the low-lying excited states of pyrene computed at the SA-10-RASSCF(2,4|8,8|2,4)/ANO-L[3s2d1p/2s1p]//SSCASPT2 level at the symmetry optimized ground state minimum. Oscillator strengths from the ground-state (f) and the main configuration-state functions (CSF) describing each state are also reported.

troscopically dark and not directly accessible. Moreover the bright S_4 is degenerate with the also dark S_5. S_3 and S_5 are characterized by a very similar nature, and are in fact mainly described by the same configuration state functions (see Table 5.1). However, the molecular dynamics simulation demonstrates that the phantom state and S_4 exhibit similar energetic profiles along the S_4 MD, thereby remaining in close vicinity throughout the entire simulation. Furthermore, near the S_4 equilibrium the energy gap is reduced to $0.03\,\mathrm{eV}$ at the FC point. This allows for an efficient non-adiabatic population energy transfer between both states, attributed to the shortest lifetime of $0.75\,\mathrm{ps}$. The population transfer to the phantom state is followed by thermalization with a lifetime of $8\,\mathrm{ps}$. A conical intersection occurs between the S_4 state (becoming the adiabatic S_4 state upon relaxation) with the dark L_b configuration (giving rise to the S_1 state at the FC point). Despite lying at considerably higher energy above the S_4 minimum, this CI is accessible and could rationalize the $24\,\mathrm{ps}$ lifetime resulting from the global fitting.

Previous experiments[22,190] pumping in the near-UV (thus, accessing the S_2 state only of pyrene) have revealed sub-100 fs relaxational dynamics to the first ES of L_b character where the system remains trapped on a ns-timescale. A tentative assumption is that once reaching the L_b state over the $S_4 \rightarrow S_3$ cascade the system exhibits similar dynamical features. This is further supported by fluorescence excitation spectra which show that the fluorescent quantum yield from S_1 does not depend on which electronic bands are excited (S_2, S_3, or S_4), instead scaling with the molar absorptivity.[35,191] This is consistent with the physical image of population becoming trapped in the bottleneck S_1 state for hundreds of picoseconds or even nanoseconds time-scales.[22,190]

Static fluorescence spectra were collected to support the proposed mechanism by exciting at $260\,\mathrm{nm}$ (Fig. 5.7). The fluorescence spectrum is symmetric to the absorption spectrum, and the peak structure between approximately $360\,\mathrm{nm}$ and $450\,\mathrm{nm}$ is associated to emission from the S_1, while the small shoulder between approximately $350\,\mathrm{nm}$ and $368\,\mathrm{nm}$ has been associated to emission from the S_2 as long as the excitation involves S_2 by Baba et al.[35], as such emission appeared only when pyrene vapors are excited at the wavelengths $37600\,\mathrm{cm}^{-1}$ ($266\,\mathrm{nm}$) and $42900\,\mathrm{cm}^{-1}$ ($233\,\mathrm{nm}$). Furthermore, in Fig. 5.7 there is a small feature between $267\,\mathrm{nm}$ and $300\,\mathrm{nm}$ visible in the zoomed bottom
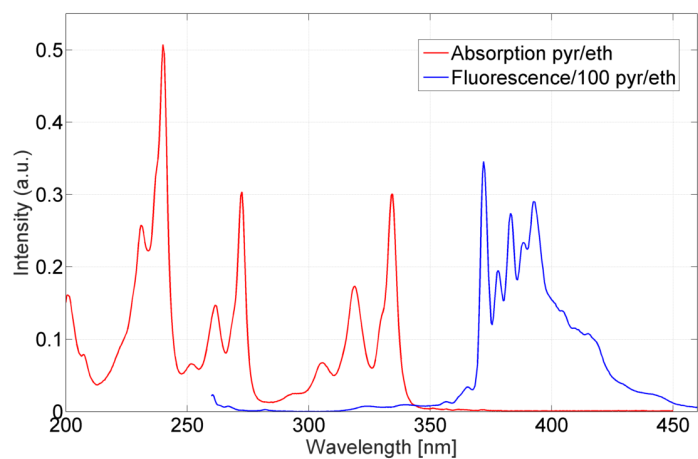
(a)
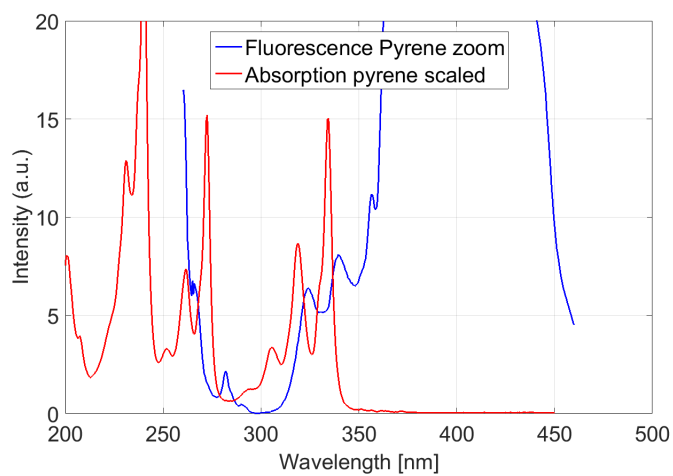
(b)

Figure 5.7: Static fluorescence emission spectrum of pyrene in ethanol. Excitation was set to $260\,\mathrm{nm}$, excitation slid was $20\,\mathrm{nm}$, while emission slid was $1.5\,\mathrm{nm}$. Average time of acquisition for each wavelength was set to be 5 seconds.

spectrum of Fig. 5.7; this feature is not discussed in the literature. Due to the very low quantum yield of this transition as compared to S_1 fluorescence, such peaks are associated to an ultrafast relaxation (possibly even to the phantom state).

From the static fluorescence spectrum proposed here, it is possible to conclude that the excitation of the S_4 is followed by a sub-picosecond relaxation of the excited population to the phantom state S_3, then to the S_2 ($8\,\mathrm{ps}$) and finally to the S_1 states ($24\,\mathrm{ps}$). This is not supported by the present calculations, which show only one conical intersection, between S_3 and L_b (that in the minimum assumes characteristics of S_1). In any case, the population is trapped for a very long time in the S_1/L_b bottle-neck minimum before relaxing to the ground state, with time-scales longer than the experimentally allowed time-scale maximum ($200\,\mathrm{ps}$). Alternatively, what was previously identified with fluorescence from S_2 ($350-368\,\mathrm{nm}$), is instead a relaxation from the L_b, right after the CI with the phantom state lasting $24\,\mathrm{ps}$, and the S_2 level is not involved at all in the de-excitation dynamics.

It is true that the proposed mechanisms are unconventional, as the various de-excitation pathways following the S_2 excitation proposed in literature[19,22,35,190–196], are not extended to the bright S_4 (previously known as $S3$) state. Nevertheless, the presence of conical intersections in ultrafast photo-decay processes of pyrene have been already investigated for other wavelength ranges.[197] Currently, higher level computations are being performed to improve the simulations, to confirm the proposed mechanism, and in particular to determine with greater precision the energy gaps between the minimum of the phantom state S_3 and the CI with L_b, and to search for other possible CIs.

5.5   2D Photon echo spectroscopy of pyrene

Fig. 5.8 shows a comparison between the experimental and simulated spectra at $T = 200\,\mathrm{fs}$, with a clear checkerboard pattern, the frequency values of the corresponding peaks are presented in table 5.2. In appendix A.3, the experimental PE spectra for other selected waiting times T are shown. By comparing the experimental spectra of Fig. 5.8 with the simulated one, the GS bleach at $(36.68, 36.65)\,\mathrm{cm}^{-1}$ corresponds to the simulated spectra at $(36.5, 36.7)\,\mathrm{cm}^{-1}$, and $(36.72, 38.04)$ cm^{-1} corresponds to $(36.5, 38.0)\,\mathrm{cm}^{-1}$. The signals from the simulated spectra at probe frequencies less than $36.5\,\mathrm{cm}^{-1}$ belong to the Stoke
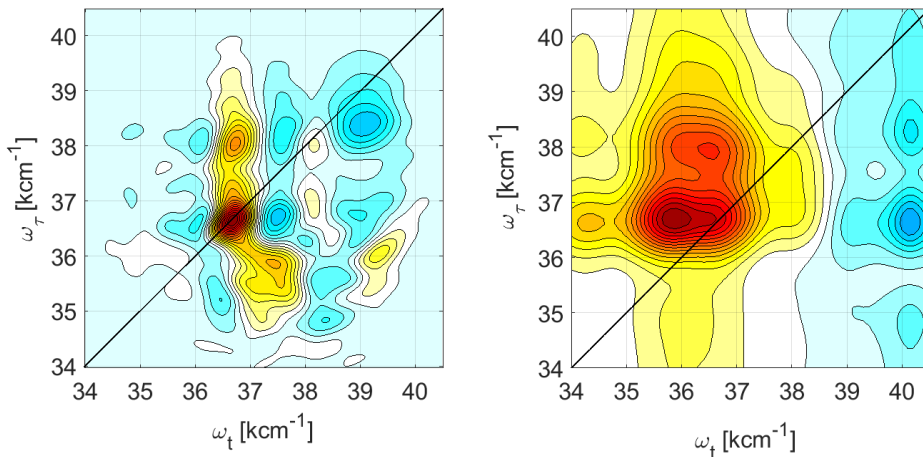
Figure 5.8: 2D maps of pyrene in ethanol at $T = 200\,\mathtt{fs}$. Left: experimental, right: simulated data.

shift and the SE which do not appear in the experimental spectrum. Regarding the ESA contributions, the most intense ESA in the experimental spectrum are present at frequencies $(39.10, 38.37)\,\mathtt{cm}^{-1}$, $(37.50, 36.69)\,\mathtt{cm}^{-1}$ and $(38.96, 36.76)\,\mathtt{cm}^{-1}$, and can be assigned to the respective frequencies in the simulated spectrum: $(40.2, 38.3)\,\mathtt{cm}^{-1}$, $(39.1, 36.5)\,\mathtt{cm}^{-1}$ and $(40.2, 36.6)\,\mathtt{cm}^{-1}$. Overall, there is a trend of approximately $1000\,\mathtt{cm}^{-1}$ blue-shift of the ESA signals between experimental and simulated spectra. All the non-assigned signals, both positive and negative, arise from interferences between the GSB (and its overtones) and the ESA. Nevertheless there is a qualitative and quantitative agreement in the theoretical approximations and experimental spectra.

The experimental and simulated TA results are supported by PE spectra, which hold a substantial wealth of information on molecular structure and dynamics of the excited states of pyrene. As an example, a cut along the vertical direction (fixed ω_t) in Fig. 5.9 is presented, respectively from the PE experimental and simulated spectra, which shows the extra information carried by such spectra. This is the opposite of the TA spectra, which are approximately the projection of PE along the vertical axes. In this particular example, the TA spectra did not show a separation of two peaks at 38 and $36.7\,\mathtt{kcm}^{-1}$. The assignment of the peaks to particular vibronical transitions involved into the photodynamics was done through the simulations and can be seen in Fig. 5.10. The main contributors to the spectra are the transition between the first vibronic level to the excited state, and the

	Experimental values		Simulation values	
	ω_t $[kcm^{-1}]$	ω_τ $[kcm^{-1}]$	ω_t $[kcm^{-1}]$	ω_τ $[kcm^{-1}]$
Positive peaks	36.68	36.65	35.9	36.7
	36.72	38.04	36.5	38.0
	38.16	37.97		
	38.14	37.02		
	37.43	35.84		
	37.08	35.46		
	39.34	36.06		
			35.9	38.0
			36.5	36.7
Negative peaks	39.10	38.37	40.2	38.3
	37.50	36.69	39.1	36.5
	36.01	36.57	40.2	36.6
	37.64	38.20		
	36.07	38.09		
	38.96	36.76		
	38.33	35.52		

Table 5.2: Positions of the peaks, experimental and theoretical values, extracted from the 2D plot at $T = 200 \, \mathtt{fs}$, expressed in $\mathtt{kcm^{-1}}$.
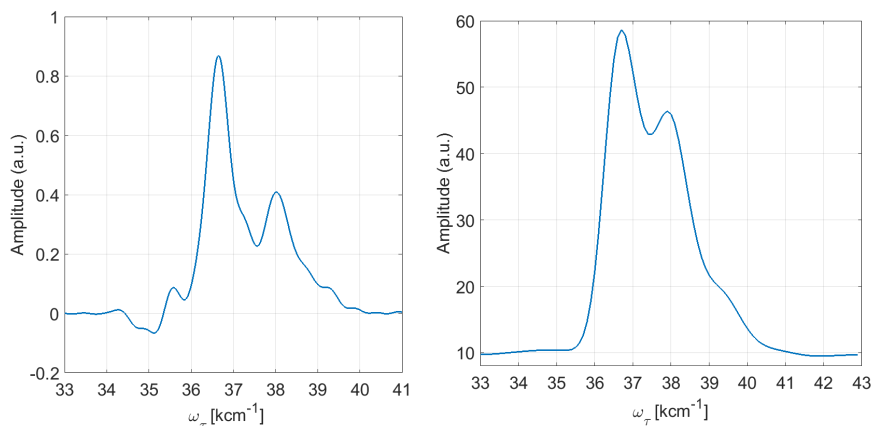
Figure 5.9: Vertical cut at fixed $\omega_t = 37\,\mathrm{kcm}^{-1}$ of the 2DPE spectra at $T = 200\,\mathrm{fs}$. Left: Experimental spectra, Right: simulated spectra.

ground state relaxation.

The main qualitative difference between the experimental and simulated PE spectra is the relative intensity of the blue band at the very right side of the spectrum ($\omega_t = 39\,\mathrm{kcm}^{-1}$). Here the upper peak has higher intensity than the lower peak in the experimental spectrum, whereas the opposite holds true in the simulated spectrum. To improve the general qualitative agreement to a more quantitative one, the system will be improved through the findings in the previous section.

The main advantage of this study's 2D spectroscopy set-up, the very short pulses, allows the dynamics of the peaks present in the PE spectra to be followed. The intensity fluctuations of those peaks can be extracted at different population times T, both from the experimental and simulated spectra, and plotted side by side as in Fig. 5.11. The frequencies of such oscillations, extracted through a two-dimensional Fourier transform, are comparable with the Raman frequencies of table 5.3, discussed in the next section.
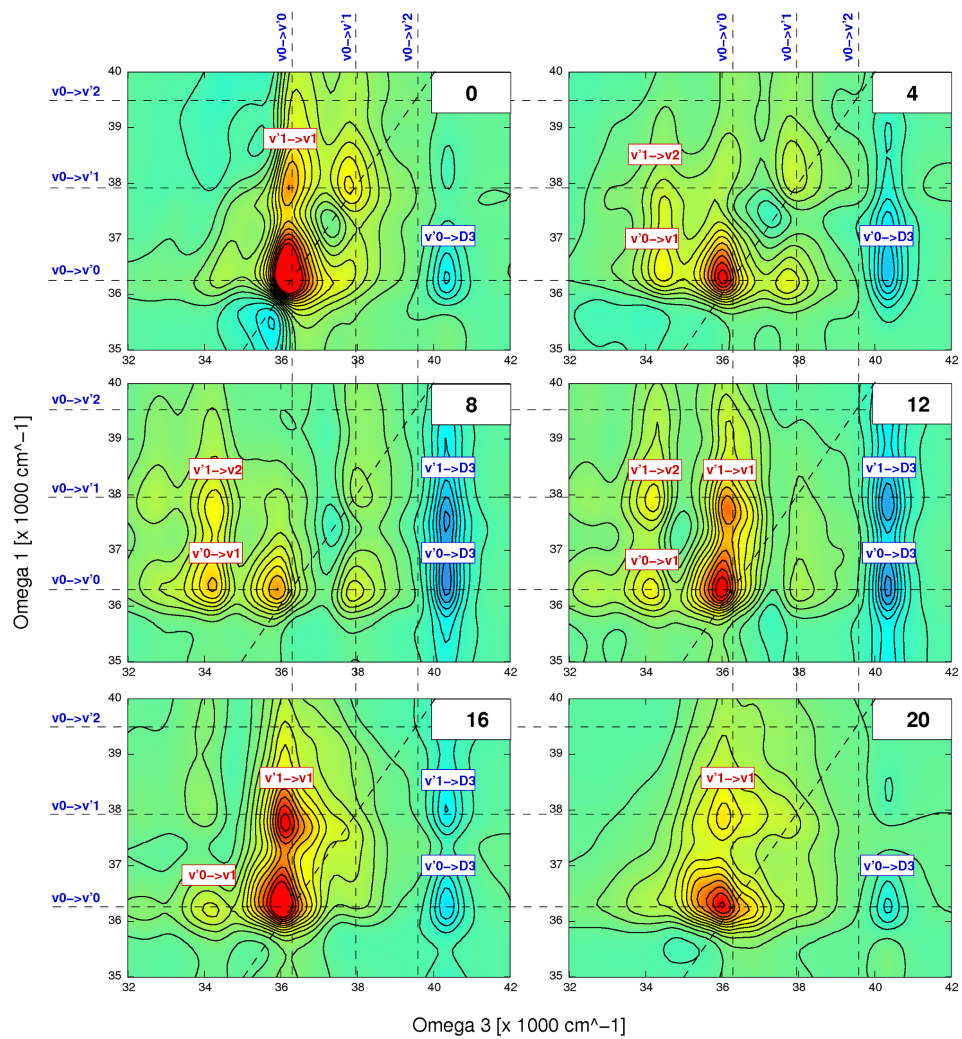
Figure 5.10: Assignment of the vibronical transitions from the simulated 2D spectra for the first 20 `fs`. The time delay T is reported in the white square on the top right corner of each 2D spectra.
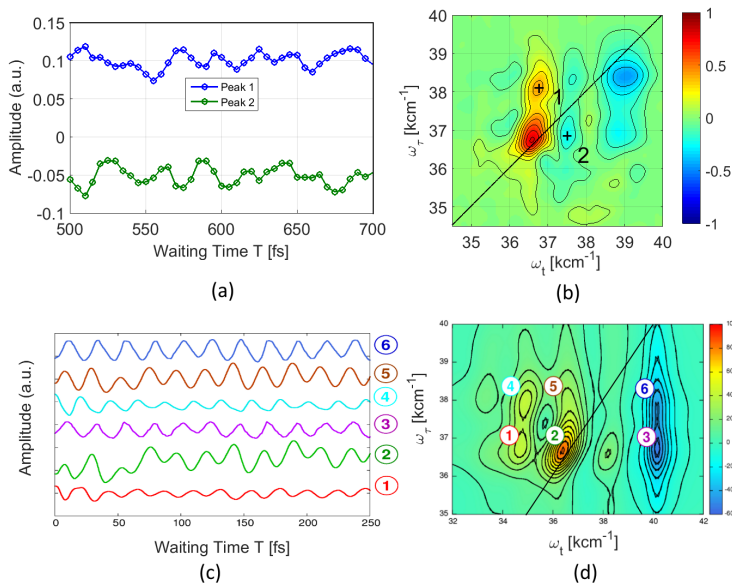
Figure 5.11: (a): Intensity fluctuations of the peaks present in the experimental 2DPE, labeled as in (c). (b): Intensity fluctuations of the peaks present in the simulated 2DPE, labeled as in (d).

5.6 Raman Oscillations

A coherent oscillation of the signals is observed in both the theoretical and the high-resolution ($5\,\texttt{fs}$) experimental spectrum in Fig. 5.12, with a period of roughly $20\,\texttt{fs}$, associated with the $1410\,\texttt{cm}^{-1}$ mode, and primarily contributing to the vibronic progression of the S_3 LA band. According to the simulations, the ESA band at $255\,\texttt{nm}$ contributes to the absorption of three bright electronic states absorbing between $245\,\texttt{nm}$ and $260\,\texttt{nm}$ and showing energy ($\sim 2000\,\texttt{cm}^{-1}$) and intensity (within 0.5 to $2.5\,\texttt{a.u.}$) oscillations due to the coherent dynamics in S_3. Fourier transformation of the $S_0 - S_3$ energy gap fluctuations along a short-time semi-classical adiabatic trajectory initiated at the FC point of the S_3 state allowed for the extraction of the main vibrational modes responsible for the observed vibronic progression in the LA spectrum of Fig. 5.3, the frequencies are reported in column MD, Table 5.3. The geometrical deformations are characterized by the computed normal modes and their frequencies in the ground state equilibrium. Moreover, they can be extracted within the DHO model by projecting the shift between the initial-state and final-state equilibrium structures on the set of normal modes (column GS, Table 5.3). From an experimental standpoint, one benefit of extremely short pulses is the direct resolution of this oscillatory behavior (Fig.
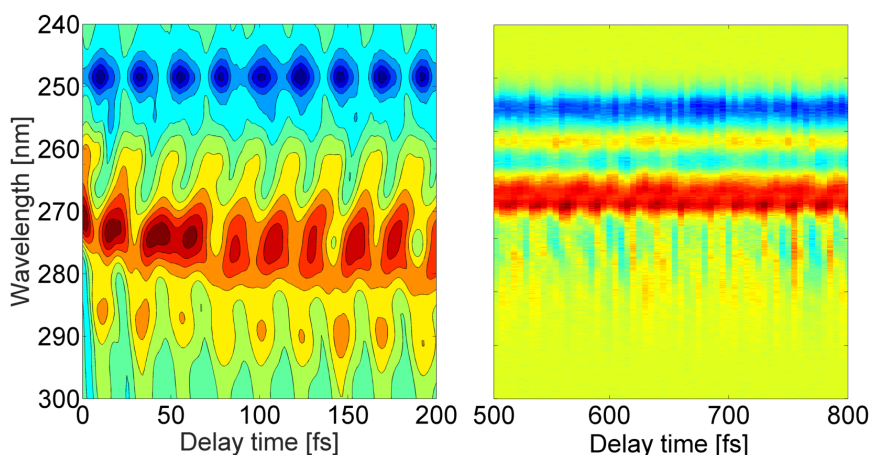
Figure 5.12: Pump-probe (TA) kinetics of pyrene in ethanol. Left - Simulated data for the first 250 `fs`. Right - Experimental data, 200 `fs` up to 500 `fs`. Colors are in counts/a.u.

A.10 in appendix). Fitting the decay of the TA or HTG, the subsequent subtraction of the resulting fits from the TA or HTG data set (the so-called residuals), and the following two-dimensional Fourier transform of such residuals provides the frequencies that lead to the oscillatory features. This is most notable in HTG where the signal to noise ratio is much higher. The Fourier transform given in Fig. 5.13 reveals a series of frequency components, with eight intense contributions listed in Fig. 5.3, (see column HTG). All the methods described above agree well with each other in the normal mode frequencies, and are comparable to Raman vibrations proposed in literature.

Resonance Raman spectroscopy has been previously utilized to identify the characteristic vibrations of the S_3 state of pyrene.[25] It is immediately evident that the frequencies reported by Jones et al.[25] and Shinohara et al.[24] agree very well with the frequencies obtained from our computations and experimental data. Table 5.3 compares the intensities of the bands obtained with non-resonance Raman in polycrystalline powder, and resonance Raman in acetonitrile (see Raman and Resonance Raman in Table 5.3). Notably, the same set of vibrations describes the GSB (265 nm and 270 nm) and ESA (255 nm) dynamics (except for the $2930\,\mathrm{cm}^{-1}$ mode which contributes only to the oscillations of the ESA), confirming the theoretical observation of similar normal mode frequencies at the GS and ES equilibrium geometries (columns GS and ES, Table 5.3. Furthermore, of note is the presence of a $888\,\mathrm{cm}^{-1}$ mode, which does not appear in Raman exper-

	simulation						experiment				type
	GS		ES	MD		HTG	Raman		Resonance Raman		
	ω	λ	ω	ω	λ	ω	ω	Intensity	ω	Intensity	
ν_1	403	0	403	427	34	390	407	0.33	408	0.40	breathing
ν_2	**579**	**2**	**571**	**549/610**	**131**	**570/587**	**592**	**0.26**	**574/592**	**0.50**	**breathing**
ν_3	-	-	-	-	-	888	-	-	-	-	
ν_4	1067	28	1038	1038/1099	47	1073	1066	0.18	1067	0.10	C-C stretch
ν_5	**1238**	**318**	**1238**	**1221/1282**	**127**	**1240**	**1241**	**1.00**	**1242**	**0.45**	**C-C stretch**
ν_6	1336	79	1334	1343	38	-	-	-	-	-	C-C stretch
ν_7	**1410**	**918**	**1409**	**1465**	**401**	**1408**	**1406**	**0.86**	**1408**	**1.00**	**C-C stretch**
ν_8	1585	141	1532	1526/1587	75	-	1550	0.09	1553	0.10	C-C stretch
ν_9	-	-	-	1592/1626	-	-	1594	0.64	1597	0.30	-
ν_{11}	3047	53	3058	-	-	2930	-	-	-	-	C-H stretch
ν_{10}	1678	27	1647	1709	39	-	1628	0.27	1632	0.30	C-C stretch

Table 5.3: Table with all the fundamental Raman modes registered in our simulated and experimental data, compared with literature values of pyrene crystalline powder[24] (Raman), and pyrene in acetonitrile[25] (Resonant Raman).
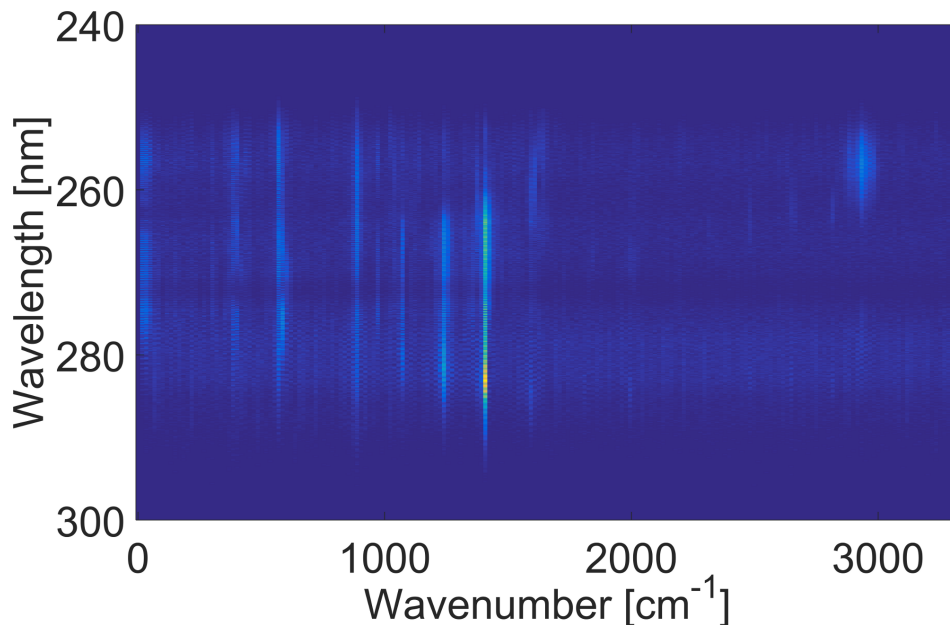
Figure 5.13: Fourier transform of the residuals of the experimental heterodyne transient grating spectrum.

iments. Thus far, its origin cannot be precisely pinpointed. Also of note is the $50\,\mathrm{cm}^{-1}$ blue-shift of the $1410\,\mathrm{cm}^{-1}$ vibration obtained from the quantum-classical simulation as compared to all other methods. This frequency is primarily responsible for the vibronic structure of the $S_0 \rightarrow S_3$ transition, associated with the symmetric carbon-carbon stretching at $1410\,\mathrm{cm}^{-1}$.

The $1594(1592/1626)\,\mathrm{cm}^{-1}$, i.e. the characteristic non-fully symmetric vibration of pyrene, is the only intense mode not appearing in the theoretical model. Depolarization ratios suggest the existence of the $1336\,\mathrm{cm}^{-1}$ mode, despite it appearing as a very weak band in Raman experiments and being covered by solvent bands in resonance Raman[25], thus justifying its absence from the HTG data. The $1242(1240)\,\mathrm{cm}^{-1}$ band is the most intense in non-resonance Raman and loses intensity in favor of the $1407(1408)\,\mathrm{cm}^{-1}$ band, as well as the low-frequency bands at $407(390)\,\mathrm{cm}^{-1}$ and $591(587)\,\mathrm{cm}^{-1}$ with an additional band at $574(570)\,\mathrm{cm}^{-1}$ appearing only in resonance Raman and our HTG experiments. The non-symmetric band at $1594(1592/1626)\,\mathrm{cm}^{-1}$ loses intensity as well, indicating that it is less important for the dynamics in S_3. The overall excellent agreement between the experimental and theoretical results indicates the sufficiency of the single trajectory treatment for reproducing the main dynamical features of pyrene. The three most important modes highlighted in

Table 5.3, show no frequency shift in the ES equilibrium (columns GS and ES, Table 5.3) as compared to GS equilibrium (thus justifying the DHO approximation). Furthermore, it is evident that the solvent has little effect on the ES dynamics and hence the spectroscopy of pyrene, as the experimental spectra (ethanol (this work), polycrystalline powder[24], acetonitrile[25] and benzene[24]) provide similar results which also agree well with the theoretical gas-phase computations.

The similarity between the vibronic structures of the S_3 and S_2 (essentially characterized through a HOMO→LUMO transition) bands in the LA spectrum is worth noting. Resonance Raman spectroscopy in S_2, as well as comparison to previously reported normal mode analysis and simulations of the near-UV LA spectrum of pyrene, reveals that the same high- and low-frequency modes $408\,\mathrm{cm}^{-1}$ and $1408\,\mathrm{cm}^{-1}$ are again responsible for the vibrational progression and band broadening.

5.7 Conclusions

This chapter presents a joint theoretical and experimental study of the dynamics of pyrene upon far UV excitation.

Firstly, two mechanisms of the de-excitation pathways of pyrene are proposed. Based on assumptions in the literature and the included experimental data, the conclusion is that excitation of the S_4 is followed by a sub-picosecond relaxation of the excited population to the phantom state S_3, then to the S_2 ($8\,\mathrm{ps}$) and finally to the S_1 states ($24\,\mathrm{ps}$). Ultimately, the population becomes trapped for an very extended time in the S_1/L_b bottle-neck minimum before relaxing to the ground state, and this time-scale is longer than the experimentally allowed time-scale maximum ($200\,\mathrm{ps}$). This mechanism not supported by the present calculations that show only one conical intersection between S_3 and L_b, which assumes characteristics of S_1 at the minimum. Alternatively, the fluorescence structure at $350 - 368\,\mathrm{nm}$, previously associated with S_2, is instead a relaxation from the L_b immediately after the CI with the phantom state, and the S_2 level is fully uninvolved in the de-excitation dynamics.

The experimental PE spectra are in qualitative agreement with the simulated spectra, with a few exceptions. The findings of the simulations are that the main transitions contributing to the PE spectra are vibronic transitions and ground state relaxations. As the agreement is not perfect, it is necessary to transition to increasingly refined simula-

tions based on the most recent aforementioned dynamic simulations.

An incidental finding of the experimental setup is the possibility of investigating Raman frequencies of pyrene. The simulated and experimental Raman agree well with the values from the literature. The majority of the Raman transitions do not have an appreciable shift between the ground state frequency and the excited state frequency, thus it is difficult to discern the origin of the experimental values, meaning whether the Raman frequencies are of the ground state or excited state vibrations. All frequencies in this study have been already assigned in the literature to either breathing of the aromatic rings, or C-C and C-H stretches.

Chapter 6

2D Photon echo, transient grating and transient absorption spectroscopy of nucleobases and analogs

The following chapter presents and discusses the time resolved experimental spectra of various nucleic acid molecules solvated in an aqueous environment. The chapter begins with transient absorption (pump-probe) spectra (TA), and analyzes them using global fitting (see Ch. 6.3). In the second part of the chapter, TA, heterodyne transient grating (HTG) and photon echo (2DPE) spectra of nucleic acids are analyzed and discussed. Part of the material in this chapter has been adapted from a published paper *V. I. Prokhorenko, A. Picchiotti et al., J. Phys. Chem. Lett. 4445–4450 (2016)*[28] of which the author of this study is an author, with permission from applicable sources.

6.1   Introduction

The photodynamics of nucleobases are a long-standing question in the chemical physics community. For example, from an evolutionary perspective the survival of these molecules during the UV bombardment of the pre-biotic world is a mystery. The exact mechanisms remain relatively unknown, mostly due to limitations of the technique until recently, when femtosecond lasers and higher computation power became available to scientists in the community. Relevant questions include whether and how solvent is involved in the release of excess

energy, and how different solvents interacted with nucleobases. Moreover, the potential differences between nucleobases, and conversely, the possible existence of an universal mechanism are questioned. These questions are answered based on the presented data, although they are limited to the "natural" nucleic acids (thymine, guanine, adenine, and cytosine) and some "natural" modifications (presence of a sugar ribose and phosphate groups), meaning they mimic the molecules present in unmodified *DNA*.

Several groups have already reported a number of femtosecond time resolved spectra on nucleobases, using various techniques: transient absorption[6,13,15,16,37–45], time-resolved fluorescence[6,44,46–48], and photoelectron spectroscopy.[49–52] The novel aspect of this work is that the optical setup allows for the full coverage of almost all of the lowest absorption band and excited-state emission band of nucleobases (250 to 300 nm). Moreover, such a broad band spectral window and the short pulse ($6-8\,\mathtt{fs}$ in fwhm) permits the recording of the very short dynamics, including oscillatory behaviors connected to Raman frequencies. With these experimental capabilities, it is possible to refine the mechanism of the photo-deactivation upon UV excitation in nucleic acids, and an universal, unifying scenario is proposed, described in the Conclusion of this chapter.

6.2 Sample preparation and detection conditions

Adenine, adenosine, cytosine, and thymine were all purchased in powder form from Sigma Aldrich (guanine and guanosine from Santa Cruz) with at least 98% purity. dATP was purchased from JenaBiosience with purity greater than 95%. All the samples (except dATP) were dissolved in distilled desalted water in glass vials (clean room quality from Carl Roth); for dATP a phosphate buffer with strength of $10\,\mathtt{mM}$ was used (see Ch.2.2). The solutions were stirred with a glass-covered magnet for approximately 30 minutes at room temperature and then sonicated. The solubility of guanine in water is insufficient for achieving the necessary concentration and therefore we substituted guanine with guanosine.

The solute concentrations were adjusted such that the maximum absorbance, at the maximum of absorption near 260 nm, was between

0.25 and 0.35.

The filtration of the samples was initially performed with a pre-filter ($0.2\,\mu$m mixed cellulose ester membrane DynaGard) by hand, and afterwards using a syringe pump (Aladdin 300- 220Z syringe pump from WPI) in a $5\,$mL syringe, at a speed of $0.5\,$mL/min. The filters used are, in order of use: $0.2\,\mu$m regenerated cellulose membrane (Chromacol) and $0.1\,\mu$m Acrodisc supor sterile membrane (Pall Life). Before usage, the final solutions were stored in a fridge at $5°C$. The absorption spectra were measured using a UV2600 spectrophotometer (Shimadzu) in a $1\,$mm or $0.1\,$mm quartz cell (Hellma or Starna), and additionally controlled *in situ* by measuring the transmission with a UV-sensitive photo-diode 2032 (Newport). After each set of measurements, the absorption spectrum and the pH of the samples were checked to ensure the sample did not have any photo-damage. The OD of all the samples was maintained at $0.25 - 0.35$ at maximum absorbance, and the pH was kept at ≈ 7. In order to minimize light scattering and pulse broadening, the solutions were circulated through a home-built wire-guided jet with the thickness in excited volume maintained at $\approx 250\,\mu$m (see Ch. 3). The excitation spot size was $\approx 50\,\mu$m and, with the jet pump speed used ($3000 - 3500\,$rpm), a refreshment of excitation volume was guaranteed for the laser repetition rate ($1\,$kHz). The UV-pulses excitation energies were $15 - 20\,$nJ per beam.

The frequency-resolved 2DPE signals were collected with a scan range of $128\,$fs and a step of $1\,$fs at fixed waiting times T. At each delay point 900 to 1800 single spectra were averaged to achieve high SNR. Each photon echo scan took approximately 2 to 10 minutes per one delay point T . The pump-probe spectra were typically collected in a delay range of $5 - 10\,$ps with a step of $10 - 20\,$fs; each delay point is the result of averaging 3600 (in the case of very small signal, this value is doubled) differential spectra (pump-on / pump-off). In order to resolve the long-lived decay times, the delay scans were performed in a $100\,$ps window with unequally-distributed steps. In the present chapter, the differential spectra are plotted as measured, without normalization of the probe spectra. In order to achieve the high spectral resolution needed for resolving the oscillations, the delay step was set to $4 - 5\,$fs in HTG measurements and the associated TA measurements (performed for phasing). PE spectra were always collected concurrently with a TA spectrum at the same population time T, and the PE spectra were individually phased with their cor-

responding TA spectrum (at the same T). TA spectra were fit with a multi-exponential model using an home-written software based on global fitting analysis.[166] Fitting of the experimental data was performed through multiple home-written programs within the Matlab shell. For a rationale regarding the global analysis fitting of pump-probe data, see Ch. 6.3.

The 2D spectra were created following the method described in Ref.[164]; the corresponding pump-probe spectra, measured at the same waiting times T, were used for their phasing. Although the phasing procedure used is described in detail in Ref.[164], due to a large spectral window in reported 2DES experiments it was necessary to account for a wavelength dependence of the LO-filter refraction index. The 2D spectra were then transformed to the time domain, filtered with a Gaussian-shaped kernel, and transformed back to the frequency domain. The filtering lowers the resolution in 2D spectra to approximately $200 \, \text{cm}^{-1}$.

6.3 Determination of the number of components in the fitting procedure of TA spectra: a study case

Global fitting was used as the statistical tool for extracting the number of populations participating in the de-excitation dynamics and their lifetimes. The software used was written within the Matlab shell environment by Valentyn I. Prokhorenko and used as a "black box". The mathematics behind the fitting is described in Ref.[166]. This section lays out the rationale behind the choice of the number of components (populations) and other influential parameters on the resulted fitting, such as setting one of the components to be infinitely long, the filtering of noise, and the starting point (time) of fitting. This is shown by giving examples of fit and using a real experimental data set, performed on adenine dissolved in water; the already filtered data used in this section are shown in Fig. 6.1.
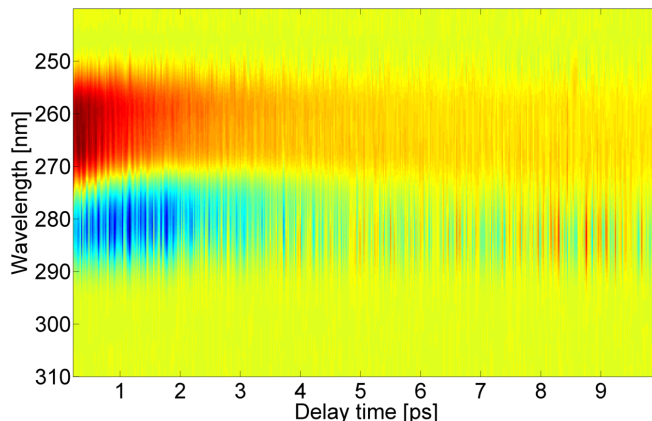
Figure 6.1: TA spectra of adenine dissolved in water, after noise reduction.

Firstly, the determination of the number of components is examined. This is equivalent to the choice of the number of exponentials fitting the data, with the temporary assumption that the starting fitting time is $0.2\,\mathrm{ps}$. The number of components is a difficult choice, as more exponentials in the fitting procedure give better fitting results due to the higher number of free parameters, but this leads to artifacts (the introduction of non-realistic non-physical components). The optimal choice is to have the *minimum* set of parameters (the minimum number of exponentials) that give a reasonably good fit. For example, the spectra compared in Fig. 6.2 show the residual after fitting the data in Fig. 6.2 with two, three and four exponentials. The 2D plots of the residuals show some non-randomness in the noise, although at first glance this might not appear qualitatively different. One can see in the residuals of the two-component fitting that one area is more light blue than the rest, between $255\,\mathrm{nm}$ and $280\,\mathrm{nm}$ and after approximately $6\,\mathrm{ps}$. It is more evident if one observes the spectrum at just one wavelength ($260\,\mathrm{nm}$ in Fig. 6.3), that there is some kind of structure (a wavelike behavior) in the case of two components, but this disappears with three components. One necessary step is to have a look at the single components in order to determine if they have been fitted properly, as in Fig. 6.4. Here the decay trace at $260\,\mathrm{nm}$ is presented, and its resulting fit with two, three and four exponentials; it is clear that three components is the minimum number necessary for obtaining a good fit. By a sufficient random pick of decay traces one can decide what is a good fit at all wavelengths. Finally, the standard deviation does not improve by moving from three components

116

(2.97 `cnts`) to four components (the same value) fitting, Tab. 6.1.

N. exp.	STD cnts	lifetime value ps	interval of confidence ps
1	3.6	2.74	0.01
2	3.33	0.33	0.01
		2.57	0.01
3	2.97	0.75	0.03
		1.49	0.04
		38.22	8.99
4	2.97	0.50	0.03
		1.32	0.14
		2.57	0.28
		13.20	4.08

Table 6.1: Lifetime values, their confidence interval (calculated at $\pm 95\%$), and the standard deviation (STD) from fitting procedures with different number of components (N. exp.).

Another aspect to consider is the actual lifetime values and their error, given that the number of experimental data points is sufficient to have proper statistics (in the hundreds or thousands). It should be assumed that it is statistically possible to distinguish the lifetimes and that their intervals do not overlap. When overlap exists and is substantial, "over-fitting" occurs, meaning that too many components (exponentials) are used in the fitting routine. Another symptom of over-fitting is the presence of components that have very similar values and a DAS symmetrical to each other, one with negative sign and one with positive, and with unrealistic magnitudes in dT, such as in Fig. 6.5.

A different configuration may be used, where the starting delay time of fitting is changed using three-exponential fitting. This problem arises from the very significant solvent contribution at very fast delay times (< 150 `fs`), that gives an in-erasable artifact (Fig. 6.6). In table 6.2 a list of lifetimes with respective confidence intervals is given, while the longer lifetimes do not substantially change, the shorter ones are particularly influenced by the choice of the starting point. As not all the experiments have similar signal to noise ratios, due to day-to-day
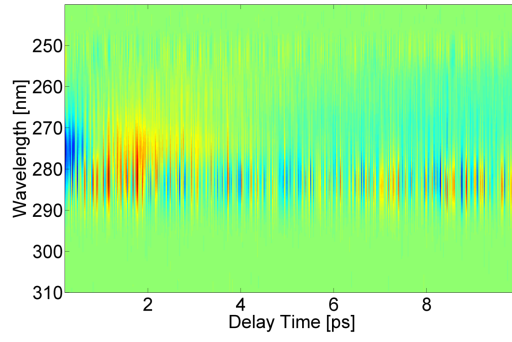
(a) 1 exponential
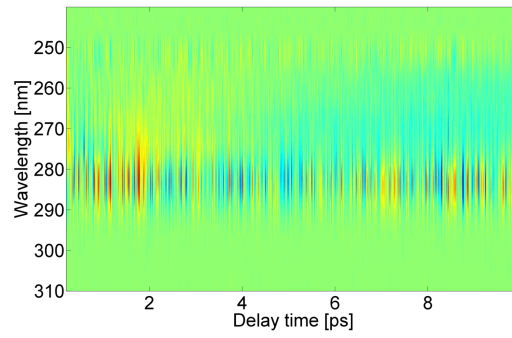
(b) 2 exponentials
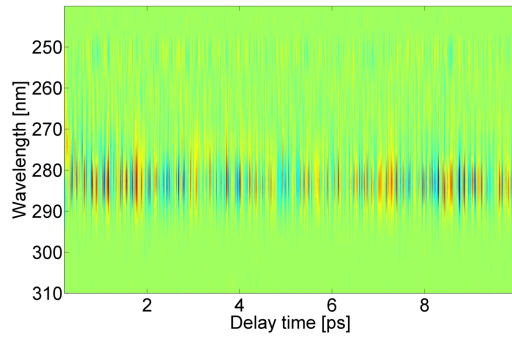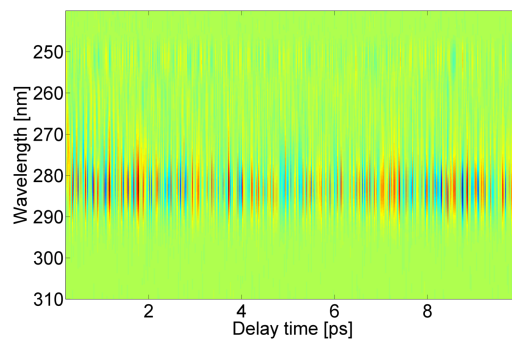
(c) 3 exponentials

(d) 4 exponentials

Figure 6.2: Comparison of residuals obtained from global fitting applied to the spectra in Fig. 6.1, using one, two, three and four exponential components.
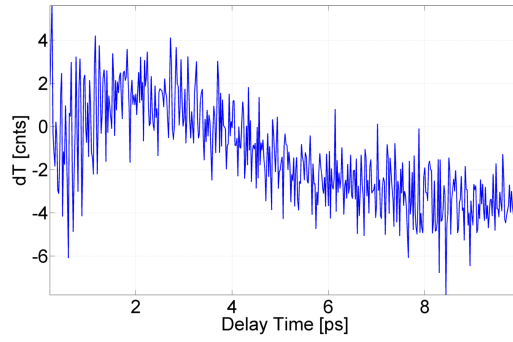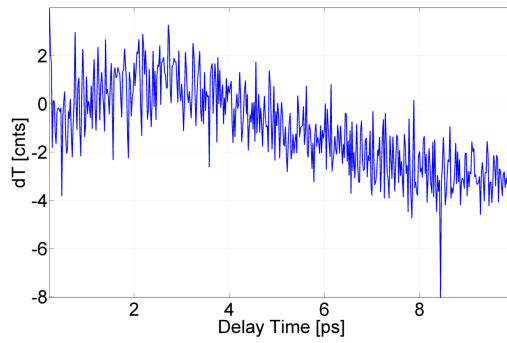
(a) 1 exponential
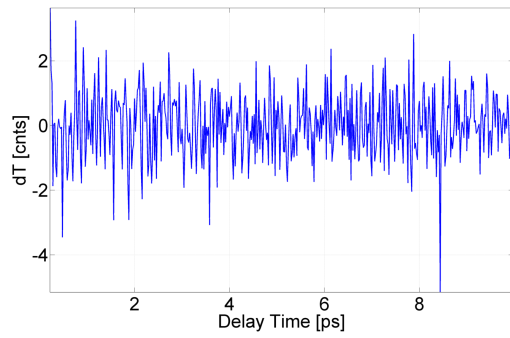
(b) 2 exponentials
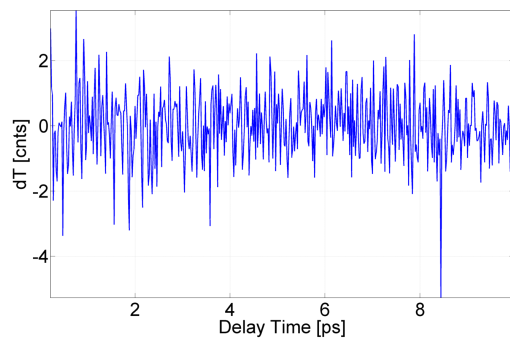
(c) 3 exponentials

(d) 4 exponentials

Figure 6.3: Comparison of residuals obtained from global fitting applied to the spectra in Fig. 6.1 at $260\,\mathrm{nm}$, using one, two, three and four exponential components.
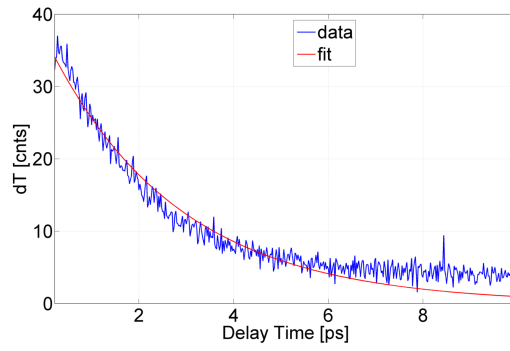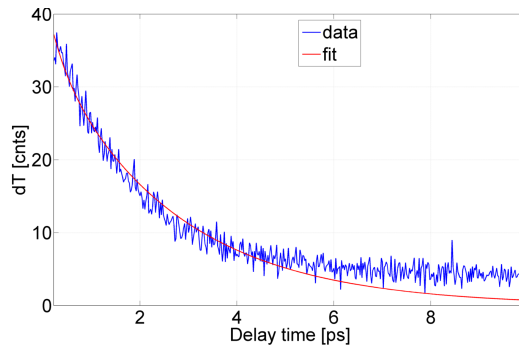
(a) 1 exponential
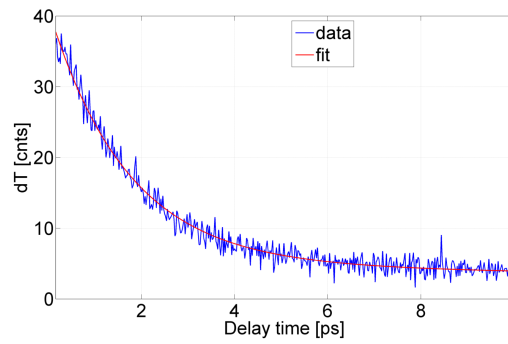
(b) 2 exponentials
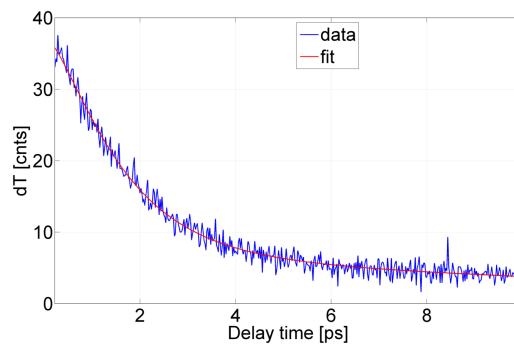
(c) 3 exponentials

(d) 4 exponentials

Figure 6.4: Comparison of decay traces at $\approx 260\,\mathrm{nm}$ and its fitted values, obtained from global fitting applied to the spectra in Fig. 6.1, using one, two, three and four exponential components.
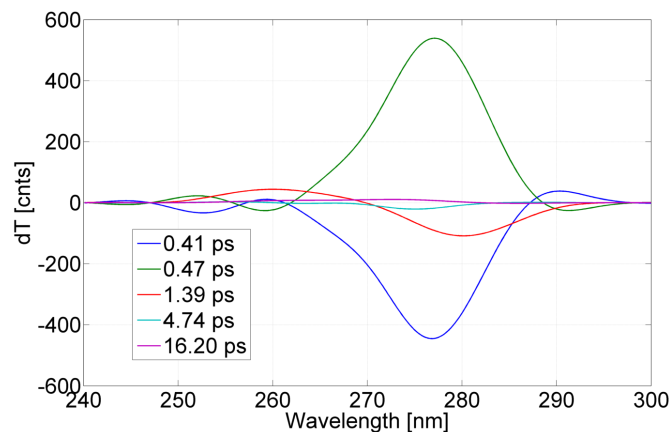
Figure 6.5: Decay associated spectra (DAS) obtained fitting the experimental data in Fig. 6.1 with global analysis with five components, showing the unrealistically high magnitudes of dT of the green and blue curves, respectively for the very near in value lifetimes $0.41\,\mathrm{ps}$ and $0.47\,\mathrm{ps}$.

influences on laser, jet, and sample filtering performance, all the data in the present work are analyzed from $200\,\mathrm{nm}$ onward, in order to have a common ground for comparison.
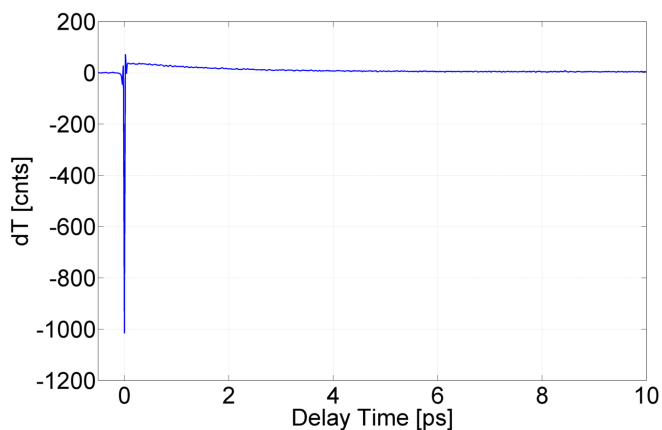
Figure 6.6: Example of decay trace at $260\,\mathrm{nm}$ showing the extreme contribution from solvent at delay time near zero.

Delay Time ps	lifetime value ps	interval of confidence ps
	0.48	0.01
0.10	1.90	0.02
	38.42	9.52
	0.59	0.01
0.15	1.67	0.03
	38.34	8.94
	0.75	0.03
0.20	1.48	0.04
	38.22	8.99

Table 6.2: Lifetimes value, their confidence interval (calculated at $\pm 95\%$) from fitting procedures with three components at different starting delay time of fitting.

Finally, a remark on the longest lifetime, which is not included in the presented modeling of nucleobases. As discussed, the final and best fitting is given by employing three exponentials and starting from a 200 ps delay time. The decay associated spectrum for the longest lifetime is 6 cnts at its maximum, and the standard deviation results in 2.97 cnts, counting for almost 50%. However, a conservative approach would not assign this lifetime. Moreover, its value is biased by the window of data acquisition, in this case 10 ps; a safer choice, often applied in the analyses in this work, is to set such a lifetime as infinitely long, assuming that it is much longer than the maximum delay time registered.

6.4 Transient absorption spectroscopy on nucleic acids: adenine, thymine, cytosine and guanosine compared

This section presents and compares the experimental results conducted on nucleosides, nucleotides and deoxy-nucleotides (see Ch. 1.5 for explanation on terminology). In particular, adenine, adenosine, dATP,

guanosine, thymine and cytosine were investigated, showing no appreciable difference in the TA kinetics and PE spectra. Due to the low solubility of guanine in water, it was not possible to acquire data on this nucleoside.
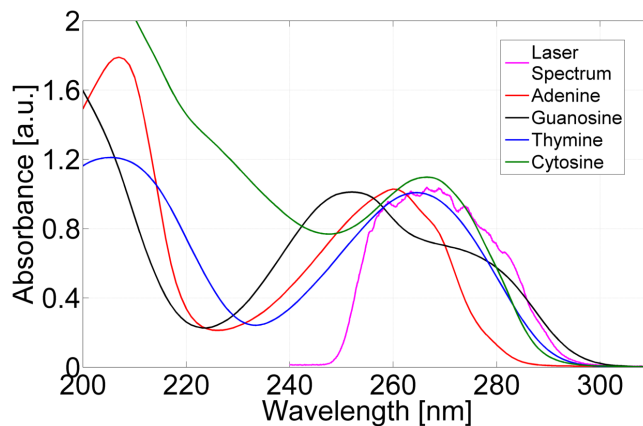
Figure 6.7: Linear spectra of the natural nucleic acids investigated: adenine (red), guanosine (black), thymine (blue) and cytosine (green), all dissolved in water, overlapped with the laser spectrum output from our setup in pink.

TA and PE studies of the four natural nucleic acids were performed in the $250-300\,\mathrm{nm}$ window, which covers their lowest absorption band and excited-state emission band (Fig. 6.7, where the absorption spectrum of the nucleic acids overlaps with the laser spectrum of the setup in our laboratory). Due to the broadband laser pulse, most of the absorption peak is covered, resulting in an good access to all the bright states.

The TA data show similar kinetics, and using global fitting also showed similar lifetimes (summarized in Tab. 6.3) of the populations involved. Fig. 6.8 summarizes these findings, with on the left the TA spectra in differential transmission dT, with their red and blue bands in opposite sign. The red bands can be associated to excited state absorption (ESA) buildup, recovery of ground state bleaching (GSB), and stimulated emission (SE) decay. Vice-versa, the blue bands are usually generated by a decay in the ESA and a building up of SE and GSB.

Following the presented data, one may notice the presence of two very distinct bands with opposite sign in the TA spectra, and the remarkable difference in the kinetics of those two bands, whose two illustrative cuts at $260\,\mathrm{nm}$ and $280\,\mathrm{nm}$ are shown in Fig. 6.9. Mean-
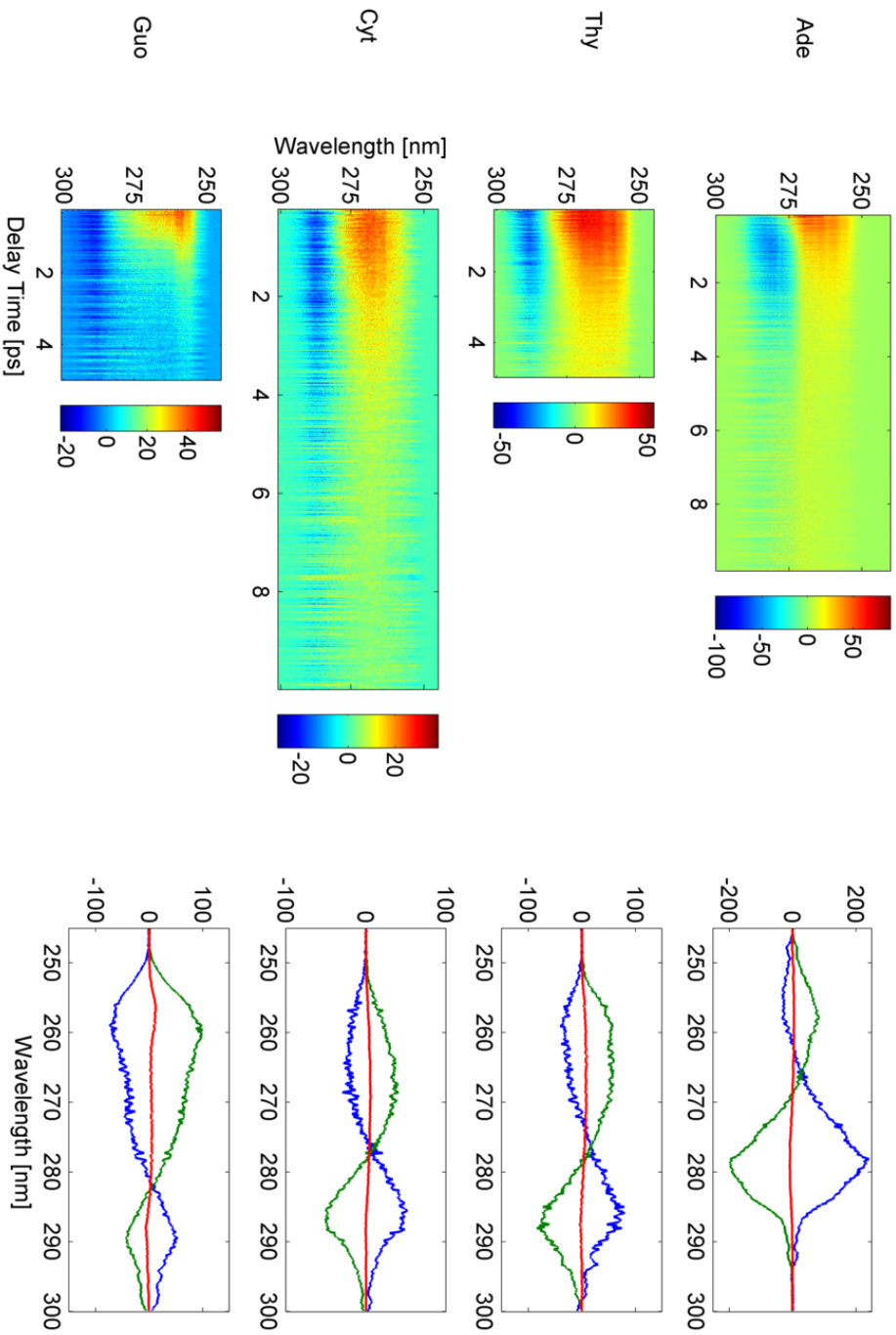
Figure 6.8: Summary of the pump-probe spectra (left) and their decay associated spectra (right) of the four nucleic acid investigated.

124
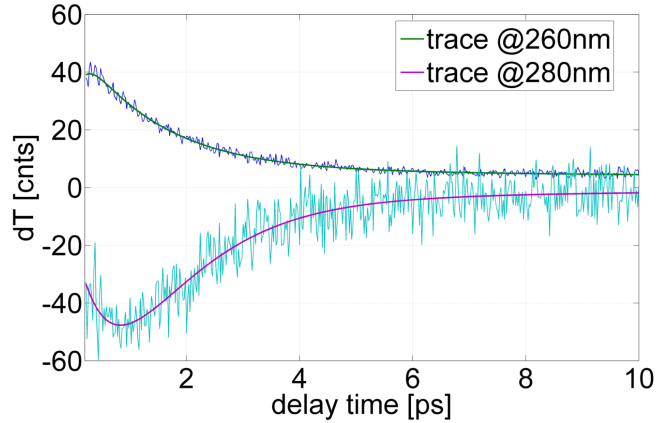
Figure 6.9: A cut from the TA spectra of Fig. 6.1 at two different wavelengths: 260 nm and 280 nm.

Nucleic acid	fast [ps]	intermediate [ps]	slow [ps]
Ade	0.75	1.51	38.2
dATP	0.7	1.31	8.6
Thy	0.63	1.74	54
Cyt	0.75	1.8	48.3
Guo	0.5	0.9	5.2

Table 6.3: Values of the three components (slow, intermediate and fast) for the four natural nucleic acids investigated. Uncertainties of fast and medium lifetimes are $\approx 5\%$, and those of slow are $\approx 10\%$.

while on the red lobe, at the shorter wavelengths where the maximum of the linear absorption spectrum is located, the excited electronic population decays relatively slowly. First there is a fast GSB and SE of the population at longer wavelengths, followed by a slower recovery to zero values of differential transmission (dT), when the ground state population is fully recovered, emptying all the other excited states. Furthermore, the dT at the blue band at longer wavelengths is negative due to ESA.

The decay associated spectra (DAS) retrieved from the TA spectra using global fitting (see Sec. 6.3) show three major components (Fig. 6.8, right). Interestingly, the TA spectra of all the four natural bases investigated in the laboratory are characterized by three lifetimes: fast, intermediate and slow, with values presented in Tab. 6.3. Opposite signs and a butterfly-like shape characterize the DAS at the two opposite spectral edges of the spectra. Following the result of the global fitting, it is apparent that at least three states are
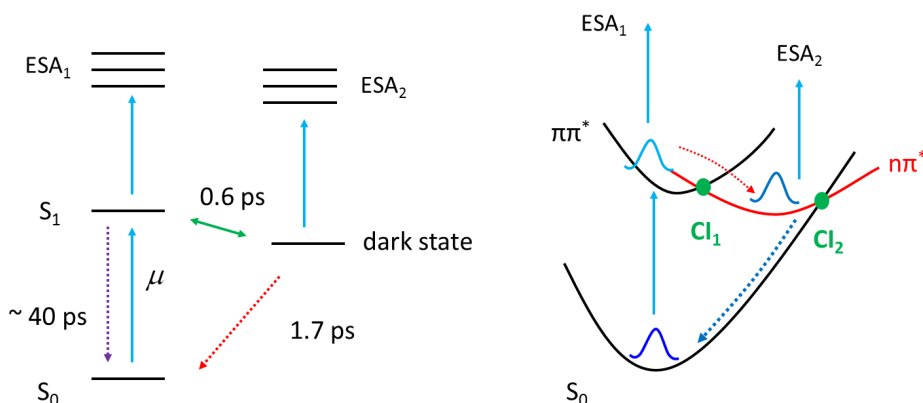
Figure 6.10: Phenomenological spectral model describing the transient absorption (TA) kinetics.

involved in the deactivation pathway, since there is a rapid transfer of population between two distinct excited states, caused by a type of intra-molecular energy (or possibly charge) transfer.

The growth of the signal at around $280\,\mathrm{nm}$ can be connected to a growth of the population in the dark state, which is not directly accessible from the ground state, but observable through the ESA. The observed population kinetics can be summarized as a phenomenological spectroscopic model, represented in Figure 6.10 as a Jablonski diagram. The key feature is the ESA channel from the dark state. Without ESA from the bright $\pi\pi^*$ state, it is not possible to explain the butterfly-like shapes of DAS. This simple spectroscopic model reproduces measured TA kinetics and DAS shapes (see Figure 3S in the Supporting Information of reference[28]).

The slowly decaying channel is not included in this model due to its insignificant contribution to the population kinetics, (see DAS in Fig. 6.8). It is unclear what process leads to this long-lived transient. It may originate from the tautomers present in the solution due to decay in an underlying and weakly populated electronic state that is not connected to the dark state (e.g., L_b or L_a states, depending on the spectral location). It may also be due to a weakly populated triplet state, as proposed for pyrimidines.[6,34,198] However, this slow transient is common to all investigated compounds that can be associated with cooling of the ground state, which undergoes heating due to excess energy released after the relaxation of the population from the dark state.[199,200] Pecourt et al.[53] attribute this cooling of the

hot ground electronic state to the medium component in TA kinetics $(0.9 - 1.8\,\text{ps}$, Tab. 6.3). However, the cooling of a solute presents nontrivial temporal behavior that is irreducible to a simple exponential function (see equation 10 in Hirakawa et al.[201]). Furthermore, the strength of the electronic oscillator is temperature-independent, thus conserving the area of the absorption spectrum. Therefore, cooling the solute ought to greatly increase the magnitude of the absorption peak position compared to the red side in the corresponding DAS. Femtosecond TA spectroscopy has demonstrated this effect for the TIN chromophore.[199] The experimental DAS of the medium relaxation times either show the opposite as compared to the TIN chromophore case (Fig. 6.8) or that DAS magnitudes at these wavelengths are similar excepting guanosine, which presents two well-resolved electronics transitions in the laser spectrum. As it is not possible to exclude that cooling affects these dynamics, this work rather refers to the dominant processes in excited-state relaxation.

6.5   Raman frequencies from the TA spectra of nucleobases

Extremely short pulses allow for the direct resolution of the fine oscillatory structure visible in the TA in Fig. 6.8. However, the resolution of this structure is significantly better in heterodyne transient grating measurements due to a higher signal-to-noise ratio. For all nucleobases, two long-lasting oscillations with similar frequencies are detected in the entire spectral range of the probe (Tab. 6.4 and Fig. 6.11). For adenine, these frequencies of $1340\,\text{cm}^{-1}$ and $1494\,\text{cm}^{-1}$ can be respectively associated with Raman modes corresponding to the stretching modes of a six-member ring (b2u) and (e1u).[201] The lowest two frequencies of thymine correspond well to recent ones in Xue et al.[45] It should be noted that no evidence regarding the reported $317\,\text{cm}^{-1}$ oscillation was found in the experimental data presented here.
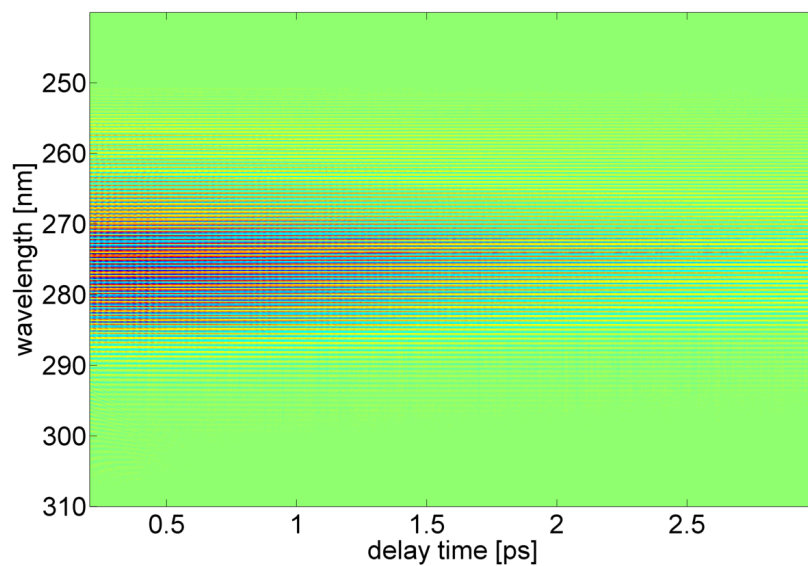
(a)
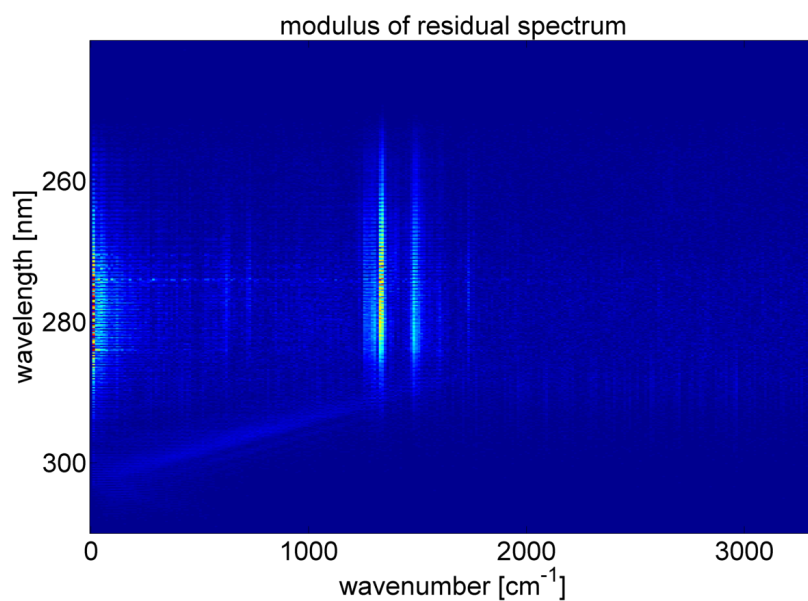
(b)

Figure 6.11: Long-lasting oscillations in heterodyne transient grating (HTG) for adenine in water (a) and the Fourier transform of the residuals (b). Two intense oscillations at 1340 and 1494 cm^{-1} are clearly resolved.

Compound	Resolved frequencies cm^{-1}	Resolution $\pm\,cm^{-1}$
Ade	1340	6
	1494	
dATP	1348	17
	1482	
	1583	
Thy	1247	17
	1380	
	1685	
Cyt	790	28
	1300	
	1526	
Guo	1300	28
	1526	

Table 6.4: Frequencies of the oscillations retrieved through Fourier transform from the residuals of the HTG data of nucleic acids. The resolution is limited by the scan ranges of the HTG data.

Two different Raman spectra were collected in order to confirm the Raman shifts listed in Table 6.4. These spectra were acquired by exciting solutions of adenine and thymine in water in the order of tens of millimolar at $260\,nm$. The spectra are presented in Fig. 6.12. The Raman shift peaks of adenine and thymine were reproduced. The frequencies detected with heterodyne transient grating spectroscopy correspond to the highest intensity Raman peaks within the experimental error. As the Raman spectra in Fig. 6.12 detect the ground state Raman frequencies, the frequencies detected with HTG are from the ground state. Alternatively, the Raman frequencies for the excited state are shifted from the ground state less than the experimental error ($6\,cm^{-1}$ for adenine and $17\,cm^{-1}$ for thymine).
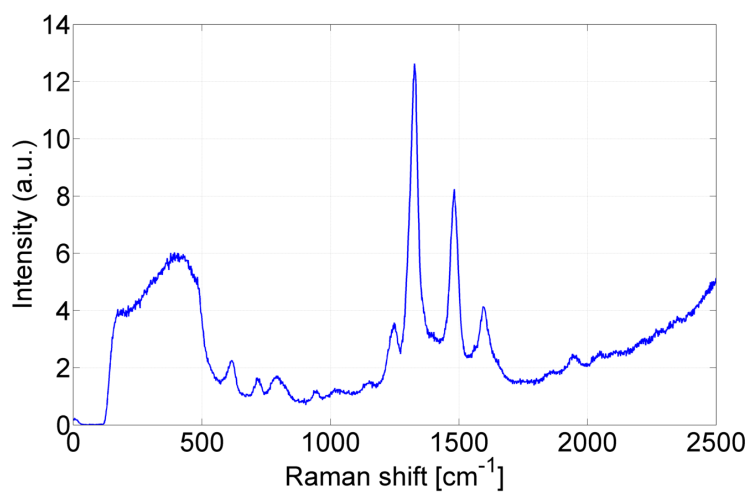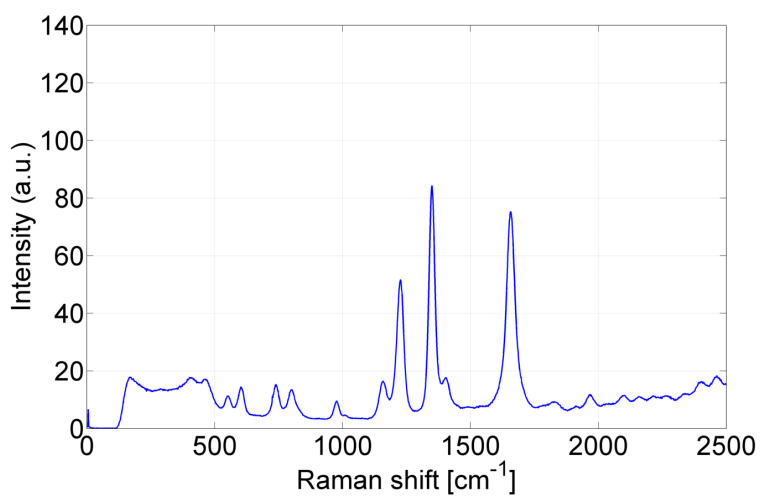
Figure 6.12: Raman spectrum of Adenine (a) and Thymine (b) dissolved in water, excited at 260 nm. Courtesy of Florian Biebl.

6.6 2D photon echo spectroscopy of nucle-obases

The PE experiments were performed in the same spectral window, and the results fully support the findings of the TA experiments. Two lobes in the 2D spectra with opposing signs along ν_t can be expected, as the projection of a 2D spectrum on an "observation" axis ν_t results in a pump-probe spectrum. This remarkable feature is present in the experimental 2D spectra of all investigated nucleobases (Fig.6.13) and can be considered the unique "marker" of a dark electronic state.
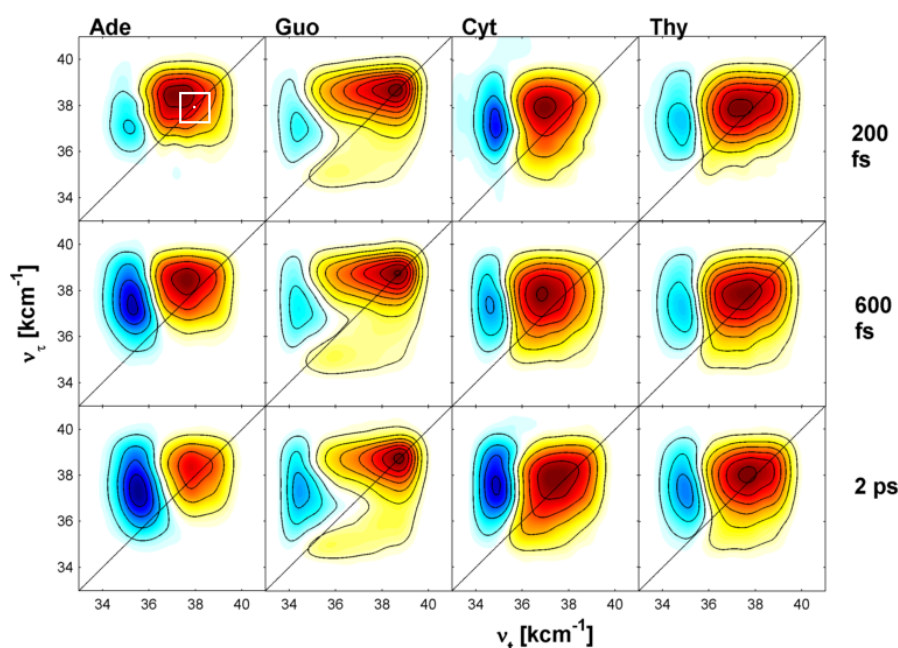
Figure 6.13: real part of PE spectra of investigated DNA nucleobases for selected waiting times as indicated. The contour steps are in 10% magnitudes; each spectrum is normalized to its maximum. The white square indicates a spectral bandwidth realized in ref[33].

It should be noted that in recent PE studies of adenine[33,34] the realized spectral bandwidth was approximately six to twelve times smaller (a few nm), which significantly restricts the observation capabilities of photo-deactivation dynamics, and therefore these two peaks were not resolved. The above-mentioned oscillations are also well-resolved in a series of 2D spectra taken with a small waiting time step. Figure 6.14 shows an example of the remarkable magnitudes of the oscillations in adenine at $\nu_t = 37410\,\mathrm{cm}^-1$ and $\nu_\tau = 36010\,\mathrm{cm}^-1$. Of note is the
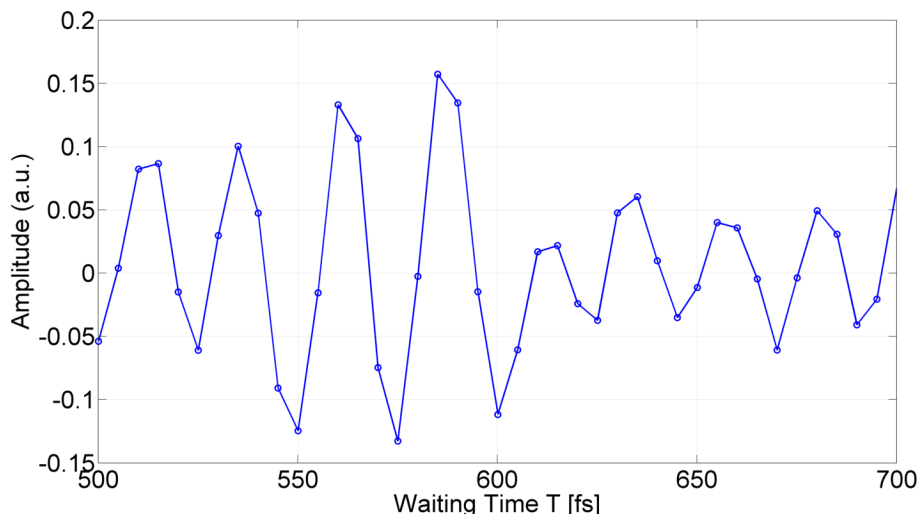
Figure 6.14: Oscillations observed in 2D spectra of Ade at $\omega_t = 37.94\,\mathrm{kcm}^{-1}$ and $\omega_\tau = 36.51\,\mathrm{kcm}^{-1}$.

high variance in the phase relations between oscillations across the 2D spectrum.

The information acquired from PE is richer than from TA spectroscopy. The two lobes in the 2D spectra of adenine are noticeably tilted to the diagonal, whereas they are parallel in cytosine and thymine. Though adenine and guanosine are both purines, the shape of their spectra are noticeably different. The 2D spectra of guanosine present two clearly resolved diagonal peaks and a cross-peak located at around $\nu_\tau = 36000\,\mathrm{cm}^{-1}$, $\nu_t = 38000\,\mathrm{cm}^{-1}$, reflecting the presence of two electronic transitions at the same ground state, and thus leading to a cross-peak. This is also present in the absorption spectrum of guanosine. This low-lying positive diagonal peak shields the contribution of the negative peak to the pump-probe spectrum, thus decreasing the negative amplitudes in TA of guanosine at the red side (Fig. 6.8). Furthermore, these 2D spectra show that in guanosine, population transfer to the dark state flows from the above-located bright electronic state. No pronounced inhomogeneous broadening or elongation along the diagonals in the 2D spectra is detected. The off-diagonal width of 2D spectra is proportional to the magnitude of homogeneous broadening, which in this case is significant, $(\approx 3000\,\mathrm{cm}^{-1})$ for the spectra of all nucleic acids. Thus, the associated electronic dephasing time is very short, $(6 - 8\,\mathrm{fs})$ depending on the nucleic acid). Therefore, the system-bath interaction in these compounds is very strong.

6.7 Conclusions

Summarizing the experimental observations and findings presented here, it is possible to conclude that an universal mechanism of photo-deactivation that is equally valid for all *DNA* bases must exist, independent of their structural peculiarities (purines vs pyrimidines). Many scenarios have already been proposed and considered[202]; however, all of them assume different pathways involving different electronic states for different nucleobases. A universal mechanism of such a two-step photo-deactivation for all nucleobases and investigated nucleotides may be offered: the population passes from an initially excited bright state $\pi\pi^*$ through an $n\pi^*$ (dark) state to the ground state via two CIs, as schematically depicted in Figure 6.10. It should be noted that a similar scenario has been proposed and discussed for cytosine[26] and adenine.[27] However, this scenario should be valid for all *DNA* nucleobases because the only dark state common to all nucleobases is the $n\pi^*$ state. To support this mechanism, a theoretical modeling of 2D spectra in the vicinity of two CIs and ESAs was performed (see details in the recent publication[28]). Despite some model restrictions, the calculated 2D spectra match the observed spectra very well (see Figure 4b in reference[28], which shows the calculated 2D spectrum at $T = 330\,\texttt{fs}$)

The main feature of the 2DPE experimental spectra, two peaks with the opposite signs, is clearly reproduced, along with the overall spectral shape. It should be pointed out that both heating and cooling of the ground state are automatically included in these simulations as a time-dependent displacement of the tuning coordinate. However, if the spectroscopic model is restricted to only one CI (i.e., direct crossing of the $\pi\pi^*$ and ground states), no reasonable agreement between the simulated and measured 2D spectra is found. The possible origins of CIs in nucleobases were extensively investigated in numerous quantum chemistry theoretical studies. Yet, it should be stressed that these calculations were performed starting from perfectly optimized molecular structures. In a living molecule, immersed in a fluctuating environment (water at room temperature), a large number of CIs can be realized so that the population transfer between the excited $\pi\pi^*$ state and the dark $n\pi^*$ state is actually unavoidable.

In summary, all *DNA* nucleobases have an identical photo-deactivation mechanism characterized by two-step relaxation of the induced

electronic population through the dark state, which can be associated with the $n\pi^*$ state based on the modeling and experimental findings. This state connects the excited state $\pi\pi^*$ and ground state via two CIs. This newly established spectroscopic model for single DNA bases can help to develop the spectroscopic models for DNA molecules and thus to unravel their photo-deactivation mechanism and understand the DNA photo-stability.

Chapter 7

2D Photon echo and transient absorption spectroscopy of *ssDNA*

This chapter seeks to compare the photo-dynamics of individual nucleobases with short single strands of *DNA* in order to understand the effect of stacking on the photo-physical properties of *ssDNA*; the chapter presents the TA and 2DPE of $(dA)_n$ and $(dT)_n$ where n is either 2 or 4.

7.1 Sample preparation and detection conditions

The *DNA* oligomers were purchased from JenaBioscience GmbH in lyophilized form and used as received; desalting and purification were performed by the vendor. The strands were solvated in glass vials (clean room quality from Carl Roth) in a phosphate-based buffer made using desalted and distilled water (see Ch. 2.2). The solute concentrations were adjusted such that the maximum absorbance, at the maximum of absorption near $260\,\mathrm{nm}$, was between 0.25 and 0.35. The filtration of the samples was performed using a syringe pump (Aladdin 300- 220Z syringe pump from WPI) in a $5\,\mathrm{mL}$ syringe, at a speed of $0.5\,\mathrm{mL/min}$. The syringe filter used was a $0.1\,\mu\mathrm{m}$ Acrodisc supor sterile membrane (Pall Life). Before usage, the final solutions were stored in a fridge at $5°C$. The absorption spectra were measured using a UV2600 spectrophotometer (Shimadzu) in a $1\,\mathrm{mm}$ or $0.1\,\mathrm{mm}$ quartz cells (Hellma or Starna), and additionally controlled in situ

by measuring the transmission with a UV-sensitive photo-diode 2032 (Newport). The *DNA* oligomers were checked using a CD spectrometer (Chirascan-plus). After each set of measurements, the absorption and CD spectra and the pH of the samples were checked to ensure the sample did not have any photo-damage. The OD of all the samples was maintained at $0.25 - 0.35$ at maximum absorbance, and the pH was kept at ≈ 7 during the experiment. The solutions were circulated through a home-built wire-guided jet with the thickness in excited volume maintained at $150 \approx 250\,\mu\mathrm{m}$ (Ch. 3). The excitation spot size was $\approx 50\,\mu\mathrm{m}$ and, with the jet pump speed used $(3000 - 4000\,\mathrm{rpm})$, a refreshment of excitation volume was guaranteed for the laser repetition rate $(1\,\mathrm{kHz})$. The UV-pulses excitation energies were $15 - 20\,\mathrm{nJ}$ per beam.

The frequency-resolved 2DPE signals were collected with a scan range of $128\,\mathrm{fs}$ and a step of $1\,\mathrm{fs}$ at fixed waiting times T. At each delay point 1800 to 3600 single spectra were averaged to achieve high SNR. Each photon echo scan took approximately 6 to 12 minutes per one delay point T . The pump-probe spectra were typically collected in a delay range of $10\,\mathrm{ps}$ with a step of $20\,\mathrm{fs}$; each delay point is the result of averaging 7200 differential spectra (pump-on / pump-off). In the present chapter, the differential spectra are plotted as measured, without normalization of the probe spectra. In order to achieve the high spectral resolution needed for resolving the oscillations, the delay step was set to $5\,\mathrm{fs}$ in the PE measurements and the associated TA measurements (performed for phasing). PE spectra were always collected concurrently with a TA spectrum at the same population time T, and the PE spectra were individually phased with their corresponding TA spectrum (at the same T). TA spectra were fit with a multi-exponential model using a home-written software based on global fitting analysis.[166] Fitting of the experimental data was performed using multiple home-written programs within the Matlab shell. For a rationale regarding the global analysis fitting of pump-probe data, see Ch. 6.3.

The 2D spectra were created following the method described in Ref.[164]; the corresponding pump-probe spectra, measured at the same waiting times T, were used for their phasing. Although the phasing procedure used is described in detail in Ref.[164], due to the large spectral window in the 2DES experiments it was necessary to account for a wavelength dependence of the LO-filter refraction index. The 2D

spectra were then transformed to the time domain, filtered with a Gaussian-shaped kernel, and transformed back to the frequency domain. The filtering lowers the resolution in 2D spectra to approximately $200\,\mathrm{cm^{-1}}$.

7.2 Discussion

Fig. 7.1 shows the absorption spectra of the studied *ssDNA*, superimposed on the laser spectrum. In particular for $(dT)_n$, but also partly for $(dA)_n$, the laser spectrum covers the majority of the broad peak at $260\,\mathrm{nm}$. The absorption spectrum does not show any immediate differences, and even with the sophisticated treatments of Ch. 2, it is difficult to de-congest these spectra.

(a) $(dA)_n$ (b) $(dT)_n$
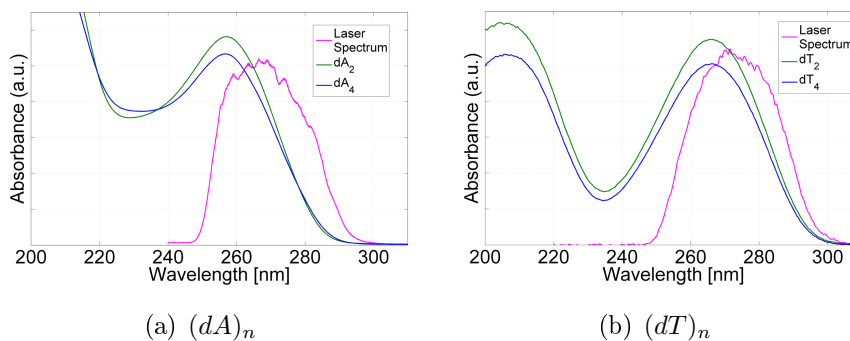
Figure 7.1: Absorption linear spectra of the short *ssDNA* investigated, with in pink an overlap of the laser spectrum: 7.1(a) $(dA)_2$ and $(dA)_4$, 7.1(b) $(dT)_2$ and $(dT)_4$.

The time-resolved dynamics of the excitation are shown in Fig. 7.2 the TA of $(dA)_2$, $(dA)_4$, $(dT)_2$, $(dT)_4$, with the corresponding DAS. Firstly, one notices two peaks that, although present in the TA of the isolated nucleosides, here are more pronounced and more separated from each other (Figures 6.8 and 7.2). The two peaks could be attributed to a Davydov splitting[99] as a result of a weak dipole interaction between the pi-stacked nucleobases in the strand. Due to the significant contribution of the solvent interaction, the static absorption in Fig. 7.1 does not show such splitting as the spectra are very congested, while it is observable in the TA due to the narrowing of the peaks as the delay time increases. The splitting can be used to calculate the electronic coupling V whose upper limit for symmetric

137

systems is[101]:

$$|V| = \frac{\Delta E_{mn}}{2} = \frac{|E_m - E_n|}{2}, \tag{7.1}$$

The experimental data show that $V((dT)_4)$ equals $116.72\,\mathrm{meV}$, while $V((dA)_4)$ equals $84.21\,\mathrm{meV}$. These values clearly do not match the values calculated by Blancafort[101], who reports $54.5\,\mathrm{meV}$ for $(dT)_2$ and $20.8\,\mathrm{meV}$ for $(dA)_2$. Using theory from Burin[125], and the experimental steady state absorption and CD spectra, the values of the exciton splitting were retrieved (Ch. 2.7, in particular Fig. 2.7), that also counters such large values. Another hypothesis is that such bands in the experimental TA spectra of $ssDNA$ are associated with a more pronounced interplay between vibronic levels, which can only be demonstrated conclusively by theoretical simulations.

$ssDNA$	fast [ps]	intermediate [ps]	slow [ps]
$(dA)_2$	0.70	2.26	∞
$(dA)_4$	0.75	2.33	∞
$(dT)_2$	0.75	1.30	∞
$(dT)_4$	0.75	1.94	∞

Table 7.1: Values of the three components (slow, intermediate and fast) for the four short $ssDNA$ studied. Uncertainties of fast and medium lifetimes are $\approx 5\%$.

The results of the global fitting analysis, with one life-time fixed to be infinitely long, are the multiple DAS in Fig. 7.2, and Tab. 7.1 that show three components with a similar shape as the nucleobases (Fig.6.8 middle row). There are two exceptions. Firstly, while the value of the life-time of the shortest component is similar in both the isolated nucleobases and the DNA strands, the value of the lifetime of the middle component approximately doubles in $ssDNA$. This suggests that a mechanism is more prominent, or a novel one has arisen that is not already described for the isolated nucleobases. The second difference is the increased amplitude of the slow component in $ssDNA$ as compared to the nucleobases. It is possible to speculate that the origin of such a long slow component in $ssDNA$ is due to the well-known higher yield of the triplet states in $ssDNA$.[15,16,66,203] It should be noted that preliminary measurements on $(dA)_{10}$ and $(dA)_{20}$ show similar kinetics to the ones presented here.
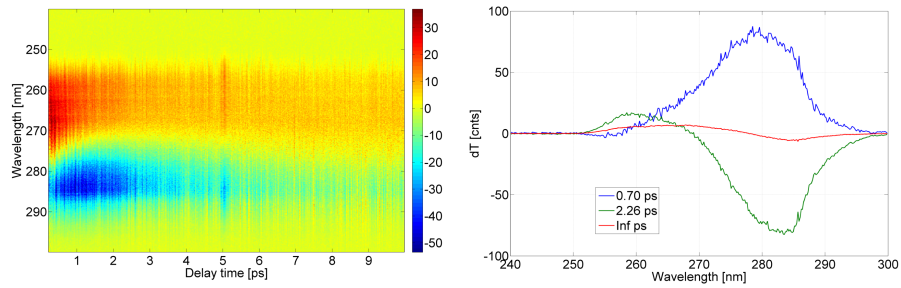
(a) TA spectra of $(dA)_2$

(b) DAS of $(dA)_2$
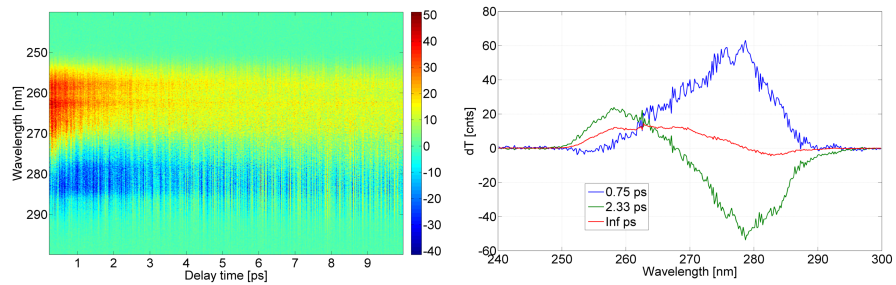
(c) TA spectra of $(dA)_4$

(d) DAS of $(dA)_4$
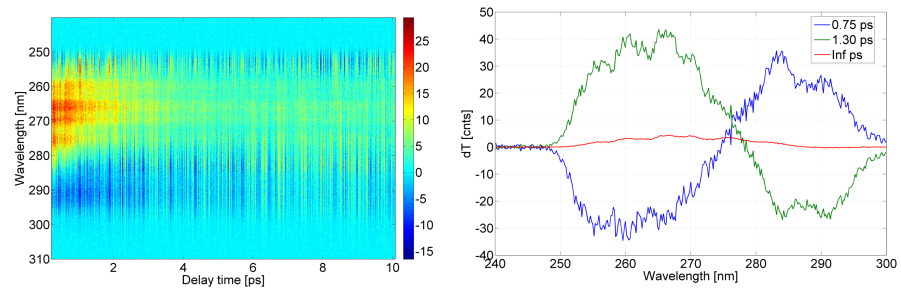
(e) TA spectra of $(dT)_2$

(f) DAS of $(dT)_2$
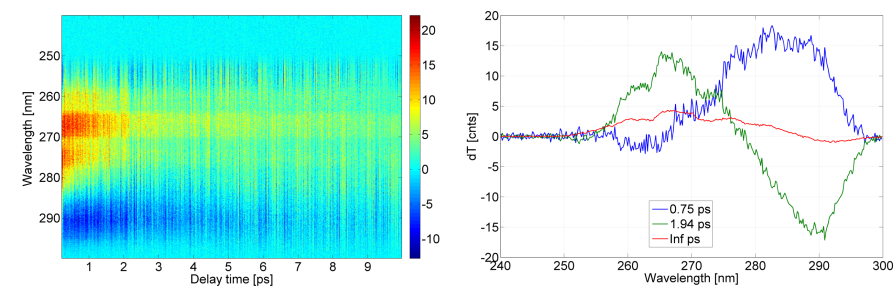
(g) TA spectra of $(dT)_4$

(h) DAS of $(dT)_4$

Figure 7.2: Summary of the pump-probe spectra and their decay associated spectra of the $ssDNA$(oligomers) investigated.

There are already such examples in the literature.[6,13,15,16,39,71] For instance, Kwok et al.[16] investigated $(dT)_{20}$, and found three lifetimes experimentally comparable to the once presented here (0.2 ps , 1.50 ps , and 140 ps). They assign such lifetimes to a fast decay from the initially excited S_π state to the S_n state, an intermediate intersystem crossing to a T_1 triplet state, and at last a relaxation to a CPD state.[16] Similarly in Ref.[15], Kwok et al. also report for $(dA)_{20}$ three lifetimes (0.39 ps , 4.3 ps , and 182 ps), and assign them to a population transfer between an "A-like" state, where the excitation is localized on a single adenine base, to an excimer state E_1, before the population is transferred to the excimer state E_2. There is a lack of theoretical framework for assigning the components found in the present work.
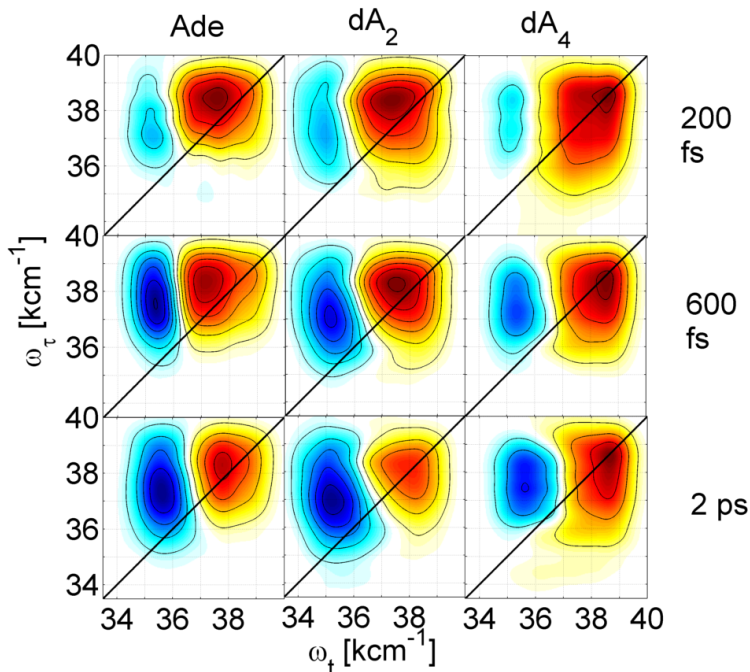
Figure 7.3: Real part of PE spectra of adenine (left), $(dA)_2$ (center), and $(dA)_4$ (right) at three different delay times T: $T = 200$ fs (top), $T = 600$ fs (middle), and $T = 2$ ps (bottom). The contour steps are in 10% magnitude. Each spectrum is normalized to its maximum.

In Fig. 7.3, the real part of representative PE spectra of the short single strands $(dA)_2$ and $(dA)_4$ are compared to the corresponding PE spectra of adenine. While no new feature is readily apparent when moving from adenine to $(dA)_2$ and $(dA)_4$, the ground state bleaching and excited state dynamics have different dynamics, confirming the results of transient absorption. It should be noted that preliminary

measurements on $(dA)_{10}$ and $(dA)_{20}$ show similar spectra to the ones presented here. Currently, there still are no 2D spectroscopy experimental results in the literature that can be compared to the results from this study.
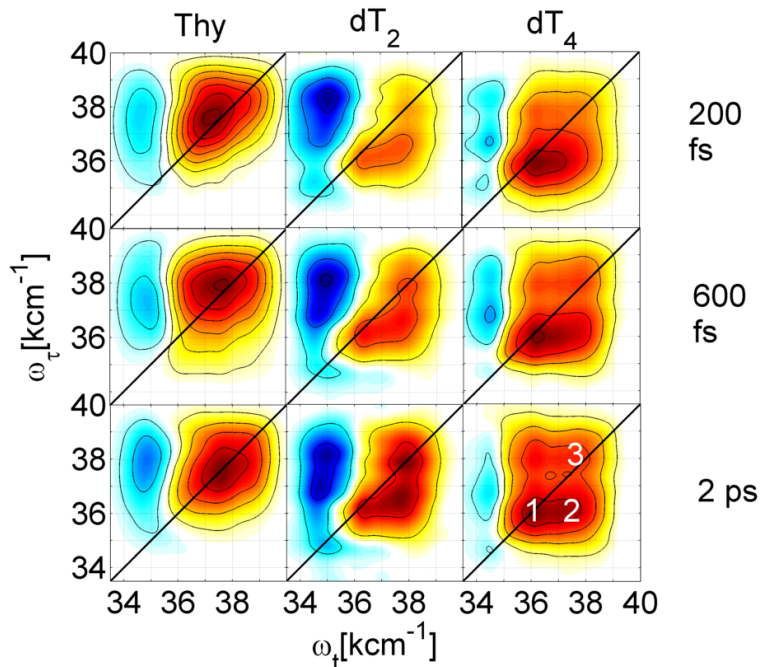
Figure 7.4: Real part of PE spectra of thymine (left), $(dT)_2$ (center), and $(dT)_4$ (right) at three different delay times T: $T = 200\,\mathtt{fs}$ (top), $T = 600\,\mathtt{fs}$ (middle), and $T = 2\,\mathtt{ps}$ (bottom). The contour steps are in 10% magnitude. Each spectrum is normalized to its maximum. On the spectrum of $(dT)_4$ and $T = 2\,\mathtt{ps}$ three numbers are printed. Those correspond to the peak oscillations in Fig. 7.5.

Fig. 7.4 shows the real part of PE spectra at three different delay times T; the figure compares the spectra of thymines and single strands of $(dT)_2$ and $(dT)_4$. A new off-diagonal peak at (37,36) is present. The significance of this peak is unclear. As speculated in the transient absorption data, it is either due to a charge or energy transfer, or a particularly intense vibronic interplay. To explore this further, a set of PE spectra with very near scan times T were taken to better follow the variation of the intensity as T changes. This is shown in Fig. 7.5, where the oscillations in the three peaks appear in phase. There seems to be a longer oscillation, with a 10-fold slower frequency, convoluted with the fast frequency ($1500\,\mathrm{cm}^{-1} \approx 22fs$), with a periodicity of $\approx 200\,\mathtt{fs}$). Currently a longer experimental scan is programmed, thus enabling the resolution of more than one period-

icity of the slow oscillation, which origin is yet to be determined.
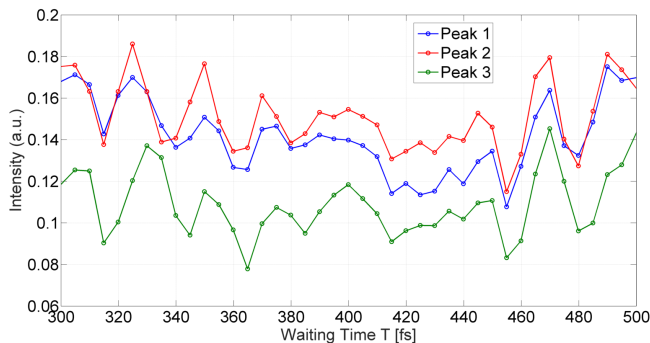
Figure 7.5: Variation with the delay time T of the intensity of the real part PE signal at three different peak locations, corresponding to the numbers in Fig. 7.4, bottom right spectrum.

7.3 Conclusions

To the best available knowledge, this is the first experimental broad-band transient absorption and 2D spectra of $ssDNA$ in the far UV ever reported. A comparison with the spectra of the respective single nucleobases shows a number of similar features, but also differences. In particular, the intermediate lifetime increases when nucleobases are stacked in $ssDNA$, and the amplitude of the DAS associated with the longest lifetime increases. Moreover, the 2DPE spectra suggest the possibility that a different mechanism causes excitation in $ssDNA$ than the mechanism for excitation of nucleobases. Currently, a theoretical framework that would describe the above-mentioned features is lacking. However, future work could be enriched by building such a theoretical framework, as well as experimental study of $dsDNA$.

Chapter 8

Summary

This study presented a series of novel methods and findings regarding time-resolved study of DNA and its nucleobases. In particular, an extensive characterization of nucleobases and short strands of DNA was conducted by means of steady-state absorption and circular dichroism spectroscopy (Ch.2). Using these techniques, it became possible to calculate transition dipole moments and excitonic coupling.

A careful Gaussian decomposition of spectra revealed the presence of two major electronic excitations below the broad and featureless peak at $260\,\mathrm{nm}$. Moreover, a linear relationship was uncovered between the number of nucleobases in a single strand of DNA and the dipole strength. Further analysis of absorption and CD spectra by a clever normalization uncovered a non-trivial dependence of the delocalization extent of excitons on the length of the oligomeric chain. Excitons delocalize only amongst nearest neighbors in adenosine oligomers, while $(dT)_n$ and $(dAT)_n$ oligomers have excitons that delocalize in a growing range of neighbors as strand length increases. Furthermore, the method described by Burin et al.[125], was applied to calculate the values of the excitonic coupling, which agree well with simulated ones.[101] While the results qualitatively agree with the samples in the study, there are two exceptions. First, all three families present with outliers in the samples with two and four nucleobases, while this is not observed when using the normalization procedure of the present work. Second, the order of the strength of the excitonic coupling calculated using Burin's method and the method in this study is reversed with respect to the dipole strength order. Currently, the origin of these differences is not fully understood; it may be due to a non-canonical disposition of the nucleobases within the strands, as supported by the

simulated CD spectra.

To the best available knowledge, this is the first experimental broadband transient absorption and 2D spectra of $ssDNA$ in the far UV ever reported. A comparison with the respective single nucleobases shows a number of similar features, but also differences. In particular, the intermediate lifetime increases when nucleobases are stacked in $ssDNA$, and the amplitude of the DAS associated with the longest lifetime increases. Moreover, the 2D spectra suggest the possibility that a different mechanism causes excitation in $ssDNA$ than the mechanism for excitation of nucleobases. Currently, a theoretical framework that would describe the above-mentioned features is lacking. However, future work could be enriched by building such a theoretical framework, as well as experimental study of $dsDNA$.

A close-loop wire-guided jet system (WGJ) was developed as a sample holder for ultrafast spectroscopic experiments. Design details and the full characterization of the WGJ are included in Ch. 3. Moreover, the broadband far-UV 2D photon echo and transient absorption optical setup described in Ch. 4 allows for the investigation of the electronic-vibronic states of selected molecular systems.

Chapter 5 examined pyrene from both a theoretical and experimental perspective. This study offers two alternative mechanisms for the de-excitation of pyrene. The first is that the excitation of the S_4 is followed by a sub-picosecond relaxation of the excited population to the phantom state S_3, then to the S_2 ($8\,\mathrm{ps}$) and finally to the L_b states ($24\,\mathrm{ps}$), assuming the characteristics of S_1 at the minimum; the population is trapped for an extended time in the S_1/L_b bottle-neck minimum before relaxing to the ground state, whose time-scales are longer than the experimentally allowed time-scale maximum ($200\,\mathrm{ps}$). The second is that there is only a single conical intersection between S_3 and L_b, and the fluorescence structure at $350-368\,\mathrm{nm}$ is instead associated with a relaxation from the L_b after the CI with the phantom state; the S_2 level is not involved in de-excitation.

The study of pyrene was further enhanced by investigating PE spectra and Raman frequencies. The transitions in the PE spectra were found to be mainly due to vibronic transitions and ground state relaxations. In the case of Raman frequencies, these values are in agreement with the literature and matched either the assigned breeding in the aromatic rings, or C-C and C-H stretches.

The experimental findings regarding nucleobases (Ch. 6) are that

144

there is an universal mechanism of two-step photo-deactivation, equally valid for all the investigated DNA bases regardless of structural peculiarities. In this mechanism, the population passes from an initially excited bright state $\pi\pi^*$ through an $n\pi^*$ (dark) state to the ground state via two CIs; this had been previously proposed for cytosine[26] and adenine[27], but was extended here to all nucleobases and nucleotides, given that the dark state shared by all nucleobases is the $n\pi^*$ state. Furthermore, theoretical modeling of 2D spectra in the vicinity of two CIs and ESAs[28] was conducted, and closely matched the experimental spectra, reproducing the two peaks with opposite signs that are the main feature of the 2DPE experimental spectra.

This study is the first experimental broadband transient absorption and 2D spectra of $ssDNA$ in the far UV. There are both similarities and differences to the respective single nucleobases. The intermediate lifetime increases when nucleobases are stacked in $ssDNA$, as well as the amplitude of the DAS associated with the longest lifetime. Furthermore, the experimental data suggest that the mechanism that causes excitation in $ssDNA$ is different than the mechanism of excitation of nucleobases; however, the theoretical framework to describe these features is lacking.

Chapter 9

Outlook

9.1 *DNA* photo-damage in the far UV

It is well known that photo-absorption leads to photochemical reactions and photophysical effects in biological molecules. In particular, *DNA* photo-damage is well documented, beginning with the first studies in the mid-seventies.[204] The photo-damage caused by UV light has been studied for the high risk of cell and *DNA* degradation. UV light is divided into 3 domains: UV-A covers the spectral region extending from $400\,\mathrm{nm}$ to $315\,\mathrm{nm}$, UV-B from $315\,\mathrm{nm}$ to $280\,\mathrm{nm}$ and UV-C from $280\,\mathrm{nm}$ to $100\,\mathrm{nm}$. The earth atmosphere absorbs the UV up to $260\,\mathrm{nm}$, meaning the UV-C, hence the studies concentrated on studying the influence of UV-A and UV-B light. For the same reason, sunblock creams block UV up to UV-B, but are not tested for the UV-C domain. However, due to human influence, the atmosphere is changing: a hole in the ozone layer protecting the Earth's surface against UV-C grows steadily in the southern hemisphere. Antarctica, Australia, and New Zealand are mostly impacted, and studies show a recrudescence of skin cancers for individuals living in New Zealand and Australia.[205] For this reason, studying the absorption of UV-C of *DNA* and the induced photo-damage is of primary interest.

Most of the studies have been conducted by using light sources emitting at $254\,\mathrm{nm}$ (UV-C).[42,110,206,207] To the best knowledge of the author, no study has been realized with coherent light in the more energetic part of UV-C, lower than $240\,\mathrm{nm}$. Yet the character of photo-damage in *DNA* may differ significantly after exposure to different wavelengths.

DNA absorption spectrum, as for example shown in Figures 2.2,2.3

and 2.4, show two absorption bands in the UV. The most studied is the one centered near 260 nm. The absorption peak centered at 213 nm indicates a photo-interaction in the UVC. The biological effect of 213 nm on *DNA* has not yet been studied and is unclear.

Photon absorption in nucleobases at 254 nm promotes an electron from its LUMO, a π orbital, to the HOMO, an antibonding π^* orbital.[42] The exact timescale is estimated to be in the picosecond range. From this unstacked single nucleobase excited state to the electronic ground state, the main pathway is through a rapid de-excitation to the HOMO by nonradiative transition or fluorescence yielding heat.[208] The probability of an intersystem crossing pathway is instead very small, changing its spin multiplicity from a singlet to a triplet excited state; the life time of this triplet state is of the order of a few μs, which is an order of magnitude longer than the excited singlet state. On this timescale, the chance of photoproduct formation is increased.[16] The generated photoproducts include both stable and unstable intermediate products, like free radicals. Not much is known of the properties of the peak of 213 nm. It is desirable to extend the study from 254 nm to 213 nm, as similar photodamage is expected at this higher wavelength.

The aim of the proposed experiment is to establish the effect of photo-irradiation on *DNA* molecules when the irradiation wavelength is 213 nm, both from a physical-chemical point of view and a biological one. Strong photo-dimerization processes are expected, due to a lesion of the phosphate backbone in *DNA*, as shown in the preliminary results, but other processes will also be taken in account. To achieve this goal, *DNA* samples that are dissolved in a mild phosphate-based buffer are irradiated to simulate the effects of solar exposure, with a fifth harmonic generation able to generate a laser pulse with a wavelength of 213 nm as described in 9.2, where some preliminary results are also presented.

The *DNA* would then undergo a series of checks to determine the presence and the quantity of bio-chemical damage, using techniques like:

- absorption and circular dichroism spectroscopy,
  The formation of dimers in the absorption and circular dichroism spectra features blue or red shifts of the peaks, shape changes, intensity variations and butterfly shapes (Cotton effect). The conformational change of *DNA* strands, in particular of the secondary structure, is visible in the circular dichroism spectra.

- electrophoresis,
  Electrophoresis gel is a routinely used technique to separate a mixed population of *DNA* fragments by length, to estimate their size and to detect and determine the length of the *DNA* and qualitatively the secondary structure changes, as electrophoresis is sensitive to the amount of charges present on the phosphate backbone, unless the *DNA* is folded and therefore the charge decreases. It is also a preparatory technique for mass spectrometry and sequencing.

- MALDI-TOF mass spectrometry,
  The mass of each nucleotide is different from the others and this difference is detectable by mass spectrometry. Single nucleotide mutations in a fragment can be detected as well.

- HPLC,
  High-performance liquid chromatography (HPLC) will be used to separate the different *DNA* and to identify and quantify them taking advantage of the different mass-to-charge ratios of the nucleotides and their dimerizations.

- DNA sequencing,
  DNA sequencing determines the precise order of nucleotides in order to understand the dependence of the damage of a nucleotide from the neighbouring ones[207].

9.2 Preliminary results

UV irradiation is obtained by harmonic generations from the output of a picosecond infrared laser, model APLQ-3000 from Attodyne Inc., Canada. The output of this laser is specified for the wavelength of $1064\,nm$, the pulse duration of $10\,ps$ and the repetition rate of $1\,kHz$. A *built-in-house* optical system performs three steps of harmonic generation, which converts the fundamental irradiation at $1064\,nm$ to UV irradiation at $213\,nm$. The preliminary results are encouraging; the sample of *DNA* used was a random sequence from Sigma Aldrich, T rich, with an exposure time of 45 minutes. Every 15 minutes an absorption spectrum was taken and compared to previous spectra. The absorbed energy was monitored in real time and was approximately of the value of $34\,\mu J$. The spectra show a increasing strong blue-shift
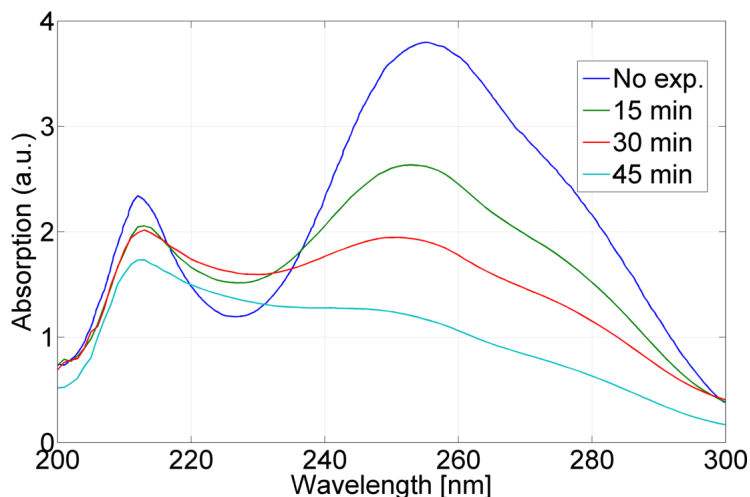
Figure 9.1: *DNA* absorption spectrum (blue) compared with the spectra of the same sample after (green) 15, (red) 30 and (light blue) 45 minutes of exposure.

of several nm and a decreasing of the peak ratio between $213\,nm$ and $260\,nm$, with increasing exposure time, as shown in Fig. 9.1. In particular, the peak that initially is at $213\,nm$ does not shift in wavelength nor in intensity, but the peak initially at $259\,nm$ shifts for the first 15 minutes of exposure by $6\,nm$, then by further $2\,nm$ each 15 minutes. The ratio between the two peaks decreases from a initial value of 1.5 to 0.8.

Further studies are necessary, in particular to establish if the base sequence is an important factor and to increase the total exposure time. Other studies could involve the use of a filter to understand the dependence of photo-damage on the energy of the irradiating field.

9.3 Outlook

This proposed experiment is limited to the determination of the products of dissociation and photo-dimerization of the DNA irradiated with 213 nm ultrashort pulses. The methods proposed to reach this goal rely on the analysis of the products resulting from the dissociation and damage of the *DNA*. Further analysis of these products would include vibrational spectroscopy. The molecules vibrate with THz frequencies corresponding to the MIR spectral domain. MIR spectroscopy or even spectroscopy with longer frequencies up to the THz region would allow a finer determination of the photoproducts.

The dynamics of the dissociation process might be studied with pump-probe experiments, where an ultrashort, UV laser pulse excites the *DNA*, and a MIR laser pulse probes the molecular states. Such THz laser sources are currently being developed at CFEL and further experiments are envisaged for the future.

9.4 Nucleobases and analogs solid-state sample preparation

Unraveling the optical properties of DNA and nucleobases is essential to understanding their biochemical functions and pathology, such as the influence of UV light on cancer formation. To clarify the complicated dynamics of DNA nucleobases, it is necessary to employ highly sophisticated, time-resolved two-dimensional spectroscopy techniques. Using the recently developed broadband two-dimensional photon-echo electronic and transient absorption spectroscopies, photoinduced relaxation processes were investigated in a number of nucleotides and their analogs in physiological liquid. One obstacle is the non-linear response of the solvents at very fast time scales (less than 150fs), where many interesting mechanisms occur. The main strategy to improve the quality of obtainable information is to reduce or eliminate the employed quantity of solvent by using solid-state samples of the molecules studied.

One approach is to deposit samples on a titanium-sapphire window to produce a multi-crystalline surface, or indeed crystallization proper, consequently characterizing the obtained samples with a spectrophotometer (in-use) and several other techniques. The obtained samples will then be used in the home-built multi-dimensional spectrometer.

9.5 Temperature ramping photon echo and transient absorption studies of single and double stranded DNA

DNA can also adopt a non-structure B-*DNA*, meaning that the bases are parallel to each other. To examine this, *DNA* can be forced to unfold and then its dynamics (and the difference at room temperature) studied. In particular, it is believed that poly-oligomers assume the

shape of B-*DNA*, while their CD spectra don't necessarily confirm this assumption, in particular when the chain is long. The characteristic of B-*DNA* is to have bases stacked on each other in a parallel fashion. $(dT)_n$, though, tends to make hairpin loops, and this affects the conformation (meaning the relative position of the different thymines) and thereby the position of the dipole moments. This means it may be possible that hairpin loops, rather than B-*DNA*, are under investigation.[209] It would be interesting to see if it is possible to forcefully vary this structure and study its dynamics. There are many ways to unfold (denatured) *DNA*, for example introducing small quantities of ethanol or urea in the buffer. However, these are not easily reversible. Temperature ramping is completely reversible, allowing for a complete study of the whole melting curve cycle. This would be the first step toward a non-stacked bases study. From a technical point of view, the experiment is already set up, except for the temperature change/control. This part can be achieved by modifying the existing flow jet system as follows: putting a coil around one of the tubes, just before the sample outlet, and testing the temperature inside the collector, by using a very long temperature tip probe (pH probes measure also temperature).

Appendix A

Additional figures

A.1 Closed-loop pump-driven wire-guided flow jet
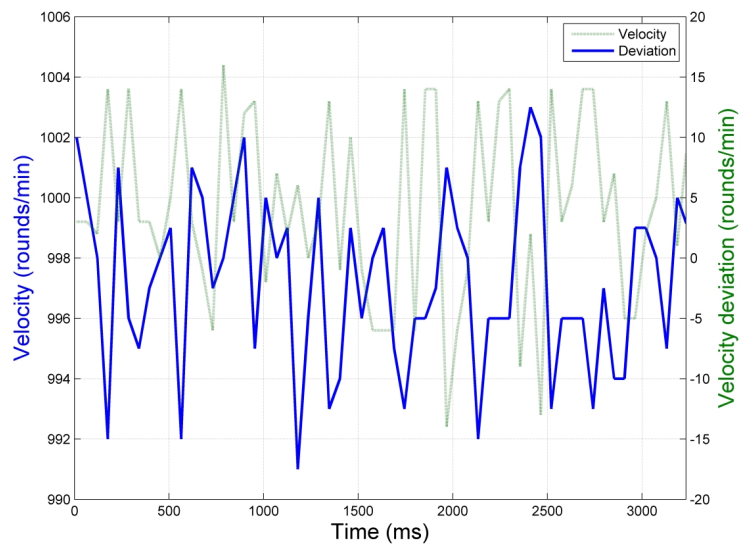
(a) 1000 rounds/min
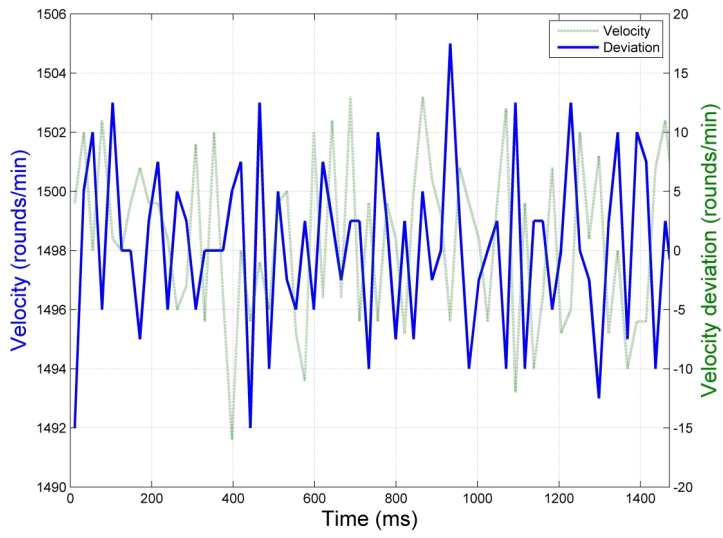
(b) 1500 rounds/min
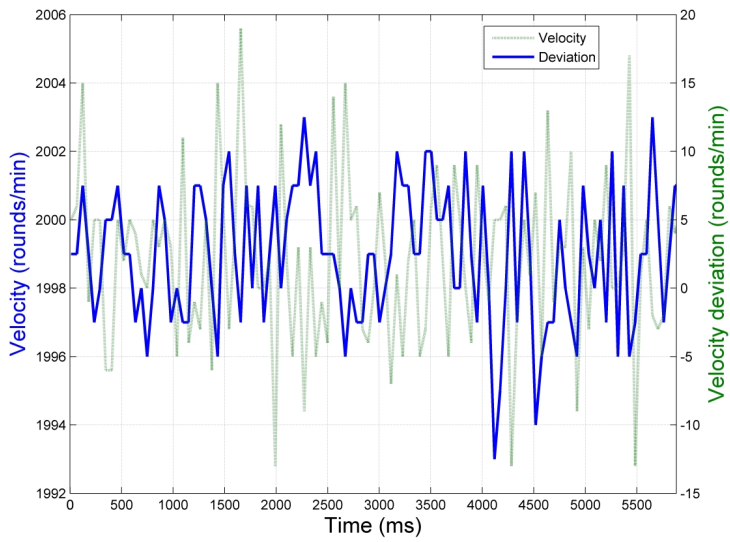
(c) 2000 rounds/min

(d) 2500 rounds/min

154
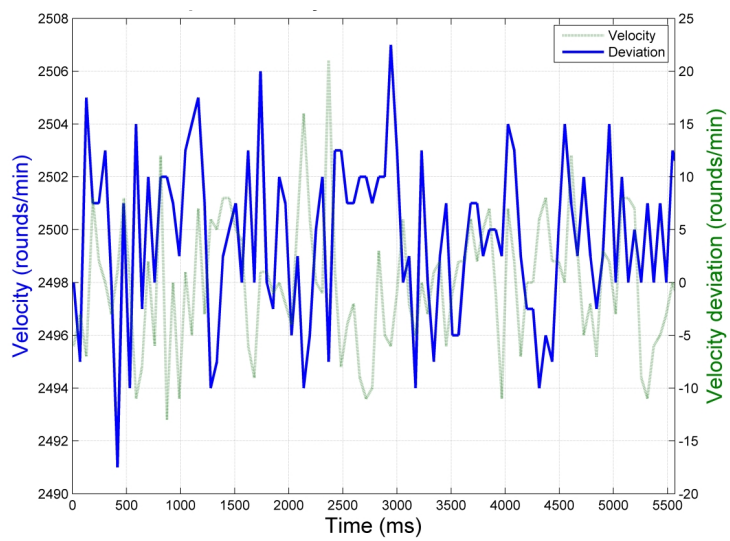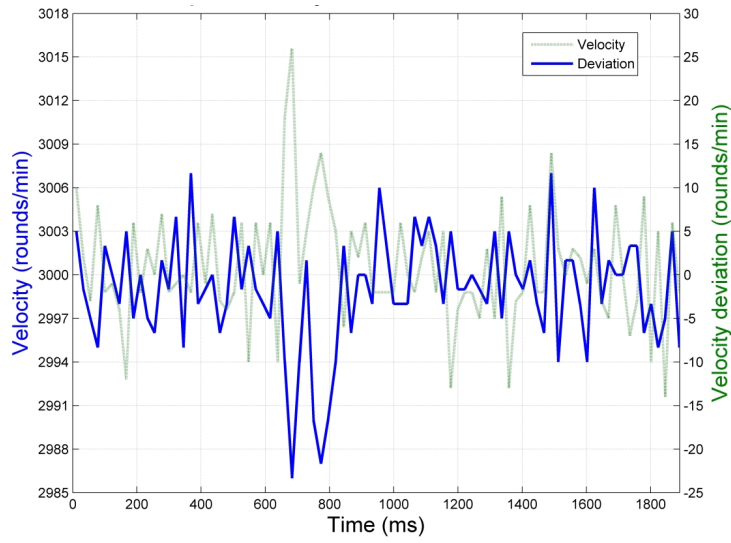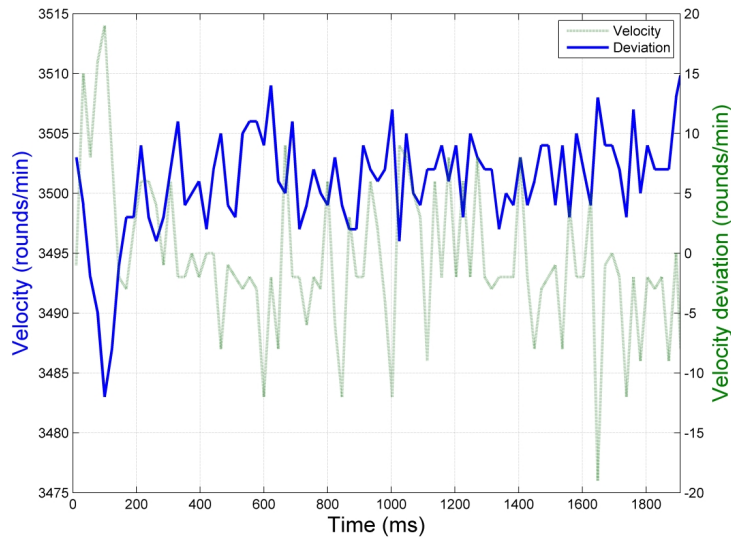
(e) 3000 rounds/min

(f) 3500 rounds/min

(g) 4000 rounds/min

155
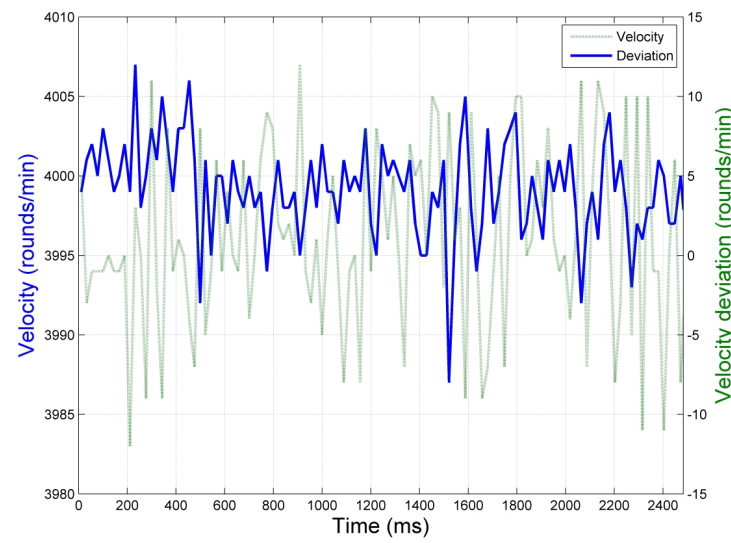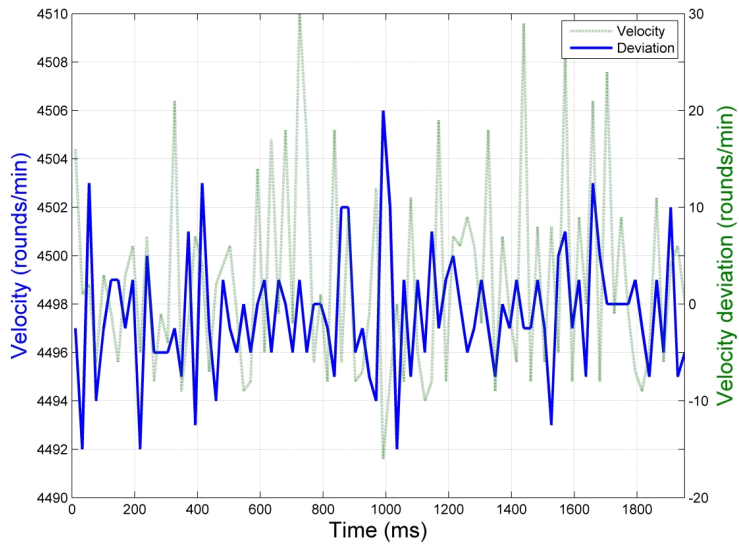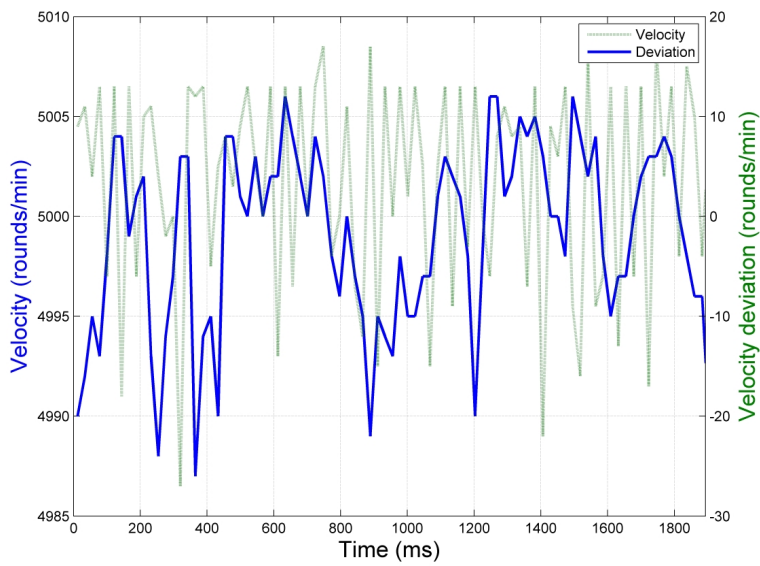
(h) 4500 rounds/min

(i) 5000 rounds/min

Figure A.0: [a-i] For each set pump velocity the *actual velocity* (on the left side of the plots, in blue line) and the velocity deviation (on the right side of the plots, in green line) were recorded.

A.2 Selection and characterization of biological samples
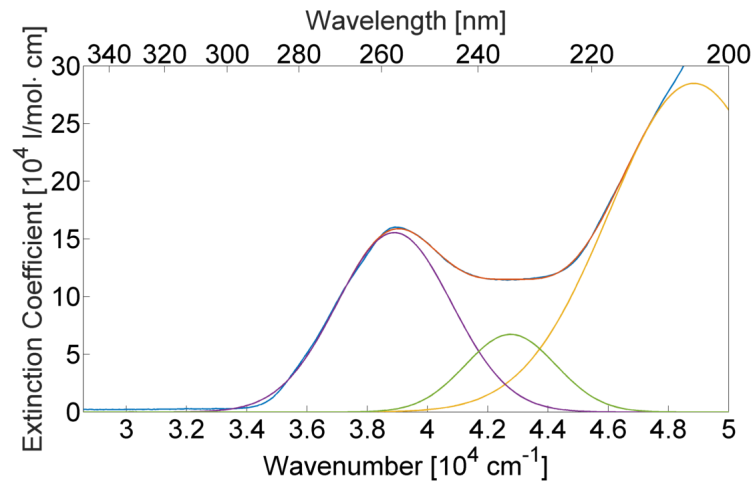
Figure A.1: An example of an absorption spectrum fit using three Gaussians, for $(dA)_{10}$
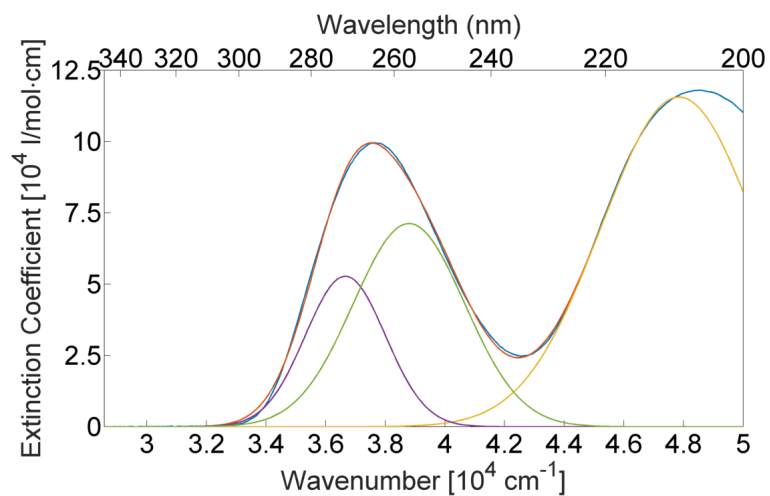
Figure A.2: An example of an absorption spectrum fit using three Gaussians, for $(dT)_{10}$
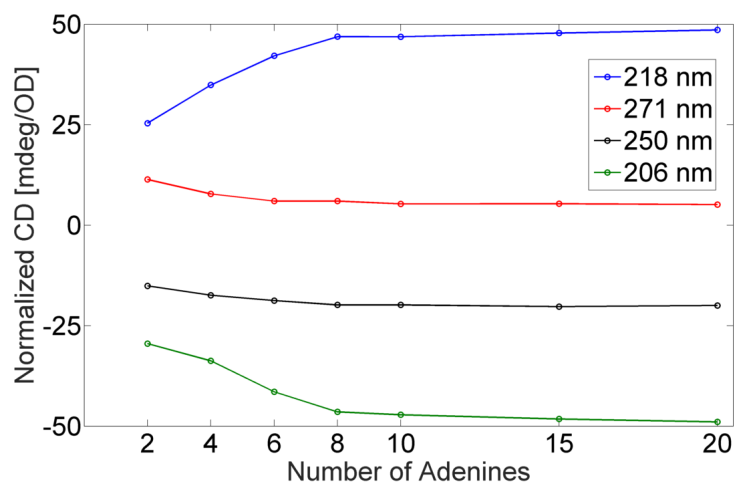
Figure A.3: Maxima and minima of the normalized CD spectra of $(dA)_n$ are shown as a function of the number n of adenosines composing the single strand for peaks at $218\,\text{nm}$ (blue line), $271\,\text{nm}$ (red line), $250\,\text{nm}$ (black line) and $206\,\text{nm}$ (pink line).
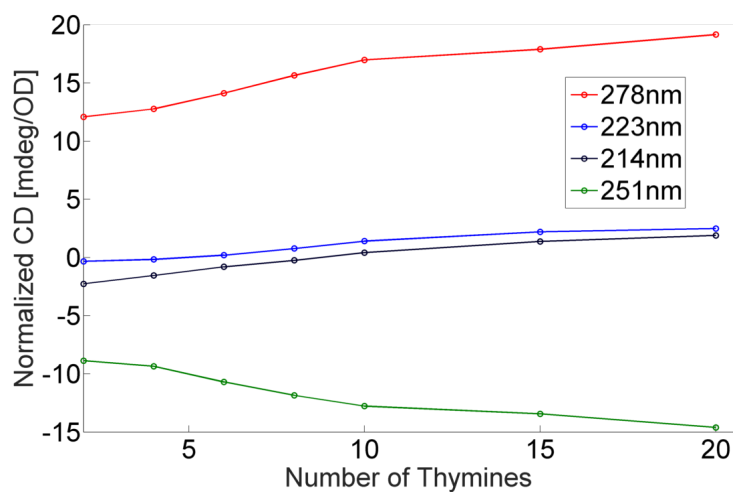
Figure A.4: Normalized CD maxima and minima, at specific wavelengths, of $(dT)_n$ are shown as a function of the number (n) of thymidines composing the single strand. The chosen wavelengths correspond to peaks at $223\,\text{nm}$ (blue line), $278\,\text{nm}$ (red line), $214\,\text{nm}$ (black line) and $251\,\text{nm}$ (pink line).
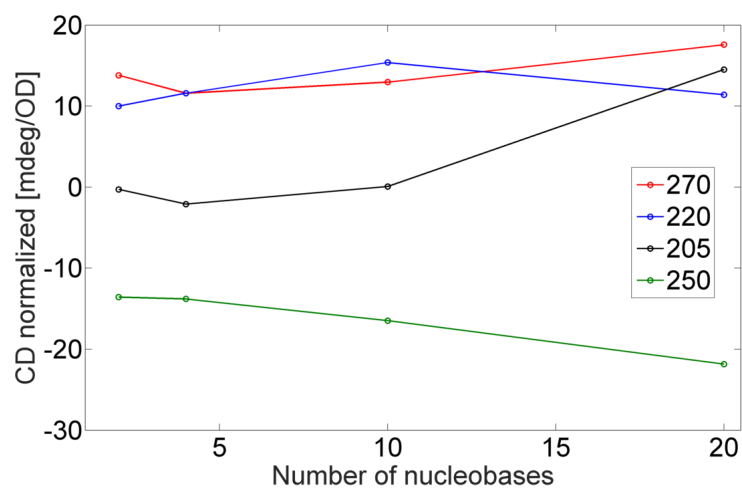
Figure A.5: Normalized CD maxima and minima, at specific wavelengths, of $(dAT)_n$ are shown as a function of the number (n) of nucleobases composing the single strand. The chosen wavelengths correspond to peaks at $220\,\text{nm}$ (blue line), $270\,\text{nm}$ (red line), $205\,\text{nm}$ (black line) and $250\,\text{nm}$ (green line).
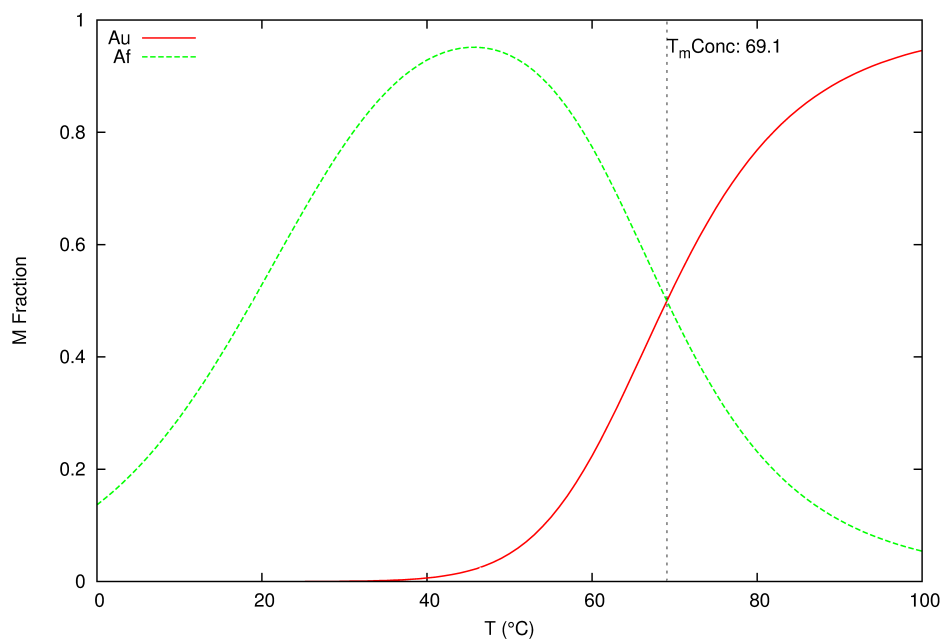
Figure A.6: Fraction of double stranded (folded) $(dAT)_{10}$ (green dashed curve) and single stranded (unfolded) $(dAT)_{10}$ (red full line), with varying temperature. The melting temperature is marked with a vertical black line at $69.1^\circ C$.
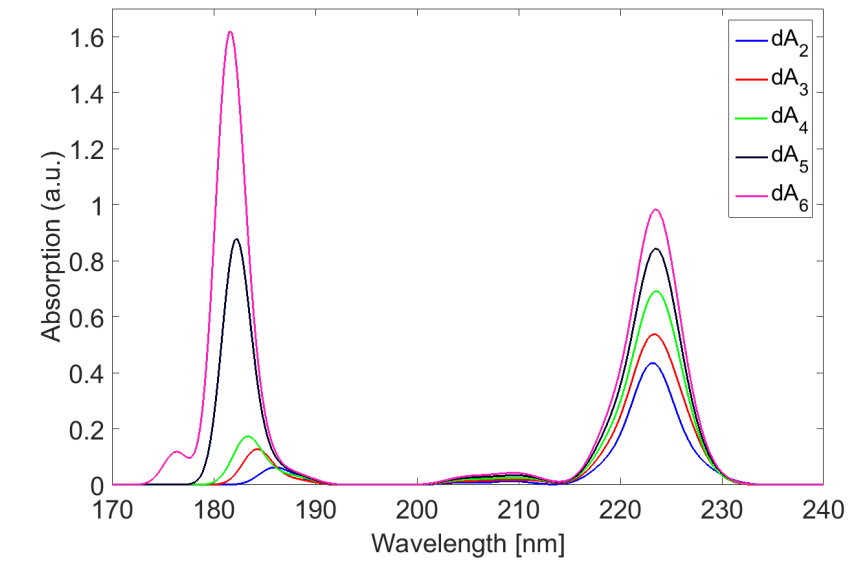
(a)
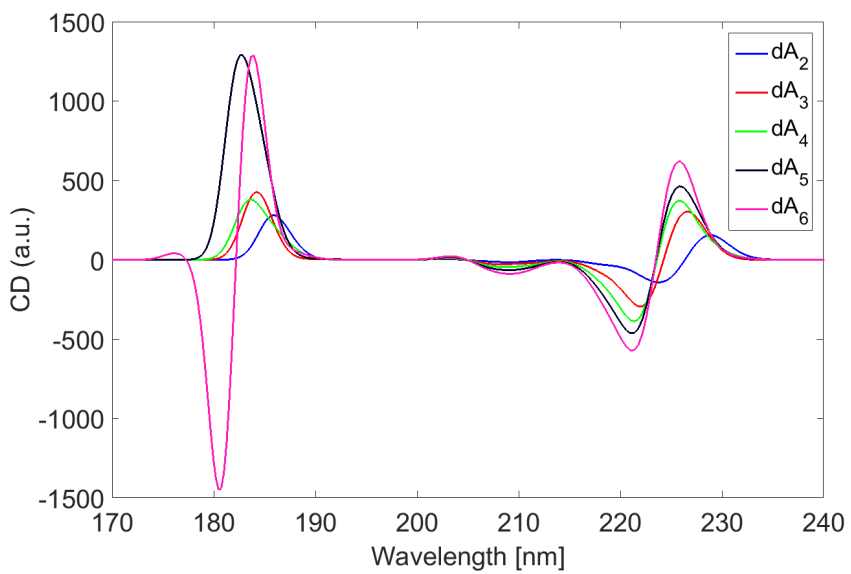
(b)

Figure A.7: Simulated absorption (a) and circular dichroism spectra (b) of $(dA)_n$, where n is the number of bases composing the strand, from 2 to 6.
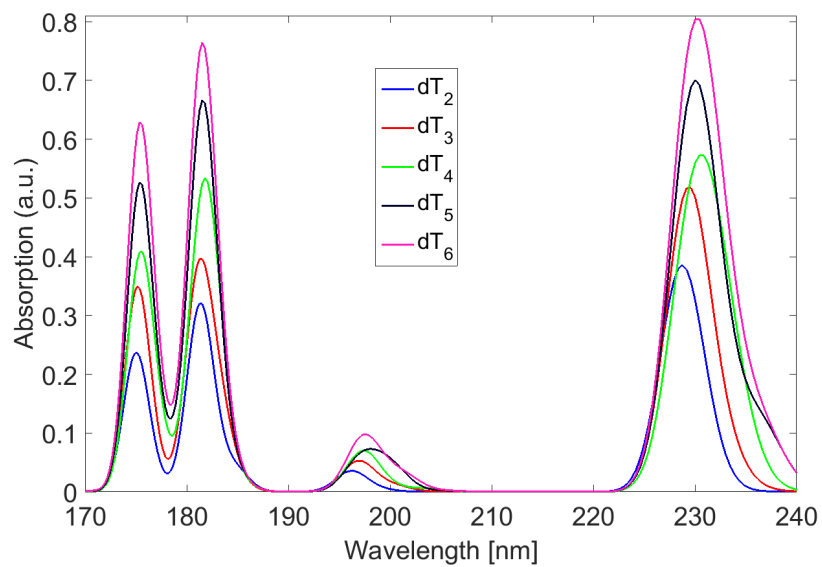
(a)
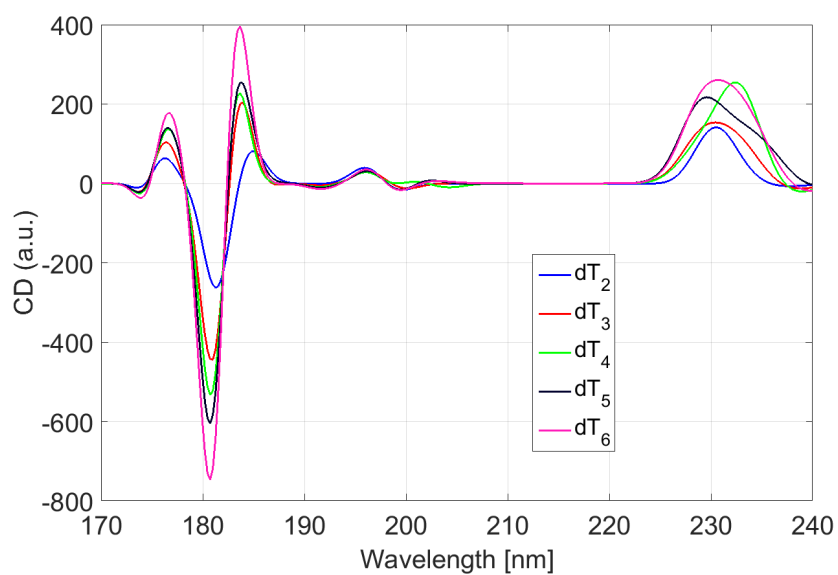
(b)

Figure A.8: Simulated absorption (a) and circular dichroism spectra (b) of $(dT)_n$, where n is the number of bases composing the strand, from 2 to 6.
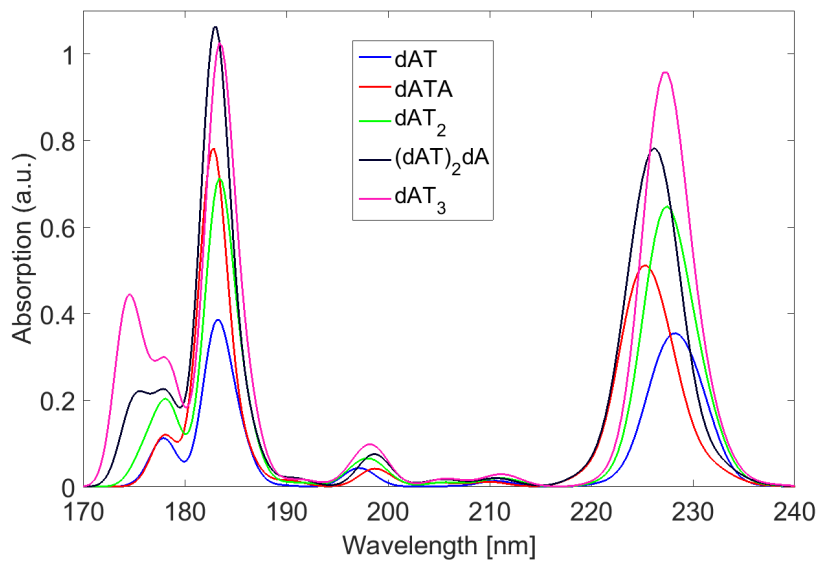
(a)
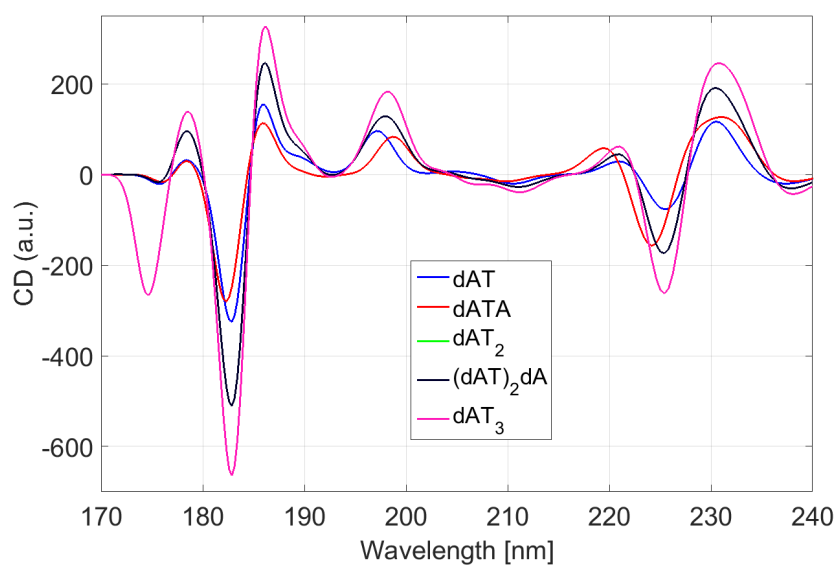
(b)

Figure A.9: Simulated absorption (a) and circular dichroism spectra (b) of A-T repeates, where n is the number of bases composing the strand, from 2 to 6.

A.3 Transient grating and photon echo on pyrene
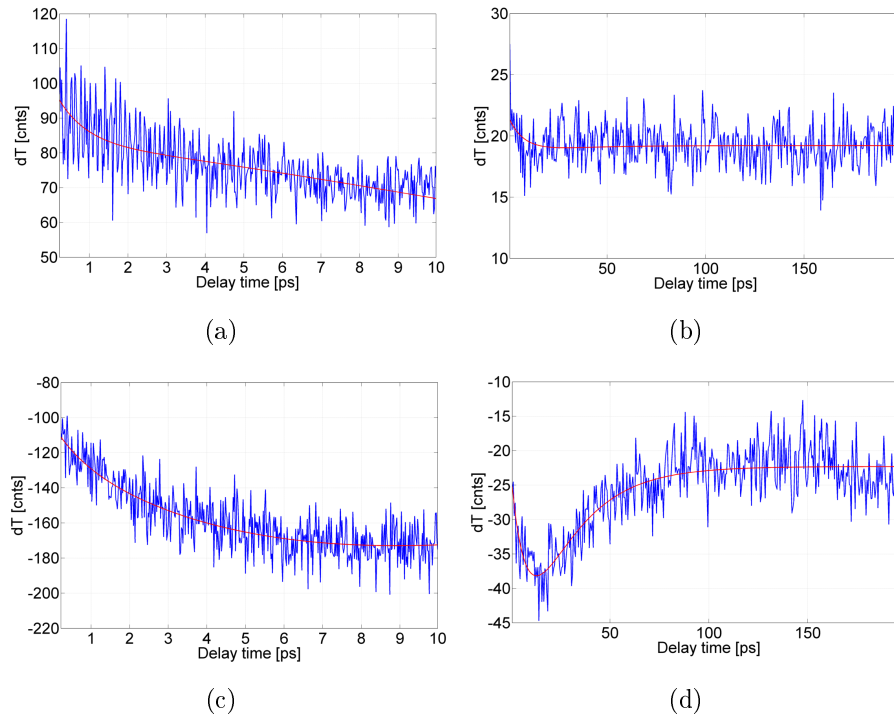
Figure A.10: Decay traces of selected wavelengths, extracted from the experimental TG spectra of Fig. 5.5 (pyrene in ethanol). (a) and (c) $10\,\mathrm{ps}$ scan, (b) and (d) $200\,\mathrm{ps}$ scan. (a) and (b) decay trace at $275\,\mathrm{nm}$, (c) and (d) decay trace at $256\,\mathrm{nm}$.

(a)

(b)

(c)

(d)

(e)

(f)

(g)

(h)

164
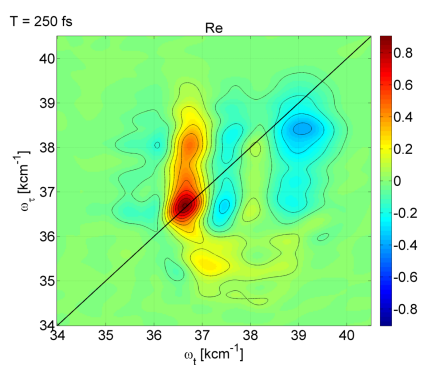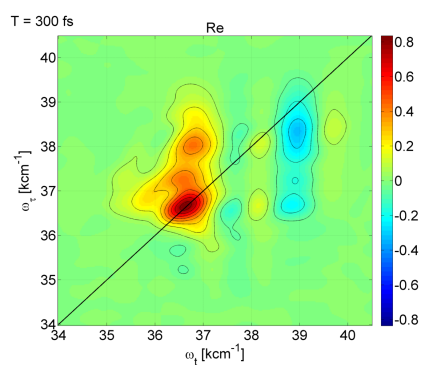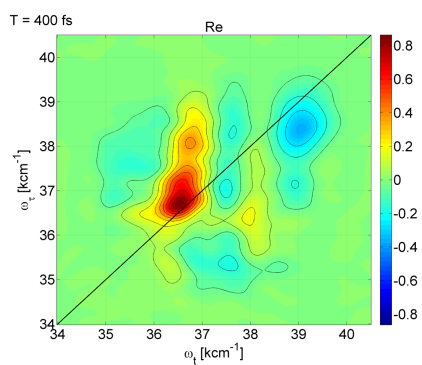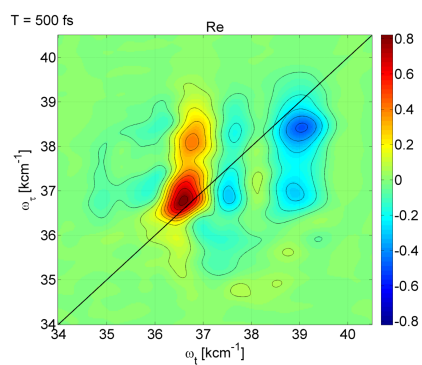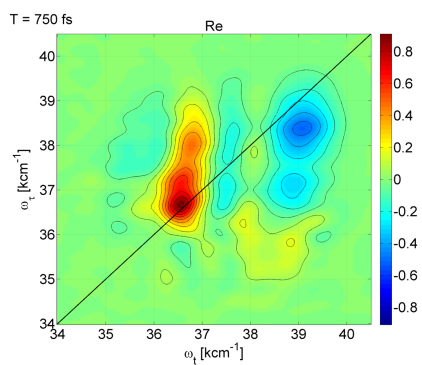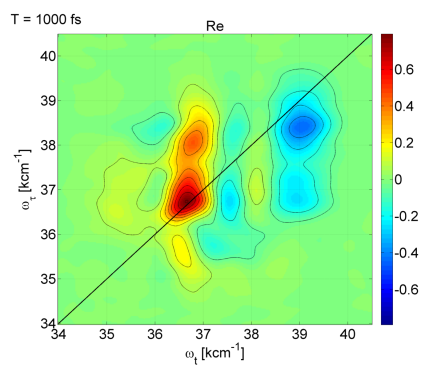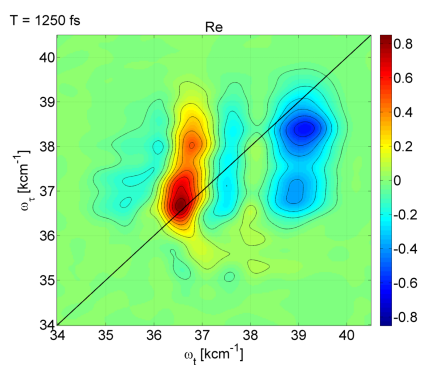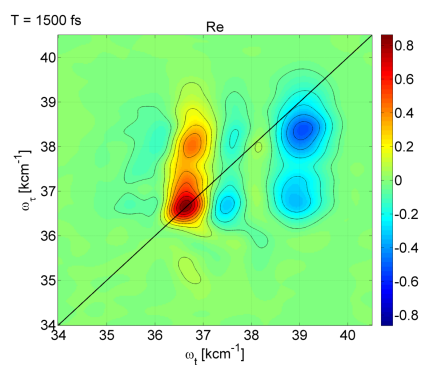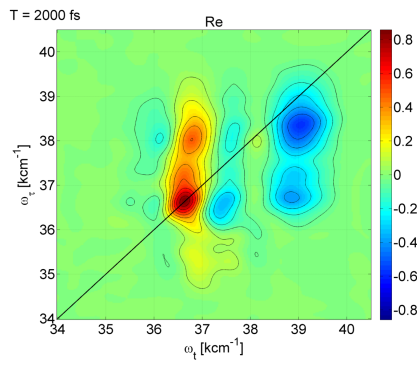
(i)
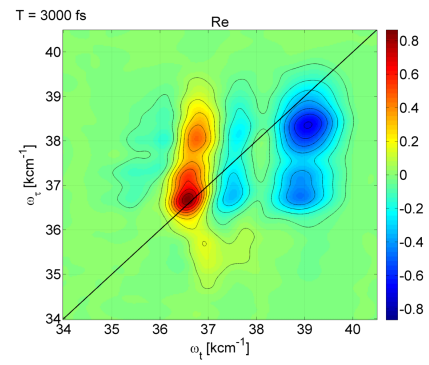
(j)
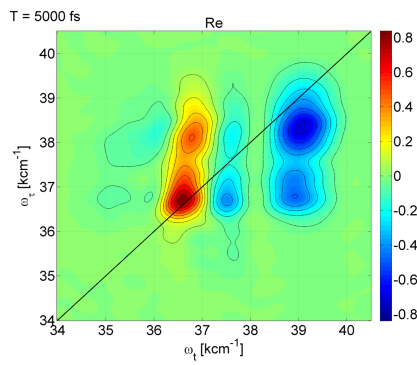
(k)
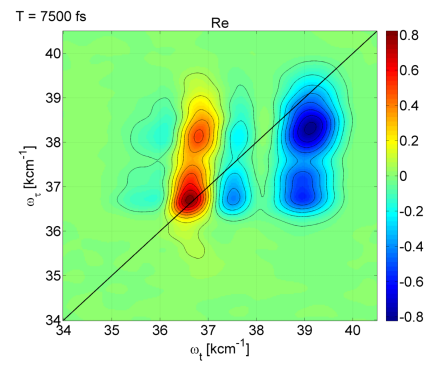
(l)

(m)

(n)

(o)

(p)

Figure A.10: Real part of photon echo spectra at various waiting time T of pyrene in ethanol. The contour steps are in 10% magnitudes; each spectrum is normalized to its maximum.

Bibliography

[1] G. P. Pfeifer, Y.-H. You and A. Besaratinia, *Mutation research*, 2005, **571**, 19–31.

[2] B. Bouvier, T. Gustavsson, D. Markovitsi, P. Millié and P. Milli, *Chemical Physics*, 2002, **275**, 75–92.

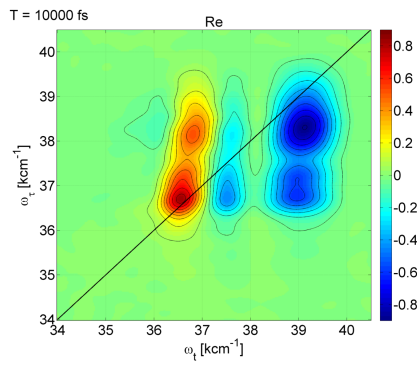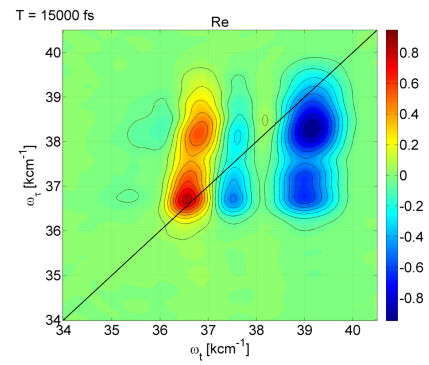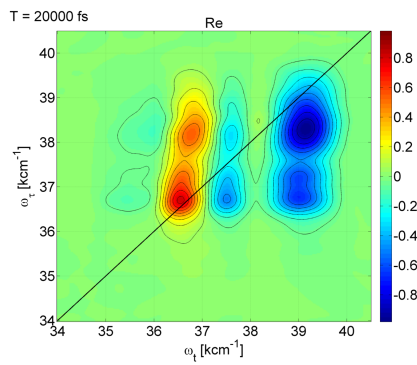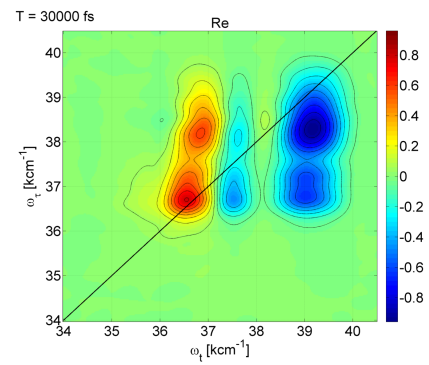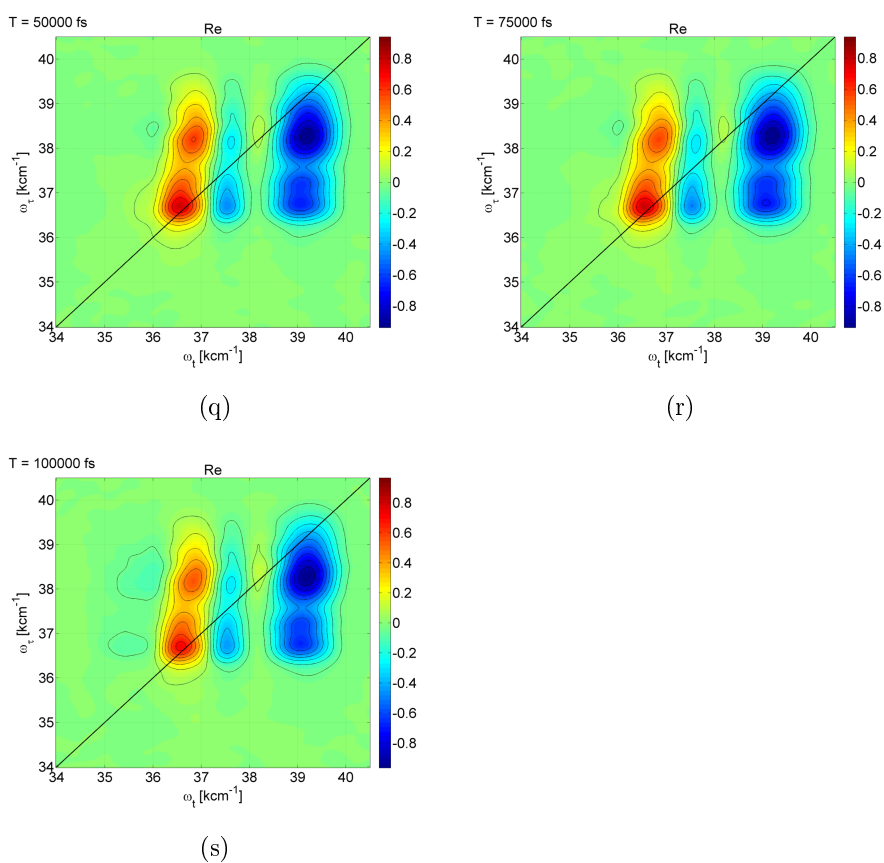[3] B. Bouvier, J.-p. Dognon, R. Lavery, D. Markovitsi, P. Millié, D. Onidas and K. Zakrzewska, *The Journal of Physical Chemistry B*, 2003, **107**, 13512–13522.

[4] J. Jortner, M. Bixon, T. Langenbacher and M. E. E. Michel-Beyerle, *Proceedings of the National Academy of Sciences*, 1998, **95**, 12759–12765.

[5] D. Onidas, T. Gustavsson, E. Lazzarotto and D. Markovitsi, *Physical chemistry chemical physics : PCCP*, 2007, **9**, 5143–5148.

[6] I. Buchvarov, Q. Wang, M. Raytchev, A. Trifonov and T. Fiebig, *Proceedings of the National Academy of Sciences of the United States of America*, 2007, **104**, 4794–4797.

[7] E. M. Conwell, P. M. McLaughlin and S. M. Bloch, *The Journal of Physical Chemistry B*, 2008, **112**, 2268–2272.

[8] D. Markovitsi, T. Gustavsson and F. Talbot, *Photochemical {&} photobiological sciences : Official journal of the European Photochemistry Association and the European Society for Photobiology*, 2007, **6**, 717–724.

[9] E. R. Bittner, *Journal of Photochemistry and Photobiology A: Chemistry*, 2007, **190**, 328–334.

[10] D. Markovitsi, *Pure and Applied Chemistry*, 2009, **81**, 1635–1644.

[11] D. Markovitsi, *Photochemistry and Photobiology*, 2015, 45–51.

[12] A. a. Voityuk, *Photochemical & photobiological sciences : Official journal of the European Photochemistry Association and the European Society for Photobiology*, 2013, **12**, 1303–1309.

[13] C. Su, C. T. Middleton and B. Kohler, *Journal of Physical Chemistry B*, 2012, **116**, 10266–10274.

[14] A. Banyasz, T. Douki, R. Improta, T. Gustavsson, D. Onidas, I. Vayá, M. Perron and D. Markovitsi, *Journal of the American Chemical Society*, 2012, **134**, 14834–14845.

[15] W.-M. Kwok, C. Ma and D. L. Phillips, *Journal of the American Chemical Society*, 2006, **128**, 11894–11905.

[16] W.-M. Kwok, C. Ma and D. L. Phillips, *Journal of the American Chemical Society*, 2008, **130**, 5131–5139.

[17] W. M. Kwok, C. Ma and D. L. Phillips, *Journal of Physical Chemistry B*, 2009, **113**, 11527–11534.

[18] A. Picchiotti, V. I. Prokhorenko and R. J. D. Miller, *Review of Scientific Instruments*, 2015, **86**, 093105.

[19] N. Krebs, I. Pugliesi, J. Hauer and E. Riedle, *New Journal of Physics*, 2013, **15**, year.

[20] A. Y. Freidzon, R. R. Valiev and A. A. Berezhnoy, *RSC Adv.*, 2014, **4**, 42054–42065.

[21] F. P. Schwarz and S. P. Wasik, *Analytical Chemistry*, 1976, **48**, 524–528.

[22] P. Foggi, L. Pettini, I. Santa, R. Righini and S. Califano, *Journal of Physical Chemistry*, 1995, **99**, 7439–7445.

[23] M. Raytchev, E. Pandurski, I. Buchvarov, C. Modrakowski and T. Fiebig, *Journal of Physical Chemistry A*, 2003, **107**, 4592–4600.

[24] H. Shinohara, Y. Yamakita and K. Ohno, *Journal of Molecular Structure*, 1998, **442**, 221–234.

[25] C. M. Jones and S. a. Asher, *The Journal of Chemical Physics*, 1988, **89**, 2649.

[26] N. Ismail, L. Blancafort, M. Olivucci, B. Kohler and M. a. Robb, *Journal of the American Chemical Society*, 2002, **124**, 6818–6819.

[27] H. Chen and S. Li, *Journal of Physical Chemistry A*, 2005, **109**, 8443–8446.

[28] V. I. Prokhorenko, A. Picchiotti, M. Pola, A. G. Dijkstra and R. J. D. Miller, *The Journal of Physical Chemistry Letters*, 2016, 4445–4450.

[29] HNP Mikrosysteme GmbH, *Operating manual for control module mzr-S06 / mzr-S06E*.

[30] V. I. Prokhorenko, A. Picchiotti, S. Maneshi and R. J. Dwayne Miller, in *Springer Proceedings in Physics*, ed. K. Yamanouchi, S. Cundiff, R. de Vivie-Riedle, M. Kuwata-Gonokami and L. DiMauro, Springer International Publishing, 2015, vol. 162, pp. 432–435.

[31] V. I. Prokhorenko, A. Picchiotti, S. Maneshi and R. J. D. Miller, in *Springer Proceedings in Physics*, ed. K. Yamanouchi, S. Cundiff, R. de Vivie-Riedle, M. Kuwata-Gonokami and L. DiMauro, Springer International Publishing, 2015, vol. 162, pp. 744–748.

[32] J. Frenkel, *Physical Review*, 1931, **37**, 17–44.

[33] B. A. West, J. M. Womick and A. M. Moran, *The Journal of Physical Chemistry A*, 2011, **115**, 8630–7.

[34] C.-h. Tseng, P. Sándor, M. Kotur, T. C. Weinacht and S. Matsika, *The journal of physical chemistry. A*, 2012, **116**, 2654–2661.

[35] H. Baba and M. Aoi, *Journal of Molecular Spectroscopy*, 1973, **46**, 214–222.

[36] T. Itoh, *Chemical Reviews*, 2012.

[37] J.-M. L. Pecourt, J. Peon and B. Kohler, *Journal of the American Chemical Society*, 2000, **122**, 9348–9349.

[38] H. Kang, K. T. Lee, B. Jung, Y. J. Ko and S. K. Kim, *Journal of the American Chemical Society*, 2002, **124**, 12958–12959.

[39] C. E. Crespo-Hernández and B. Kohler, *The Journal of Physical Chemistry B*, 2004, **108**, 11182–11188.

[40] C. E. Crespo-Hernández, B. Cohen and B. Kohler, *Nature*, 2005, **436**, 1141–1144.

[41] P. M. Hare, C. E. Crespo-Hernández and B. Kohler, *Proceedings of the National Academy of Sciences of the United States of America*, 2007, **104**, 435–440.

[42] C. T. Middleton, K. de La Harpe, C. Su, Y. K. Law, C. E. Crespo-Hernández and B. Kohler, *Annual Review of Physical Chemistry*, 2009, **60**, 217–239.

[43] X. Chen, W. Fang and H. Wang, *Physical chemistry chemical physics : PCCP*, 2014, **16**, 4210–4219.

[44] C. Ma, C. C.-W. Cheng, C. T.-L. Chan, R. C.-T. Chan and W.-M. Kwok, *Physical chemistry chemical physics : PCCP*, 2015, **17**, 19045–57.

[45] B. Xue, A. Yabushita and T. Kobayashi, *Phys. Chem. Chem. Phys.*, 2016, **18**, 17044–17053.

[46] J. Peon and A. H. Zewail, *Chemical Physics Letters*, 2001, **348**, 255–262.

[47] D. Onidas, D. Markovitsi, S. Marguet, A. Sharonov and T. Gustavsson, *The Journal of Physical Chemistry B*, 2002, **106**, 11367–11374.

[48] T. Pancur, N. K. Schwalb, F. Renth and F. Temps, *Chemical Physics*, 2005, **313**, 199–212.

[49] S. Ullrich, T. Schultz, M. Z. Zgierski and A. Stolow, *Physical Chemistry Chemical Physics*, 2004, **6**, 2796.

[50] C. Z. Bisgaard, H. Satzger, S. Ullrich and A. Stolow, *ChemPhysChem*, 2009, **10**, 101–110.

[51] N. L. Evans and S. Ullrich, *The journal of physical chemistry. A*, 2010, **114**, 11225–11230.

[52] F. Buchner, A. Nakayama, S. Yamazaki, H.-H. Ritze and A. Lübcke, *Journal of the American Chemical Society*, 2015, **137**, 2931–2938.

[53] J.-M. L. Pecourt, J. Peon and B. Kohler, *Journal of the American Chemical Society*, 2001, **123**, 10370–8.

[54] A. Kossel, *Zeitschrift für physiologische Chemie*, 1879, **3**, 284–291.

[55] A. Kossel, *Zeitschrift für physiologische Chemie*, 1880, **4**, 290–295.

[56] H. M. Ward, *Proceedings of the Royal Society of London*, 1892, **52**, 393–400.

[57] N. G. Reed, *Public Health Reports*, 2010, **125**, 15–27.

[58] W. N. Hartley, *Journal of the Chemical Society, Transactions*, 1905, **87**, 1796.

[59] N. K. Koltzoff, *Biol. Zbl*, 1928, **48**, 345–369.

[60] E. Altenburg, *The American Naturalist*, 1928, **62**, 540–545.

[61] G. M. Findlay, *The Lancet*, 1928, 1070–1073.

[62] H. B. Newcombe and H. A. Whitehead, *J Bacteriol*, 1951, **61**, 243–251.

[63] J. D. WATSON and F. H. C. CRICK, *Nature*, 1969, **224**, 470–471.

[64] J. Watson and F. Crick, *Nature*, 1969, **224**, 470–471.

[65] D. E. Duggan, R. L. Bowman, B. B. Brodie and S. Udenfriend, *Archives of Biochemistry and Biophysics*, 1957, **68**, 1–14.

[66] A. N. Pisarevskii, S. N. Cherenkevich and V. T. Andrianov, *Journal of Applied Spectroscopy*, 1966, **5**, 452–454.

[67] J. Eisinger and R. Shulman, *Science*, 1968, **161**, 1311–1319.

[68] J. Falk and J. E. Murray, *Applied Physics Letters*, 1969, **14**, 245–247.

[69] G. D. Reid and K. Wynne, *Encyclopedia of Analytical chemistry*, 2000.

[70] D. Markovitsi, A. Sharonov, D. Onidas and T. Gustavsson, *Chemphyschem*, 2003, **4**, 303—+.

[71] C. E. Crespo-Hernández, B. Cohen, P. M. Hare and B. Kohler, *Chemical Reviews*, 2004, **104**, 1977–2020.

[72] Wikipedia, *Wikipedia*.

[73] C. Houssier and K. Sauer, *Journal of the American Chemical Society*, 1970, **92**, 779–791.

[74] Y.-M. Chang, C. K.-M. Chen and M.-H. Hou, *International journal of molecular sciences*, 2012, **13**, 3394–3413.

[75] D. M. Gray, *Biopolymers*, 1974, **13**, 2087–2102.

[76] D. M. Gray and R. L. Ratliff, *Biopolymers*, 1975, **14**, 487–498.

[77] A. I. S. Holm, B. Kohler, S. V. Hoffmann and S. Brøndsted Nielsen, *Biopolymers*, 2010, **93**, 429–33.

[78] U. R. Kadhane, A. I. S. Holm, S. V. Hoffmann and S. B. Nielsen, *Physical Review E*, 2008, **77**, 21901.

[79] S. B. Nielsen, T. Chakraborty and S. V. Hoffmann, *Chemphyschem : a European journal of chemical physics and physical chemistry*, 2005, **6**, 2619–2624.

[80] C. S. M. Olsthoorn, L. J. Bostelaar, J. F. M. Rooij, J. H. Boom and C. Altona, *European Journal of Biochemistry*, 1981, **115**, 309–321.

[81] C. A. Sprecher and W. C. Johnson, *Biopolymers*, 1977, **16**, 2243–2264.

[82] D. M. Gray, R. L. Ratliff and M. R. Vaughan, *Methods in enzymology*, 1992, **211**, 389–406.

[83] A. H. Zewail, *The Journal of Physical Chemistry A*, 2000, **104**, 5660–5694.

[84] N. Huse, *Ph.D. thesis*, Hamburg, 2006.

[85] S. E. Braslavsky, *Pure and Applied Chemistry*, 2007, **79**, 293–465.

[86] P. Hamm and M. Zanni, *Concepts and methods of 2D infrared spectroscopy*, Cambridge University Press, 2011.

[87] M. Cho, *Two-dimensional optical spectroscopy*, CRC press, 2009.

[88] S. Mukamel, *Principles of nonlinear optical spectroscopy*, Oxford University Press on Demand, 1999.

[89] L. Lepetit, G. Chériaux and M. Joffre, *Journal of the Optical Society of America B*, 1995, **12**, 2467.

[90] F. Miescher, 1869.

[91] I.-I. Comm, *Biochemistry*, 1970, **9**, 4022–4027.

[92] C. o. B. N. IUPAC-IUB, *Biochimica et biophysica acta. Nucleic acids and protein synthesis.*, 1971, **247**, 1–12.

[93] T. Katoh, Y. Inagaki and R. Okazaki, *Bulletin of the Chemical Society of Japan*, 1997, **70**, 2279–2286.

[94] A. Mishra, R. K. Behera, P. K. Behera, B. K. Mishra and G. B. Behera, *Chemical Reviews*, 2000, **100**, 1973–2012.

[95] J. Frenkel, *Physical Review*, 1931, **37**, 1276–1294.

[96] A. S. Davydov, *Theory of Molecular Excitons*, Springer US, Boston, MA, 1971.

[97] *Mo et al. - 2014(2).pdf*.

[98] H. Haken, *Journal of Physics and Chemistry of Solids*, 1959, **8**, 166–171.

[99] A. S. Davydov, *Soviet Physics Uspekhi*, 1964, **7**, 145–178.

[100] M. Kasha, H. R. Rawls and M. Ashraf El-Bayoumi, *Pure and Applied Chemistry*, 1965, **11**, 371–392.

[101] L. Blancafort and A. A. Voityuk, *Journal of Chemical Physics*, 2014, **140**, year.

[102] U. Brackmann, *Lambdachrome laser dyes*, 1986.

[103] F. L. Arbeloa, I. L. Gonzalez, P. R. Ojeda and I. L. Arbeloa, *Journal of the Chemical Society, Faraday Transactions 2*, 1982, **78**, 989.

[104] O. Valdes-Aguiler and D. C. Neckers, *Accounts Of Chemical Research.*, 1989, **22**, 171–177.

[105] L. Hu, Y. Zhao, F. Wang, G. Chen, C. Ma, W.-M. Kwok and D. L. Phillips, *The journal of physical chemistry B*, 2007, **111**, 11812–6.

[106] H.-H. Ritze, P. Hobza and D. Nachtigallová, *Physical Chemistry Chemical Physics*, 2007, **9**, 1672.

[107] D. Voet, W. B. Gratzer, R. a. Cox and P. Doty, *Biopolymers*, 1963, **1**, 193–208.

[108] A. V. Tataurov, Y. You and R. Owczarzy, *Biophysical chemistry*, 2008, **133**, 66–70.

[109] C. R. Cantor, M. M. Warshaw and H. Shapiro, *Biopolymers*, 1970, **9**, 1059–77.

[110] L. M. Baggesen, S. V. Hoffmann and S. B. Nielsen, *Photochemistry and photobiology*, 2013, **1**, 99–106.

[111] W. Saenger, *Principles of Nucleic Acid Structure*, Springer New York, New York, NY, 1984.

[112] H. S. Harned and S. R. Scholes Jr, *Journal of the American Chemical Society*, 1941, **63**, 1706–1709.

[113] H. S. Harned and R. Davis Jr, *Journal of the American Chemical Society*, 1943, **65**, 2030–2037.

[114] D. Markovitsi, D. Onidas, F. Talbot, S. Marguet, T. Gustavsson and E. Lazzarotto, *Journal of Photochemistry and Photobiology A: Chemistry*, 2006, **183**, 1–8.

[115] M. Vorlícková, I. Kejnovská, J. Kovanda and J. Kypr, *Nucleic Acids Research*, 1998, **26**, 1509–14.

[116] B. Cohen, P. M. Hare and B. Kohler, *Journal of the American Chemical Society*, 2003, **125**, 13594–13601.

[117] M. Vorlícková, I. Kejnovská, J. Kovanda and J. Kypr, *Nucleic Acids Research*, 1999, **27**, 581–586.

[118] D. Markovitsi, F. Talbot, T. Gustavsson, D. Onidas, E. Lazzarotto and S. Marguet, *Nature*, 2006, **441**, E7; discussion E8.

[119] K. de la Harpe, C. E. Crespo-Hernández and B. Kohler, *Chemphyschem : a European journal of chemical physics and physical chemistry*, 2009, **10**, 1421–1425.

[120] F.-A. Miannay, A. Banyasz, T. Gustavsson and D. Markovitsi, *The Journal of Physical Chemistry C*, 2009, **113**, 11760–11765.

[121] P. Changenet-Barret, E. Emanuele, T. Gustavsson, R. Improta, A. B. Kotlyar, D. Markovitsi, I. Vayá, K. Zakrzewska and D. Zikich, *The Journal of Physical Chemistry C*, 2010, **114**, 14339–14346.

[122] E. Emanuele, K. Zakrzewska, D. Markovitsi, R. Lavery and P. Millié, *The journal of physical chemistry B*, 2005, **109**, 16109–16118.

[123] V. I. Pechenaya, *Chemical Physics Letters*, 1975, **34**, 585–587.

[124] Jena Bioscience GmbH, *{Jena Bioscience GmbH}*.

[125] A. L. Burin, M. E. Armbruster, M. Hariharan and F. D. Lewis, *Proceedings of the National Academy of Sciences of the United States of America*, 2009, **106**, 989–994.

[126] Y. Zhao and D. G. Truhlar, *Theoretical Chemistry Accounts*, 2008, **120**, 215–241.

[127] A. J. A. Aquino, D. Nachtigallová, P. Hobza, D. G. Truhlar, C. Hättig and H. Lischka, *Journal of Computational Chemistry*, 2011, **32**, 1217–1227.

[128] P. G. Szalay, T. Watson, A. Perera, V. F. Lotrich and R. J. Bartlett, *Journal of Physical Chemistry A*, 2013, **117**, 3149–3157.

[129] A. Trofimov and J. Schirmer, *Journal of Physics B: Atomic, Molecular and Optical Physics*, 1995, **28**, 2299.

[130] A. Dreuw and M. Wormit, *Wiley Interdisciplinary Reviews: Computational Molecular Science*, 2015, **5**, 82–95.

[131] J. D. Watts and R. J. Bartlett, *Chemical Physics Letters*, 1995, **233**, 81–87.

[132] T. J. Watson Jr, V. F. Lotrich, P. G. Szalay, A. Perera and R. J. Bartlett, *The Journal of Physical Chemistry A*, 2013, **117**, 2569–2579.

[133] M. J. Frisch, G. W. Trucks, H. B. Schlegel, G. E. Scuseria, M. A. Robb, J. R. Cheeseman, G. Scalmani, V. Barone, B. Mennucci, G. A. Petersson, H. Nakatsuji, M. Caricato, X. Li, H. P. Hratchian, A. F. Izmaylov, J. Bloino, G. Zheng, J. L. Sonnenberg, M. Hada, M. Ehara, K. Toyota, R. Fukuda, J. Hasegawa, M. Ishida, T. Nakajima, Y. Honda, O. Kitao, H. Nakai, T. Vreven, J. A. J. Montgomery, J. E. Peralta, F. Ogliaro, M. Bearpark, J. J. Heyd, E. Brothers, K. N. Kudin, V. N. Staroverov, R. Kobayashi, J. Normand, K. Raghavachari, A. Rendell, J. C. Burant, S. S. Iyengar, J. Tomasi, M. Cossi, N. Rega, J. M. Millam, M. Klene, J. E. Knox, J. B. Cross, V. Bakken, C. Adamo, J. Jaramillo, R. Gomperts, R. E. Stratmann, O. Yazyev, A. J. Austin, R. Cammi, C. Pomelli, J. W. Ochterski, R. L. Martin, K. Morokuma, V. G. Zakrzewski, G. A. Voth, P. Salvador, J. Dannenberg, S. Dapprich, A. D. Daniels, Ö. Farkas, J. B. Foresman, J. V. Ortiz, J. Cioslowski and D. J. Fox, *Gaussian 09, Revision D.01*, 2009.

[134] D. M. York and M. Karplus, *J. Phys. Chem. A*, 1999, **103**, 11060–11079.

[135] G. Scalmani and M. J. Frisch, *The Journal of Chemical Physics*, 2010, **132**, 114110.

[136] J. Sambrook, E. F. Fritsch, T. Maniatis *et al.*, *Molecular cloning: a laboratory manual.*, Cold spring harbor laboratory press, 1989.

[137] A. I. S. Holm, L. M. Nielsen, S. V. Hoffmann and S. B. Nielsen, *Physical chemistry chemical physics : PCCP*, 2010, **12**, 9581–96.

[138] C. S. M. Olsthoorn, C. a. Haasnoot and C. Altona, *European journal of biochemistry / FEBS*, 1980, **106**, 85–95.

[139] J. Greve, M. F. Maestre and A. Levin, *Biopolymers*, 1977, **16**, 1489–1504.

[140] J. Brahms, a. M. Michelson and K. E. Van Holde, *Journal of molecular biology*, 1966, **15**, 467–488.

[141] L. M. Nielsen, S. V. Hoffmann and S. Brøndsted Nielsen, *Physical chemistry chemical physics : PCCP*, 2012, **14**, 15054–9.

[142] I. E. Scheffler, E. L. Elson and R. L. Baldwin, *Journal of Molecular Biology*, 1968, **36**, 291–304.

[143] A. L. Burin, J. A. Dickman, D. B. Uskov, C. F. F. Hebbard and G. C. Schatz, *The Journal of Chemical Physics*, 2008, **129**, 091102.

[144] M. J. Tauber, R. a. Mathies, X. Chen and S. E. Bradforth, *Review of Scientific Instruments*, 2003, **74**, 4958.

[145] M. Kondoh and M. Tsubouchi, *Optics Express*, 2014, **22**, 14135–14147.

[146] D. Toptygin, B. Z. Packard and L. Brand, *Chemical Physics Letters*, 1997, **277**, 430–435.

[147] A. Dubietis, G. Jonušauskas and A. Piskarskas, *Optics Communications*, 1992, **88**, 437–440.

[148] G. Cerullo, M. Nisoli and S. de Silvestri, *Applied Physics Letters*, 1997, **71**, 3616.

[149] A. Shirakawa and T. Kobayashi, *Applied Physics Letters*, 1998, **72**, 147–149.

[150] A. Shirakawa, I. Sakane, M. Takasaka and T. Kobayashi, *Appl. Phys. Lett.*, 1999, **74**, 2268–2270.

[151] G. Cerullo and S. De Silvestri, *Review of Scientific Instruments*, 2003, **74**, 1–18.

[152] R. W. Boyd, *Nonlinear optics*, Taylor & Francis, 2003, pp. 161–183.

[153] Y.-R. Shen, *The principles of nonlinear optics*, New York, Wiley-Interscience, 1984, 575 p., 1984, vol. 1.

[154] S. X. Dou, D. Josse and J. Zyss, *Journal of the Optical Society of America B*, 1992, **9**, 1312.

[155] E. Riedle, M. Beutter, S. Lochbrunner, J. Piel, S. Schenkl, S. Spörlein and W. Zinth, *Applied Physics B*, 2000, **71**, 457–465.

[156] R. L. Fork, C. V. Shank, C. Hirlimann, R. Yen and W. J. Tomlinson, *Optics letters*, 1983, **8**, 1–3.

[157] A. Couairon and A. Mysyrowicz, *Physics Reports*, 2007, **441**, 47–189.

[158] I. Buchvarov, A. Trifonov and T. Fiebig, *Conference on Lasers and Electro-Optics Europe - Technical Digest*, 2007, **32**, 1539–1541.

[159] U. Megerle, I. Pugliesi, C. Schriever, C. F. Sailer and E. Riedle, *Applied Physics B: Lasers and Optics*, 2009, **96**, 215–231.

[160] P. Baum, S. Lochbrunner and E. Riedle, *Optics letters*, 2004, **29**, 1686–1688.

[161] P. Baum, S. Lochbrunner and E. Riedle, *Applied Physics B: Lasers and Optics*, 2004, **79**, 1027–1032.

[162] K. W. DeLong, D. N. Fittinghoff, R. Trebino, B. Kohler and K. Wilson, *Optics letters*, 1994, **19**, 2152–2154.

[163] R. Trebino, K. W. DeLong, D. N. Fittinghoff, J. N. Sweetser, M. A. Krumbügel, B. A. Richman and D. J. Kane, *Review of Scientific Instruments*, 1997, **68**, 3277.

[164] V. I. Prokhorenko, A. Halpin and R. J. D. Miller, *Optics Express*, 2009, **17**, 9764.

[165] U. Selig, C.-F. Schleussner, M. Foerster, F. Langhojer, P. Nuernberger and T. Brixner, *Optics letters*, 2010, **35**, 4178–4180.

[166] V. I. Prokhorenko, *EPA newsletters*, 2012, 21–23.

[167] M. Barbatti, A. C. Borin and S. Ullrich, *Photoinduced Phenomena in Nucleic Acids I*, Springer International Publishing, Cham, Springer I edn., 2015, vol. 355, pp. 39–87.

[168] A. Nenov, S. Mukamel, M. Garavelli and I. Rivalta, *Journal of Chemical Theory and Computation*, 2015, **11**, 3755–3771.

[169] A. Nenov, I. Rivalta, G. Cerullo, S. Mukamel and M. Garavelli, *The journal of physical chemistry letters*, 2014, **5**, 767–771.

[170] A. Nenov, A. Giussani, J. Segarra-Martí, V. K. Jaiswal, I. Rivalta, G. Cerullo, S. Mukamel and M. Garavelli, *Journal of Chemical Physics*, 2015, **142**, year.

[171] A. Nenov, A. Giussani, B. P. Fingerhut, I. Rivalta, E. Dumont, S. Mukamel and M. Garavelli, *Phys. Chem. Chem. Phys.*, 2015, **17**, 30925–30936.

[172] R. Tempelaar, C. P. van der Vegte, J. Knoester and T. L. Jansen, *The Journal of chemical physics*, 2013, **138**, 164106.

[173] M. Richter and B. P. Fingerhut, *Journal of chemical theory and computation*, 2016, **12**, 3284–3294.

[174] M. K. Lee and D. F. Coker, *The Journal of Physical Chemistry Letters*, 2016, **7**, 3171–3178.

[175] P. Siegbahn, A. Heiberg, B. Roos and B. Levy, *Roos BO, Taylor PR, Siegbahn PEM (1980) Chem Phys*, 1980, **48**, 157.

[176] B. O. Roos, *Advances in Chemical Physics: Ab Initio Methods in Quantum Chemistry Part 2, Volume 69*, 1987, 399–445.

[177] K. Andersson, P. A. Malmqvist, B. O. Roos, A. J. Sadlej and K. Wolinski, *Journal of Physical Chemistry*, 1990, **94**, 5483–5488.

[178] K. Andersson, P.-Å. Malmqvist and B. O. Roos, *The Journal of chemical physics*, 1992, **96**, 1218–1226.

[179] P. A. Malmqvist, A. Rendell and B. O. Roos, *Journal of Physical Chemistry*, 1990, **94**, 5477–5482.

[180] P. Å. Malmqvist, K. Pierloot, A. R. M. Shahi, C. J. Cramer and L. Gagliardi, *The Journal of chemical physics*, 2008, **128**, 204109.

[181] F. Aquilante, J. Autschbach, R. K. Carlson, L. F. Chibotaru, M. G. Delcey, L. De Vico, I. Fdez. Galván, N. Ferré, L. M. Frutos, L. Gagliardi, M. Garavelli, A. Giussani, C. E. Hoyer, G. Li Manni, H. Lischka, D. Ma, P. Å. Malmqvist, T. Müller, A. Nenov, M. Olivucci, T. B. Pedersen, D. Peng, F. Plasser, B. Pritchard, M. Reiher, I. Rivalta, I. Schapiro, J. Segarra-Martí, M. Stenrup, D. G. Truhlar, L. Ungur, A. Valentini, S. Vancoillie, V. Veryazov, V. P. Vysotskiy, O. Weingart, F. Zapata and R. Lindh, *Journal of Computational Chemistry*, 2016, **37**, 506–541.

[182] P.-O. Widmark, B. J. Persson and B. O. Roos, *Theoretica chimica acta*, 1991, **79**, 419–432.

[183] T. B. Pedersen, F. Aquilante and R. Lindh, *Theoretical Chemistry Accounts*, 2009, **124**, 1–10.

[184] K. Andersson, F. Aquilante, M. Barysz, A. Bernhardsson, M. R. A. Blomberg, J. Bostrom, Y. Carissan, L. Chibotaru, D. L. Cooper, M. Cossi, O. Danyliv, M. Delcey, A. Devarajan, L. DeVico, N. Ferré, M. P. Fülscher, A. Gaenko, L. Gagliardi, I. Fdez.. Galván, G. Ghigo, C. de Graaf, S. Gusarov, D. Hagberg, J. Hasegawa, B. A. Hess, A. Holt, G. Karlström, J. Krogh, R. Lindh, P. A. Malmqvist, T. Nakajima, N. P., J. Olsen, T. Pedersen, D. Peng, M. Pitonák, J. Raab, J. Hermida-Ramón, M. Reiher, B. O. Roos, U. Ryde, B. Schimmelpfennig, M. Schütz, L. Seijo, L. Serrano-Andrés, I. Schapiro, P. E. M. Siegbahn, P. Söderhjelm, J. Stalring, B. Suo, P. Sushko, T. Thorsteinsson, T. Tsuchiya, L. Ungur, S. Vancoillie, V. Veryazov, V. P. Vysotskiy, U. Wahlgren, P.-O. Widmark and A. Öhrn, *Molcas 8*.

[185] P. Altoè, M. Stenta, A. Bottoni and M. Garavelli, *Theoretical Chemistry Accounts*, 2007, **118**, 219–240.

[186] D. Abramavicius, B. Palmieri, D. V. Voronine, F. Sanda and S. Mukamel, *Chemical reviews*, 2009, **109**, 2350–2408.

[187] L. Valkunas, D. Abramavicius and T. Mancal, *Molecular excitation dynamics and relaxation: quantum theory and spectroscopy*, John Wiley & Sons, 2013.

[188] B. Li, A. Johnson, S. Mukamel and A. Myers, *J. Am. Chem. Soc*, 1994, **116**, 11039–11047.

[189] B. a. West, B. P. Molesky, P. G. Giokas and A. M. Moran, *Chemical Physics*, 2013, **423**, 92–104.

[190] F. V. R. Neuwahl and P. Foggi, *Laser Chemistry*, 1999, **19**, 375–379.

[191] H. Baba, A. Nakajima, M. Aoi and K. Chihara, *The Journal of Chemical Physics*, 1971, **55**, 2433.

[192] P. R. Salvi, P. Foggi and E. Castelucci, *Chemical Physics Letters*, 1983, **98**, 206–211.

[193] D. Karpovich and G. Blanchard, *Journal of Physical Chemistry*, 1995, **99**, 3951–3958.

[194] J. Conte, *Revista Portuguesa de Química*, 1967, **9**, 35.

[195] T. Deinum, C. Werkhoven, J. Langelaar, R. Rettschnick and J. van Voorst, *Chemical Physics Letters*, 1971, **12**, 189–192.

[196] B. Nickel and G. Roden, *Chemical Physics Letters*, 1980, **71**, 238–241.

[197] Y. Harabuchi, T. Taketsugu and S. Maeda, *Physical chemistry chemical physics : PCCP*, 2015, **17**, 22561–22565.

[198] A. L. Sobolewski and W. Domcke, *European Physical Journal D*, 2002, **20**, 369–374.

[199] M. Merchán, L. Serrano-Andrés, M. A. Robb and L. Blancafort, *Journal of the American Chemical Society*, 2005, **127**, 1820–1825.

[200] P. Vigny, *Comptes rendus hebdomadaires des séances de l'Académie des sciences. Série D: Sciences naturelles*, 1971, **272**, 3206–9.

[201] A. Y. Hirakawa, H. Okada, S. Sasagawa and M. Tsuboi, *Spectrochimica Acta Part A: Molecular Spectroscopy*, 1985, **41**, 209–216.

[202] R. Improta, F. Santoro and L. Blancafort, *Chemical Reviews*, 2016, **116**, 3540–3593.

[203] M. Daniels and W. Hauswirth, *Science (New York, N.Y.)*, 1971, **171**, 675–7.

[204] L. Marrot and J.-R. Meunier, *Journal of the American Academy of Dermatology*, 2008, **58**, S139–48.

[205] P. G. Buettner and B. a. Raasch, *International journal of cancer. Journal international du cancer*, 1998, **78**, 587–593.

[206] D. L. Mitchell and D. Karentz, in *Environmental UV Photobiology*, ed. A. R. Young, J. Moan, L. Björn and W. Nultsch, Springer US, 1993, ch. 2, pp. 345–377.

[207] D. Angelov, B. Beylot and A. Spassky, *Biophysical journal*, 2005, **88**, 2766–78.

[208] F. Santoro, R. Improta, F. Avila, M. Segado and A. Lami, *Photochemical & photobiological sciences : Official journal of the European Photochemistry Association and the European Society for Photobiology*, 2013, **12**, 1527–1543.

[209] N. L. Goddard, G. Bonnet, O. Krichevsky and A. Libchaber, *Physical review letters*, 2000, **85**, 2400–2403.